A Measurement of the Diffractive Reduced Cross-Section $\sigma_r^{D(3)}$ at High Q^2 with the H1 Detector at HERA

Thesis submitted in accordance with the requirements

of the University of Liverpool

for the degree of Doctor in Philosophy

by

Paul James Laycock

May 2003

Abstract

A measurement is presented which investigates the nature of diffractive exchanges. Data taken by the H1 experiment amounting to an integrated luminosity of $\mathcal{L} = 63$ pb^{-1} are used to investigate the process $ep \to eXY$ in the kinematic range where diffractive exchanges are known to dominate. The Y system is a proton or proton remnant with $M_Y < 1.6$ GeV and $|t| < 1.0$ GeV^2 and it is separated from the X system by a large gap in rapidity caused by a diffractive exchange carrying a fraction of the proton's longitudinal momentum $x_{I\!P} \leq 0.05$. The diffractive reduced cross-section $\sigma_r^{D(3)}$ is extracted at high Q^2 in the kinematic range $Q^2 > 130$ GeV$^2, 0.07 < (\beta = x/x_{I\!P}) < 1.0$ and $0.005 < x_{I\!P} \leq 0.05$. The data are used to test several models of diffraction and a fit to the data allows the extraction of the effective Pomeron intercept and Pomeron parton density functions.

The new Object-Oriented generic analysis framework used to perform the analysis is also presented. The framework consists of a set of objects which provide the necessary functionality and flexibility to perform very different and complex physics analyses while maintaining a constant core structure.

"It is contrary to reason to say that there is a vacuum or space in which there is absolutely nothing." - *Descartes*.

Acknowledgements

Thanks to all of the people that have made this thesis possible. Top of this list is my supervisor Dave Milstead who played "Bad Cop" when reviewing my attempts at scientific writing. "Good Cop" was played admirably well by Steve Maxfield who undoubtedly had the more difficult of the two roles. Thanks also to the University of Liverpool for funding the last stages of my PhD, especially to Paul Booth, John Dainton, Tim Greenshaw and of course Erwin Gabathuler who got me into this in the first place.

Thanks to all of the people that have made the analysis possible. Special thanks go to Frank-Peter Schilling who performed the fits to the data and without whom the reader would have found the penultimate chapter a little disappointing. Unlike Frank, Andy Mehta, Paul Newman, Eram Rizvi and Paul Thompson were bound out of a sense of national duty to answer all of my questions but all four went above and beyond the call of duty by keeping a straight face, or at least waiting until I left the room before laughing hysterically.

Thanks to all of the people that have made my PhD as enjoyable as it has been. The Hamburg gang is led by my principle collaborator, Dave South, who also proof read this thesis along with playing a position I like to call "Paul's Number 2" in the development of the generic analysis framework. Matt Beckingham, Yves[2] Coppens and Fleming, Oliver Henshaw, John Kennedy, Nick Malden and Ethan-Etienne Woehrling are an alphabetically ordered and incomplete list of the rest of the Hamburg gang members irresponsible for much of the aforementioned enjoyment. Richard Sloane leads the Liverpool gang, where the points-system is based on the number of nights a member of the gang has put me up, with Michael George and Mark Tobin taking deserved places on the podium. Andy Washbrook and Dave Payne stave off relegation once again this season due to a technicality.

Thanks to all of my friends back in the UK and from way back when. James

and Alison probably should have considered renting that back bedroom out to me, or at least demanded some recompense to get rid of the smell (a party-size pizza, a family-size bucket of chicken and a crate of beer can do terrible things to a man); I can only say thank you. Thanks to Paddy for teaching me all of the fiddly stuff that I can play on the guitar and Rob, Rich, Keith, John, Ian, Billy, Boff, Gus and everyone else who contributed in their own peculiar ways to making student life great, if a little mouldy.

Thanks to all of my family for their unwaning love and support over the years. I feel very lucky to have such a big family who always seem to have been absolutely convinced that I could do this. My repayment of several score pages of unintelligible nonsense hardly seems appropriate, but I assure you all that it's dead clever unintelligible nonsense that means that I'm now a Doctor.

Finally, special thanks to Mum, Dad, Alison and Jennifer. You have given me a lot over the years and the words fail me, which is why I did Physics instead of English, so I dedicate this thesis to you. Thank you for everything, because it doesn't take a Doctor of Particle Physics to tell you that without everything none of this would have been possible. I also include in the dedication of this thesis my 4-year old nephew, William, who will be forced to read this until he understands it. Fair is fair, lad.

Figure 1: *The results of this experiment were a little easier to digest.*

The Author's Contribution

The author is responsible for the analysis leading to the extraction of the cross-section measurement and its subsequent interpretation and developed the studies of the forward detectors and the invariant mass correction method. The analysis relies upon a generic analysis framework entirely designed by the author who also played a leading role in its implementation and this framework is now being used by the H1 collaboration. The author also played a leading role in the implementation in C++ of the algorithms necessary to perform the event selection.

The author assisted in the operation of the H1 detector as both a shift crew member and on-call expert for the Forward Track and Forward Muon Detectors. The author was also responsible for connecting the PVSS high-voltage control software to the central ORACLE database at DESY.

Finally, the author has presented results on inclusive diffraction, including the results presented in this thesis, at several international conferences and workshops on behalf of both the H1 and Zeus collaborations.

A Note on Units

In the work presented in this thesis a system of natural units is used whereby $\hbar = c = 1$.

This work was supported by the UK Particle Physics and Astronomy Research Council (PPARC) between September 1999 and August 2002.

For Mum, Dad, Alison, Jennifer and William

Contents

List of Figures

List of Tables

Introduction

The observation at HERA of events with a large region of rapidity devoid of hadronic activity, a rapidity gap, renewed interest in the field of diffraction and gave the Pomeron a new lease of life. The measurement presented in this thesis significantly extends the precision and phase-space of diffractive cross-sections.

Pomeranchuk studied the asymptotic behaviour of the S-matrix and proved [1,2] that the cross-section for any process which involved the exchange of quantum numbers must vanish as the centre of mass energy s increased. Foldy and Peierls proved [3] that, conversely, if the cross-section for a process does not vanish as s increases that cross-section must be dominated by the exchange of vacuum quantum numbers, a so-called diffractive exchange. In the language of Regge theory [4,5] this diffractive exchange is identified with a Regge trajectory, the Pomeron.

Early experimental evidence showed that the total $p\bar{p}$ cross-section actually increases with increasing s [6]. The cross-section must then be dominated at high energies by the diffractive exchange. In the Standard Model an object with the properties of a diffractive exchange can exist, for example a glueball; experimental searches for such a state have yielded one candidate [7].

At HERA, deeply inelastic scattering (DIS) of virtual photons off protons is used to study the structure of the proton. The photon, with virtuality Q^2, couples to a point-like constituent of the proton, a parton, and the interaction can be calculated using the quantised theory of electromagnetism, Quantum Electrodynamics (QED). The theory of strong interactions, Quantum Chromodynamics (QCD), can be used to calculate the short-distance strong interac-

tions of the partons. However, at large distances the strong coupling constant becomes so large that perturbation theory cannot be used and this part of the cross-section is described by phenomenologically derived parton density functions (PDFs): the cross-section has been factorised. These PDFs cannot be derived from first principles but their behaviour as a function of Q^2 can be predicted using QCD.

DIS can also be used to probe the structure of diffractive exchanges. Diffractive PDFs can be defined in analogy with the case for a proton [8]; in the Resolved Pomeron Model [9] they are Pomeron PDFs. Again, QCD can be used to predict the Q^2 behaviour of these PDFs and in order to test these predictions it is necessary to measure across as wide a range of Q^2 as possible. The measurement presented in this thesis extends the kinematic phase-space of diffractive DIS measurements to the highest ever Q^2.

The use of Object-Oriented (OO) programming techniques as a means of dealing with the huge amounts of information necessary to perform a physics analysis is now firmly established. Accordingly, the H1 collaboration has undertaken a project to reimplement the physics analysis software and data-storage in C++. The measurement presented in this thesis was produced with a new generic OO analysis framework. The framework is designed such that it can also be and is used to easily perform very different physics analyses from the analysis presented here. This is crucial in the efficient production of physics analyses by a large high energy physics collaboration.

After a theoretical overview in the first chapter of this thesis the H1 detector used to make the measurement is described. The third chapter details the method used to first select the high Q^2 DIS event sample and then the diffractive DIS subsample of these events. In the next chapter the method used to analyse the data sample and extract the diffractive DIS cross-section is presented. In the penultimate chapter the diffractive DIS cross-section results are presented and compared to several QCD-based models of diffraction. Finally, the generic OO analysis framework used to perform the analysis is presented.

Chapter 1

Diffractive DIS at HERA

In this chapter the basic concepts of DIS in electron-proton interactions are introduced. The use of the QCD hard-scattering factorisation theorem [10] as a basis for understanding hadronic structure in terms of phenomenologically derived parton density functions convoluted with perturbatively calculable hard-scattering cross-sections is outlined.

The topic of diffraction is then introduced and a brief summary of Regge theory [4, 5] given. Based on an analogy with inclusive DIS processes the use of diffractive DIS processes to study the structure of diffractive exchanges is described. The extension of the QCD hard scattering factorisation theorem to include diffractive DIS processes is discussed together with the Regge factorisation hypothesis. Next, synopses of several theoretical models of diffraction are presented along with the simulations of these models. Finally, an overview of the techniques involved in the simulation of ep interactions is given; only those models directly compared to the data will be described in detail.

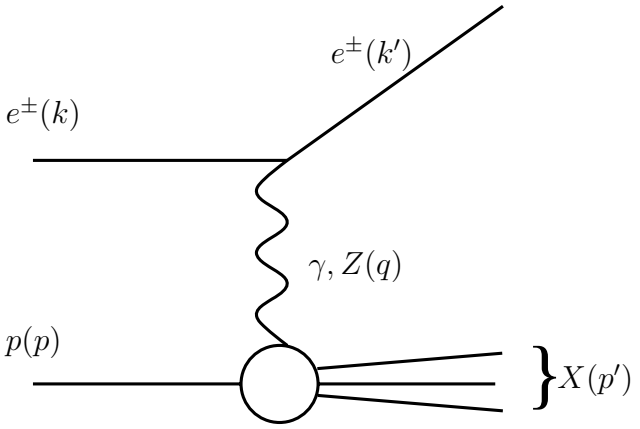

Figure 1.1: *A Standard Model diagram of a NC DIS process at HERA. The four-momenta of the particles are shown in parentheses.*

1.1 DIS at HERA

1.1.1 The Kinematics of DIS Processes

Deeply inelastic scattering of electrons off protons can proceed via either a neutral or charged current exchange. The Neutral (NC) and Charged Current (CC) reactions proceed as $ep \to e'X$ and $ep \to \nu X$, respectively. For NC the outgoing lepton is an electron whilst in the case of CC interactions it is a neutrino. In both reactions X represents the resulting hadronic system. The Standard Model of Particle Physics [11] describes these two processes as being mediated by a spin-1 boson; in the case of NC this can either be a photon or a Z boson while in the case of CC it is a W boson. In the analysis presented in this thesis only NC interactions are considered.

Shown in figure 1.1 is the diagram of the Standard Model representation of NC interactions at HERA; particle types are shown accompanied by momenta labels in parentheses. Here, k and k' represent the four-momenta of the incoming and outgoing electrons, respectively, and the exchanged boson has four-momentum q. The momentum of the incoming proton is p, while p' is the momentum of the hadronic system X, also known as the "proton remnant".

Two kinematic variables are required to describe a DIS process. Variables

that are commonly used are:

$$Q^2 = -q^2 = -(k - k')^2, \qquad x = \frac{Q^2}{2p \cdot q}, \qquad y = \frac{p \cdot q}{p \cdot k}. \tag{1.1}$$

Here Q^2 is the virtuality of the exchange boson, x is the Bjorken scaling variable and y the inelasticity. They are related to the ep centre of mass energy $\sqrt{s}$ by the equation $Q^2 = sxy$ (neglecting the proton and electron masses).

The wavelength of the exchange boson is related to its virtuality via $\lambda \sim \frac{1}{Q}$, so that as Q^2 increases ever smaller structures within the proton are resolved. Nuclear scattering experiments suggest that the proton has an effective size of ≈ 1 fm [12] which corresponds to a $Q^2 \sim 1$ GeV^2. For larger values of Q^2 the virtual boson can be thought of as resolving sub-structure within the proton. This is known as the DIS regime. The virtual boson then couples to a constituent of the proton, known as a parton.

The physical interpretation of x, in the infinite momentum frame of the proton, is that it is the fractional momentum of the proton carried by the struck parton [12]. Similarly, in the proton rest frame, the variable y can be thought of as the fractional momentum of the electron carried by the virtual boson.

1.1.2 Cross-sections, Structure Functions and the Reduced Cross-Section

The NC cross-section can be expressed differentially in x and Q^2 in terms of two structure functions [11], $F_2(x, Q^2)$ and $F_L(x, Q^2)$[1], as shown in equation 1.2.

$$\frac{\mathrm{d}^2\sigma_{ep\to e'X}}{\mathrm{d}x\mathrm{d}Q^2} = \frac{2\pi\alpha_{em}^2}{xQ^4}\left[\left(1 + (1-y)^2\right)F_2(x, Q^2) - y^2 F_L(x, Q^2)\right]. \tag{1.2}$$

[1] Z and γZ interference terms are suppressed by factors of $\left(\frac{Q^2}{Q^2+M_Z^2}\right)$ or more and so are small or negligible given the Q^2 range considered in this analysis. For clarity of discussion these contributions are not discussed in any detail here. The expressions for the reduced cross-section given in 1.3 and 1.21 can be generalised to include Z and γZ contributions which can then be used in 1.4 and 1.20 respectively, see for example [13].

The structure function F_2 will be discussed further in section 1.1.3. The structure function F_L parameterises the contribution to the total cross-section from longitudinally polarised photons and, owing to the positivity constraint on the cross-section, it can range from $0 < F_L < F_2$. It is experimentally constrained to be small in most regions of phase-space and measurements show that, as expected, it only contributes significantly to the total cross-section at high y [14].

Nevertheless any measurement of the NC cross-section will include contributions from both F_2 and F_L and so it is useful to introduce a reduced cross-section defined as:

$$\sigma_r(x, Q^2) = F_2(x, Q^2) - \frac{y^2}{1 + (1 - y)^2} F_L(x, Q^2). \tag{1.3}$$

The differential NC cross-section can then be expressed as a function of fundamental constants, kinematic quantities and the reduced cross-section, as shown in equation 1.4.

$$\frac{\mathrm{d}^2\sigma_{ep\to e'X}}{\mathrm{d}x\mathrm{d}Q^2} = 2\pi\alpha_{em}^2 \frac{1 + (1 - y)^2}{xQ^4} \sigma_r(x, Q^2). \tag{1.4}$$

1.1.3 The Quark Parton Model

The Rutherford scattering formula [11] which describes the scattering of two point-like objects has no dependence on any quantity with units of length and so the cross-section is said to "scale". Assuming that ep DIS interactions proceed via the exchange of a pointlike virtual photon scattering off some pointlike constituent of the proton then the cross-section should exhibit scaling and have no dependence on Q^2.

Early experimental evidence supported this prediction [15, 16] and led theorists to identify the point-like constituents of the proton with Gell-Mann's quarks [17]. The three generations of quarks as defined in the Standard Model are shown in table 1.1. Simply by considering the proton's charge quantum number (= +1), the fact that the proton is a baryon (a qqq combination) and

1st generation	2nd generation	3rd generation	Charge	Baryon Number
Up (u)	Charm (c)	Top (t)	+2/3	+1/3
Down (d)	Strange (s)	Bottom (b)	-1/3	+1/3

Table 1.1: *The 3 generations of quarks; their symbols are given in parentheses.*

the lack of evidence for proton decay leads to the obvious choice for the quark structure of the proton to be uud.

In the Quark Parton Model (QPM) the structure function $F_2(x, Q^2)$ can be related to the density of quarks within the proton. PDFs are defined for quarks, $q_i(x)$ and anti-quarks, $\bar{q}_i(x)$. The PDFs represent the probability of finding a quark of type i and momentum fraction x within the proton. They obey the relation:

$$F_2(x, Q^2) = x \sum_i e_i^2 \{q_i(x) + \bar{q}_i(x)\} \tag{1.5}$$

where the index i represents the six different quark flavours given in table 1.1 and e is the electromagnetic charge of the quark. Thus F_2 gives a measure of the total quark content of the proton and it can be seen that in addition to the uud valence quark structure needed to account for the quantum numbers of the proton there can also be contributions from so-called "sea quarks"; these sea quarks can appear in $q\bar{q}$ pairs, thus leaving the overall quantum numbers of the proton unchanged. In the QPM the quarks are non-interacting; the theory which describes the strong interactions of the quarks is introduced in the next section.

1.2 Quantum Chromodynamics

The degree of freedom ascribed to the strong interactions is called "colour" and has three basic states, often referred to as "red, blue and green". All

physically observable states are colourless, i.e. they are colour singlets, and furthermore only $q\bar{q}$ and qqq states are observed in nature. The quantum field theory which describes "colour" is called Quantum Chromodynamics (QCD) and to explain the observed behaviour of strong interactions QCD is based upon the $SU(3)_c$ gauge group [11].

The exchange particles which mediate strong interactions are massless spin-1 bosons called gluons. Quarks carry one colour-charge each whilst gluons carry approximately twice the colour-charge in eight combinations. Thus, unlike the photons of QED, gluons can self-interact. This self-coupling, or non-Abelian, behaviour results in the phenomenon called asymptotic freedom. At small distances, $r \to 0$, the strong force $F_{QCD} \to 0$, and so at sufficiently high values of Q^2 the partonic constituents of a hadron can be thought of as being free. Conversely, at large distances, or small Q^2, the strong force increases dramatically, resulting in the property of confinement, or infrared slavery, which explains why no free colour-charges are observed in nature.

The theory of perturbative QCD (pQCD) can be used to perform a calculation of a cross-section up to a given order in the strong coupling parameter, α_s. At leading order (LO) the dependence of α_s on the renormalisation scale μ_R^2 is:

$$\alpha_s(\mu_R^2 = Q^2) = \frac{12\pi}{(33 - 2n_f)\ln(Q^2/\Lambda^2_{\rm QCD})}$$

where $\Lambda_{QCD} \simeq 200$ MeV and can be thought of as the scale at which the strong interactions become strong[1]. At large Q^2, α_s is small and perturbation theory can be used safely. However, for $Q^2 \lesssim \Lambda^2_{QCD}$ it can be seen that α_s becomes large and the perturbative approach is no longer reliable.

1.2.1 QCD Hard Scattering Factorisation

The QPM needs to be modified to account for QCD interactions, in particular the radiation of gluons from the quarks. Furthermore, pQCD calculations can

[1]The choice of scale here is an arbitrary one, the only requirement is that $\mu_R^2 >> \Lambda^2_{QCD}$; in DIS Q^2 is a convenient choice.

only be safely performed when the scale of the interaction is large enough. The cross-section must be factorised into a perturbatively calculable (hard) part, where pQCD can be applied, and a non-perturbatively calculable (soft) part. Any soft processes, where the momentum transfer is small, appear frozen when viewed from a hard process, where the momentum transfer is large[2]. The modified structure function has the form:

$$F_2(x,Q^2) = \sum_i \int_x^1 \mathrm{d}x' \sigma(\frac{x}{x'}, Q^2, \mu_F^2) \ \left[q_i(x',\mu_F^2) + \bar{q}_i(x',\mu_F^2)\right] \tag{1.6}$$

where $\sigma(\frac{x}{x'}, Q^2, \mu_F^2)$ is the hard-scattering cross-section for a quark of type i and momentum x' and a photon with virtuality Q^2; this hard process is calculable in pQCD. The modified PDFs, $q_i(x',\mu_F^2)$ and $\bar{q}_i(x',\mu_F^2)$, now represent the probablity of finding a quark of momentum fraction x' within the proton at the factorisation scale μ_F^2. The fractional momentum of the quark involved in the hard-scatter is x by definition, but a quark with momentum x' can lower its momentum to x via gluon emission. Thus any quark with a fractional momentum ranging between x and 1 can contribute, making the integral necessary. The factorisation scale μ_F^2 is the scale below which this gluon emission is defined to be a soft process and is absorbed into the PDFs.

Importantly, the PDFs thus defined are completely process-independent and can therefore be measured in one process and applied to another. This universality property means that the PDFs of the proton measured at HERA should be able to describe any other process involving protons, whether it be ep interactions at HERA, $p\bar{p}$ interactions at the Tevatron or pp at the LHC.

1.2.2 The DGLAP Evolution Equations

Although the PDFs are not themselves calculable from first principles it is still possible to apply pQCD in calculating their evolution. Several evolution schemes exist, most notably the DGLAP [18–21], BFKL [22, 23] and

[2]One of the Heisenberg uncertainty relations states that $\Delta E \Delta t \geq \hbar/2$ so small energy scales correspond to long time scales and vice versa.

CCFM [24–26] schemes, each having regions of phase-space in which they are valid. The DGLAP evolution scheme has been proven to describe all structure function measurements at HERA, e.g. [14], and has also allowed precision measurements of the strong coupling parameter α_s [27]. Owing to this and given that the DGLAP scheme is the only scheme available for comparison [28, 29], only the DGLAP scheme is considered in this analysis.

The DGLAP evolution equations describe the evolution in $\ln Q^2$ of the PDFs in section 1.2.1. In addition to the quark PDFs considered there gluon PDFs, $g(x, \mu^2)$, can also be defined. The DGLAP equations then have the form [12]:

$$\frac{\partial q(x,t)}{\partial t} = \frac{\alpha_s(t)}{2\pi} \int_x^1 \frac{\mathrm{d}y}{y} \left[q(y,t) P_{qq}(\frac{x}{y}) + g(y,t) P_{qg}(\frac{x}{y}) \right] \quad (1.7)$$

$$\frac{\partial g(x,t)}{\partial t} = \frac{\alpha_s(t)}{2\pi} \int_x^1 \frac{\mathrm{d}y}{y} \left[q(y,t) P_{gq}(\frac{x}{y}) + g(y,t) P_{gg}(\frac{x}{y}) \right] \quad (1.8)$$

where $t = \ln(Q^2)/\Lambda_{\mathrm{QCD}}$ and $P_{ab}(x/y)$ are the splitting functions which represent the probability of finding a parton a with momentum x originating from a parton b with momentum y. For example, the gluon Bremsstrahlung process $q \to qg$ which modifies the quark distributions is represented by the two splitting functions $P_{qq}(x/y)$ and $P_{qg}(x/y)$, and similarly for modifications to the gluon distributions, as shown in figure 1.2.

1.2.3 Testing QCD - The Structure of the Proton

The QCD picture of the proton predicts there to be contributions from:

- The three valence quarks, uud;
- Gluons, arising from QCD interactions between partons;
- Sea-quarks, arising from $g \to q\bar{q}$ processes.

These contributions can be parameterised and fitted to the data at a particular scale. The DGLAP evolution equations can then be used to predict

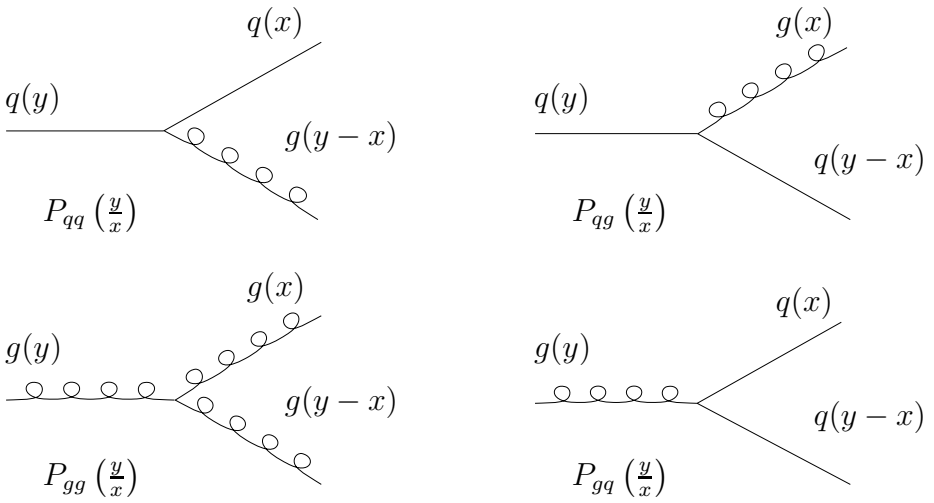

Figure 1.2: *Diagrams which show the four terms which modify the quark (top left,right) and gluon (bottom left, right) PDFs.*

the PDFs at a different scale, provided the new scale remains in the region of validity of pQCD. In order to test the predictions of QCD it is necessary therefore to measure across as broad a range of Q^2 as possible.

The full QCD picture is now available with which it should be possible to completely describe the structure of the proton. Figure 1.3 shows the degree to which that description works. The Bjorken scaling prediction is seen to be violated as x decreases, which can be interpreted in the following way: As Q^2, the resolving power, increases it is possible to resolve more and more of those partons which carry small fractions of the proton momentum; this explains the rise of F_2 at low x. To conserve total momentum this means that, conversely, less objects carrying large fractions of the proton momentum must be observed; this explains the fall of F_2 at high x.

The objects carrying small fractions of the proton's momentum are identified with the gluons (which interact with the photon via $g \rightarrow q\bar{q}$) and the scaling violations seen in Figure 1.3 are indirect evidence for them. Integrating the PDFs over x reveals that only $\sim 50\%$ of the proton's momentum is carried by quarks [12], suggesting that the remainder is carried by gluons.

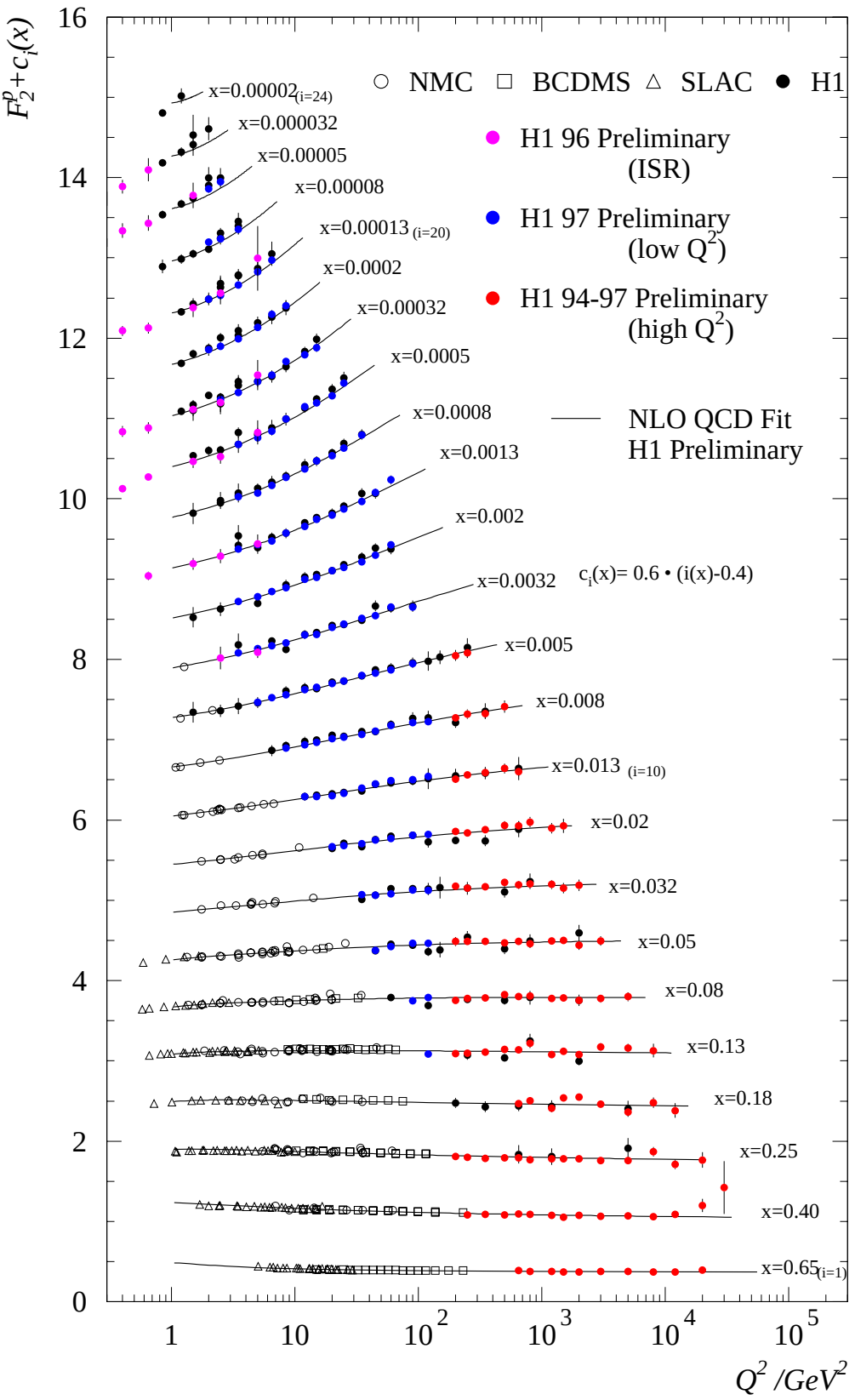

Figure 1.3: *Measurements of the proton structure function F_2 as a function of Q^2 in bins of x compared to a QCD fit using the DGLAP evolution scheme.*

1.3 Diffraction

In this section a short review of scattering in quantum mechanics is presented and the subject of Regge theory [4, 5] is introduced. Next the topics of Regge phenomenology and diffractive exchanges are introduced along with the Pomeron.

1.3.1 Two-Body to Two-Body Scattering in Quantum Mechanics

Any two-body to two-body process can be described quantum mechanically in terms of a unitary scattering matrix $\mathcal{S}$ such that the amplitude, $\mathcal{A}$, for the process is:

$$\mathcal{A} = \langle cd|\mathcal{S}|ab\rangle \tag{1.9}$$

where ab and cd represent the initial and final two-body states respectively. The Mandelstam variables are defined in terms of the four-momenta of the particles [12]:

$$s = (p_a + p_b)^2 \tag{1.10}$$

$$t = (p_a - p_c)^2 \tag{1.11}$$

$$u = (p_a - p_d)^2 \tag{1.12}$$

where p_a represents the four-momentum of particle a, etc.

1.3.2 Regge Theory

In the asymptotic limit where $s \gg |t|$, the so-called Regge region or limit, the amplitude for the 2 body to 2 body process can be written as [30]:

$$\mathcal{A}(s,t) \propto s^{\alpha(t)} \tag{1.13}$$

which can be interpreted as an exchange in the t-channel of an object with angular momentum $\alpha(t)$, shown in figure 1.4. Chew and Frautschi [31, 32]

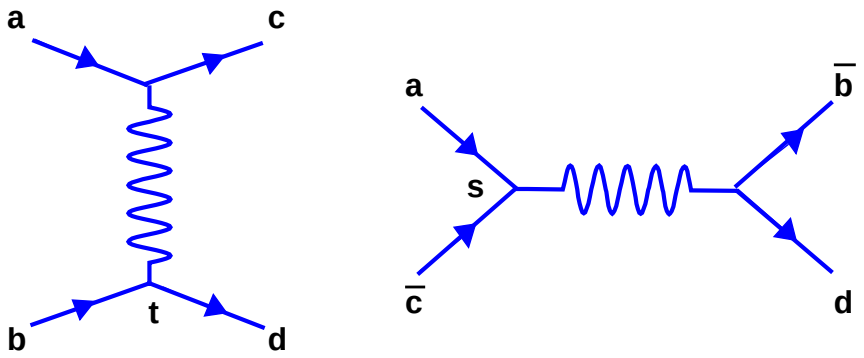

Figure 1.4: *The process $ab \rightarrow cd$ viewed as a t-channel exchange (left) and the equivalent s-channel process (right).*

plotted the spins of low-mass mesons against their square mass ($= t$) and noticed that they lie on a straight line, as shown in figure 1.5. This implies that α is a linear function of t and defines a so-called Regge trajectory

$$\alpha(t) = \alpha(0) + \alpha' t. \tag{1.14}$$

It can be shown [30] that, in the Regge limit, the total cross-section is related to s via:

$$\sigma_{tot} \propto s^{(\alpha(0)-1)}. \tag{1.15}$$

The ρ family of mesons shown in figure 1.5 have an intercept $\alpha(0) \approx 0.5$, resulting in the cross-section for this exchange decreasing as s increases.

1.3.3 Diffraction and the Pomeron

Pomeranchuk proved [1,2] that in any process in which there is charge exchange the cross-section vanishes asymptotically. Conversely, Foldy and Peierls proved [3] that for any process in which the cross-section does not fall as s increases that process must be dominated by the exchange of vacuum quantum numbers.

The pp and $p\bar{p}$ total cross-sections were seen experimentally to rise at large s as s increases, as shown in figure 1.6. At large s the interaction must be dominated by vacuum quantum number exchange which is referred to as a

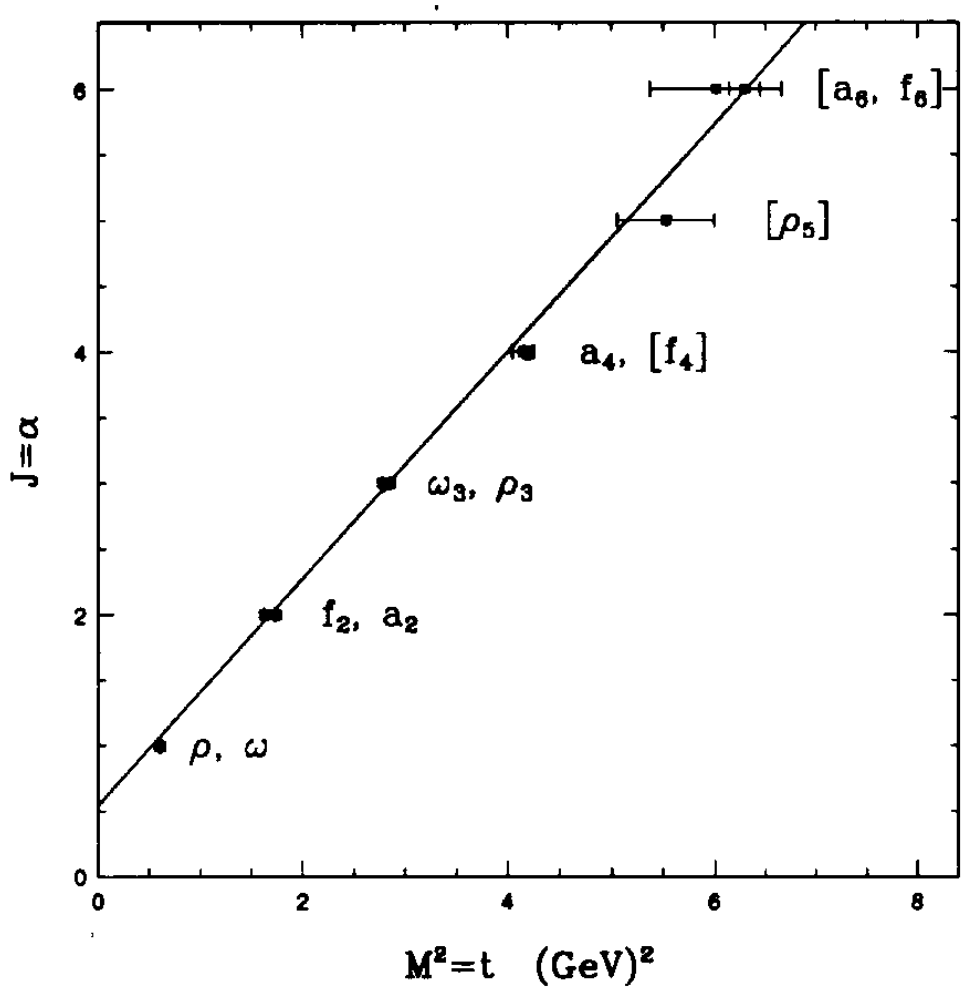

Figure 1.5: *The Chew-Frautschi plot.*

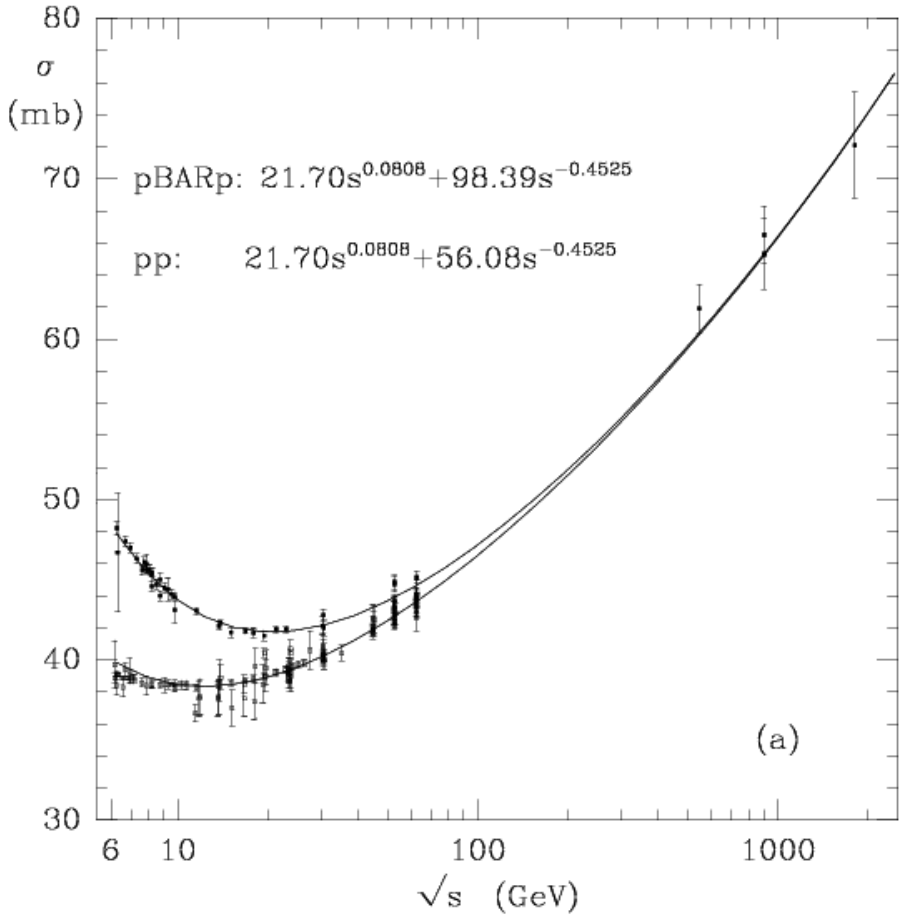

Figure 1.6: *The pp and $p\bar{p}$ total cross-sections as a function of $\sqrt{s}$ compared with the Donnachie-Landshoff parameterisation.*

diffractive exchange. In the Regge picture this is attributed to a Regge trajectory with an intercept $\alpha(0) > 1$, a trajectory named the Pomeron. Donnachie and Landshoff [6] performed a simple fit to the *pp* and $p\bar{p}$ data of the form:

$$\sigma = As^{\alpha_{IP}(0)-1} + Bs^{\alpha_{IR}(0)-1} \tag{1.16}$$

representing a Pomeron trajectory and a sub-leading Reggeon trajectory. The result of the fit is shown in figure 1.6. The sub-leading Reggeon trajectory can be identified as that shown in figure 1.5.

1.4 Diffractive DIS at HERA

It is possible to use DIS to study the structure of diffractive exchanges in an analogous way to the use of DIS to study the structure of the proton. Diffractive exchanges are characterised by the fact that there are no quantum numbers exchanged overall. In the case of ep scattering the diffractive interaction can be viewed as the 2 body to 2 body process $\gamma^* p \longrightarrow Xp$, i.e. the proton emerges quasi-elastically from the scatter. The hadronic system X, resulting from the hard photon-diffractive exchange interaction, is separated in the laboratory frame from the quasi-elastic proton p as there is no colour-connection between the two systems. This absence of the production of hadrons is called a "rapidity gap" and can be used to identify diffractive events.

1.4.1 Diffractive Kinematics

Figure 1.7 shows the diagram for the generic diffractive DIS process at HERA. Further to the kinematic variables defined in 1.1.1 and the Mandelstam variables the kinematic variables $x_{I\!P}$ and β are useful in describing the interaction. They are defined as:

$$\beta = \frac{Q^2}{Q^2 + M_X^2 - t} \tag{1.17}$$

$$x_{I\!P} = \frac{Q^2 + M_X^2 - t}{Q^2 + W^2 - M_p^2} \tag{1.18}$$

$$= \frac{x}{\beta} \tag{1.19}$$

where M_X is the invariant mass of the hadronic system X, M_p is the mass of the proton and $W^2 = (q+p)^2$ is the square of the centre of mass of the photon-proton system. Assuming that the diffractive exchange can be attributed to a QCD object, i.e. a Pomeron, then $x_{I\!P}$ is the fractional momentum of the Pomeron with respect to the proton and β is the fractional momentum of the struck parton with respect to the Pomeron.

M_Y, the mass of the Y system, can also in principle be measured. However, in this analysis both M_Y and t are not measured but are constrained to be

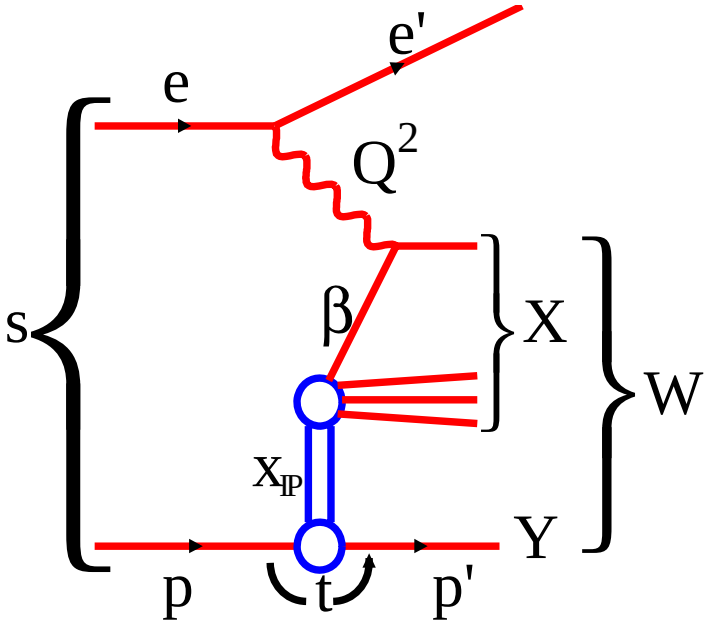

Figure 1.7: *Schematic of the generic diffractive DIS process at HERA.*

small, allowing an increase in the statistics of the event sample (see section 3.2).

1.4.2 Diffractive Cross-Sections, Structure Functions and Reduced Cross-Sections

Following the same formalism as that given in 1.1.2 the differential cross-section for diffractive DIS, as a function of the three measured kinematic variables, can also be expressed in terms of a reduced cross-section , $\sigma_r^{D(3)}(\beta, Q^2, x_{IP})$:

$$\frac{d^3\sigma_{ep\to eXp}}{d\beta dQ^2 dx_{IP}} = \frac{4\pi\alpha_{em}^2}{\beta Q^4}\left(1 - y + \frac{y^2}{2}\right)\sigma_r^{D(3)}(\beta, Q^2, x_{IP}) \tag{1.20}$$

where the same notation as in equation 1.4 has been used. Again the reduced cross-section can be related to the structure functions by:

$$\sigma_r^{D(3)}(\beta, Q^2, x_{IP}) = F_2^{D(3)}(\beta, Q^2, x_{IP}) - \frac{y^2}{1 + (1-y)^2} F_L^{D(3)}(\beta, Q^2, x_{IP}). \tag{1.21}$$

1.5 Factorisations and Models of Diffraction

In order to investigate the QCD structure of the diffractive exchange using the DGLAP formalism it is necessary to factorise the kinematical dependencies of $\sigma_r^{D(3)}(\beta, Q^2, x_{IP})$ such that only the x and Q^2 dependencies remain. The x and Q^2 behaviour can then be predicted using the DGLAP equations.

1.5.1 QCD Hard Scattering Factorisation for Diffractive DIS

It has been proven by Collins [8] that the diffractive $\gamma^* p$ cross-section can be written in terms of diffractive PDFs, $q(x, Q^2, x_{IP}, t)$, which are now dependent on four kinematic variables, convoluted with a hard-scattering cross-section:

$$\sigma(\gamma^* p \to Xp) \;\sim\; q(x_{IP}, t, x, Q^2) \;\otimes\; \hat{\sigma}_{\gamma^\star q}(x, Q^2). \tag{1.22}$$

At fixed x_{IP} and t these PDFs will evolve with Q^2 and x in exactly the same way as the proton PDFs in equation 1.8. Such a proof allows a full QCD fit to the data with no additional assumptions.

1.5.2 Regge Factorisation and the Resolved Pomeron Model

In the Regge factorisation scheme the extra assumption that the diffractive PDFs do not depend (other than in normalisation) on x_{IP} and t is made. Instead the interaction factorises into a term which describes the flux of Pomerons from the proton and a hard scatter of the photon with the Pomeron, as illustrated in figure 1.8. This factorisation scheme is based on physical intuition; the time scales for these two processes are very different. At the proton vertex the relevant scale is t which is small in the diffractive limit. Any dynamics occurring here will appear frozen when viewed from the hard scatter vertex where the relevant scale is Q^2. In the Regge factorisation scheme the hard

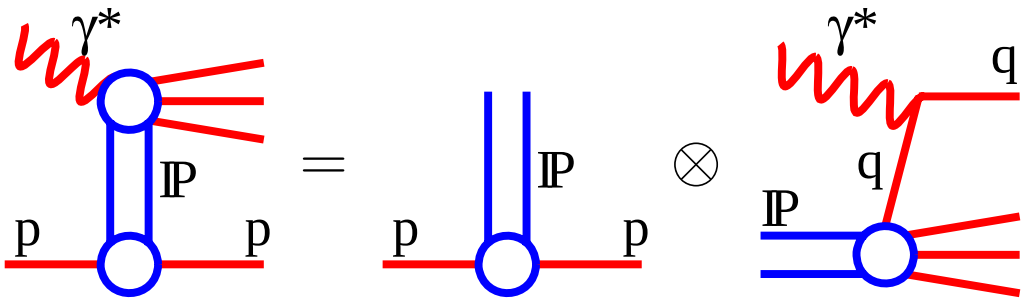

Figure 1.8: *A sketch of the Regge factorisation scheme. The diffractive exchange is factorised into a flux component (long time scales) and a hard scatter component (short time scales).*

scatter depends only on $\beta(=\frac{x}{x_{IP}})$ and Q^2 while the flux term depends only on x_{IP} and t:

$$\sigma(\gamma^* p \to Xp) \;\sim\; f_{IP}(x_{IP}, t) \;\otimes\; p_{IP}(\beta, Q^2) \;\otimes\; \hat{\sigma}_{\gamma^* q}(\beta, Q^2) \tag{1.23}$$

where $f_{IP}(x_{IP}, t)$ represents the flux term, $p_{IP}(\beta, Q^2)$ represent Pomeron PDFs and $\hat{\sigma}_{\gamma^* q}(\beta, Q^2)$ represents the virtual photon-quark hard-scatter. The reduced cross-section $\sigma_r^{D(3)}$ can then be written as:

$$\sigma_r^{D(3)}(\beta, Q^2, x_{IP}) = f_{IP}(x_{IP})\; \sigma_r^{IP}(\beta, Q^2) \tag{1.24}$$

where σ_r^{IP} defines the reduced cross-section of the Pomeron.

There is strong experimental support for Regge factorisation at HERA, e.g. [28, 29, 33]. Figure 1.9 shows the logarithmic Q^2 derivative of $\sigma_r^{D(3)}$ for three bins of x_{IP}, where the x_{IP} dependence has been removed by division of a flux factor, $f_{IP}(x_{IP}, t)$. The data suggest that the $f_{IP}(x_{IP}, t)$ factor contains all of the x_{IP} dependence.

Regge phenomenology [9] leads to a parameterisation of the flux factor:

$$f_{IP}(x_{IP}) = \int_{t_{cut}}^{t_{min}} \frac{e^{Bt}}{x_{IP}^{2\alpha(t)-1}} \mathrm{d}t \tag{1.25}$$

where $t_{cut} = -1.0$ GeV^2 defined by the selection technique in section 3.2 and t_{min} is the minimum kinematically allowed value.

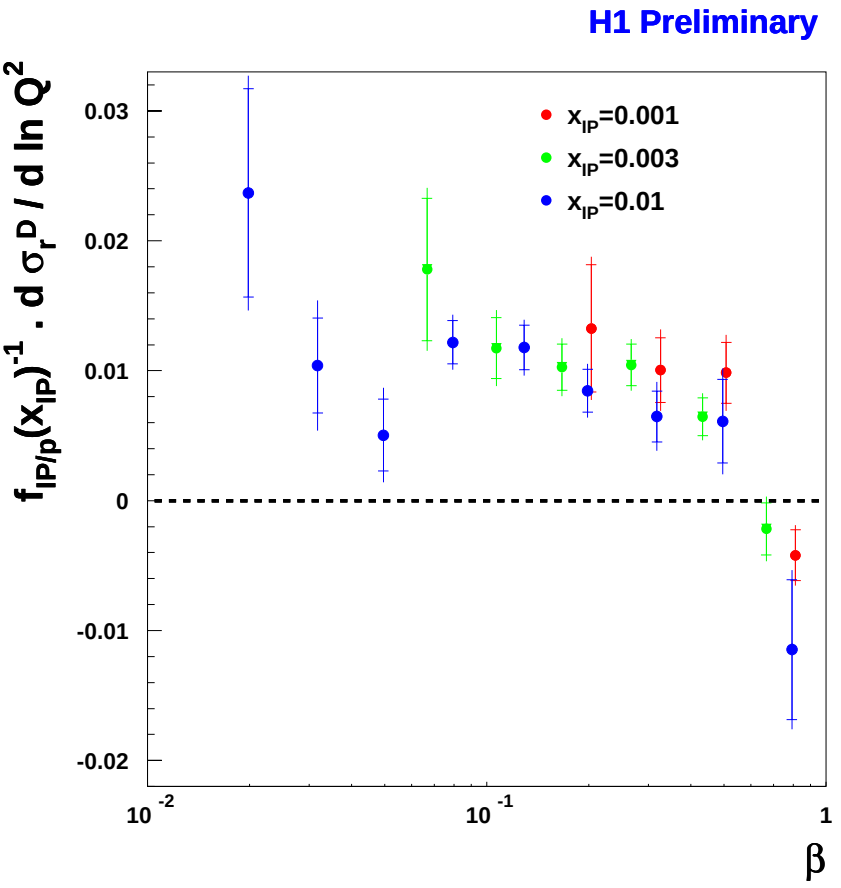

Figure 1.9: *The logarithmic Q^2 derivative of $\sigma_r^{D(3)}$ at three values of fixed x_{IP}, multiplied by $f_{IP}(x_{IP}, t)^{-1}$, as a function of β.*

In addition to the leading Pomeron trajectory it is necessary, at higher values of x_{IP}, to include a sub-leading reggeon trajectory, that shown in figure 1.5, which survives by virtue of its relatively large value of $\alpha(0)$. The full parameterisation of the data is then:

$$\sigma_r^{D(3)}(\beta, Q^2, x_{IP}) = f_{IP}(x_{IP})\sigma_r^{IP}(\beta, Q^2) + f_{IR}(x_{IP})\sigma_r^{IR}(\beta, Q^2) \tag{1.26}$$

1.5.3 Soft Colour Interactions

In the model of Soft Colour Interactions (SCI) of Edin, Ingelman and Rathsman [34,35] the assumption is that the underlying hard interaction is the same for both diffractive and non-diffractive events. In the diffractive case there is a subsequent soft interaction where colour but not momentum are transferred, such that the overall $\gamma^* p$ interaction involved no net exchange of colour. This soft interaction can be pictured as the rearrangement of colour strings, shown in figure 1.10. The simplest version of the model is governed by one free parameter which is the probability of this soft interaction occurring.

A modification to this model uses a Generalised Area Law (GAL) [36]. In this model configurations where a colour string spans a large area in energy-momentum space are exponentially suppressed and so the probability P for a string rearrangement is given by:

$$P = R_0(1 - \exp -b\Delta A) \tag{1.27}$$

where R_0 and b are the two parameters of the model and ΔA is the difference between the areas spanned by the string before and after rearrangement.

1.5.4 The Semi-Classical Model

In the proton rest frame the $\gamma^* p \longrightarrow Xp$ interaction can be interpreted as the fluctuation of the virtual photon into a partonic state a long way from the proton; this partonic state then interacts with the proton. Shown in figure 1.11 are the dominant states, $q\bar{q}$ and $q\bar{q}g$, as viewed in the proton rest frame (left) and the infinite momentum frame of the proton (right).

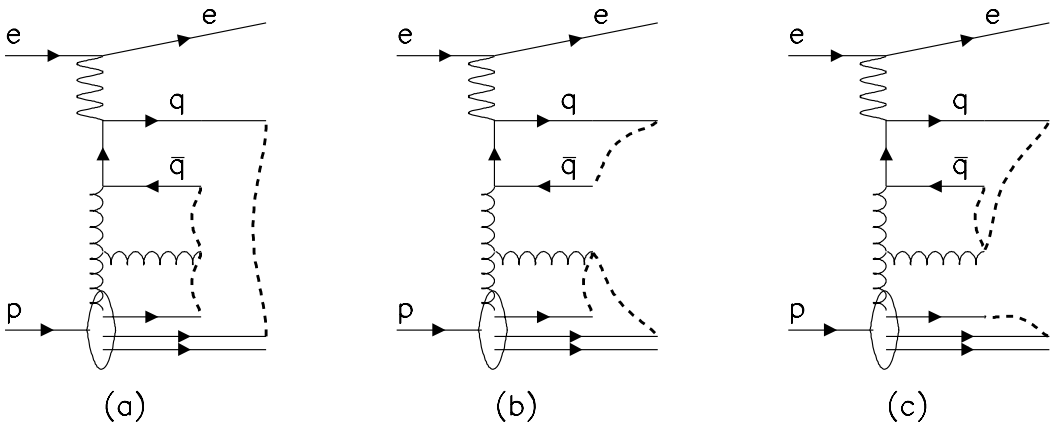

Figure 1.10: *Diagrams showing string configurations in a DIS event when a.) strings connect the hadronic system leaving no rapidity gaps, b.) and c.) soft colour interactions rearrange the strings creating rapidity gaps.*

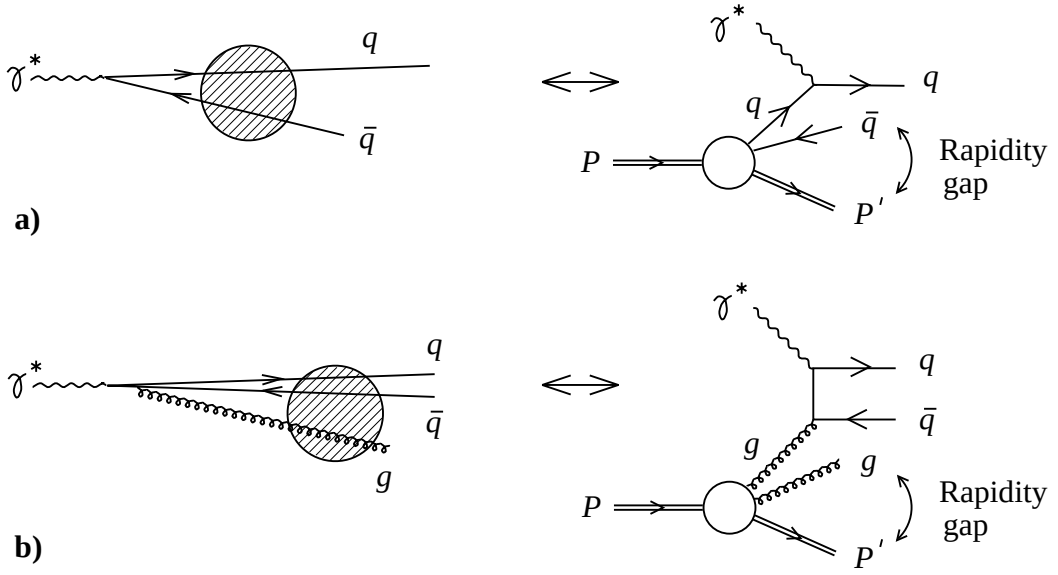

Figure 1.11: *The $q\bar{q}$ and $q\bar{q}g$ states of the virtual photon as viewed in the proton rest frame (left) and the same process as viewed in the infinite momentum frame of the proton (right) .*

In the Semi-Classical Model of Buchmuller, Gehrmann and Hebecker [37] the photon fluctuates into one of the $q\bar{q}$ or $q\bar{q}g$ partonic states; this then scatters off the proton which is modelled as a superposition of colour fields. If the resulting partonic state is an overall colour-singlet then the interaction was diffractive as there was no net colour exchange.

1.6 Simulating ep Interactions

In order to correct the data[1] and compare the data to the various theoretical models Monte Carlo (MC) methods are used employing the following strategy.

- Firstly, PDFs, extracted from a previous measurement, are evolved to the relevant scale.
- The hard process of interest, e.g. a virtual photon scattering from a quark, is then calculated at leading order.
- The resulting partons then undergo hadronisation to produce the observed hadrons. In the analysis presented in this thesis this hadronisation step is always performed by the JETSET [38] programme which implements the LUND string model of hadronisation [39].
- Finally these "generator-level" events are passed through a detailed detector simulation and are therefore directly comparable to the data events.

Simulated event samples are generally required to be more than three times the size of the data samples in order to ensure that the statistical error of the simulated sample can be, to a good approximation, ignored.

[1] See section 4.3 for a discussion on correcting the data using simulations.

1.6.1 The Models Used in this Analysis

Models used for DIS

The DJANGO [40] programme was used to simulate $\sim 400,000$ inclusive DIS events. This programme is an interface between the HERACLES [41] ep event generator and the ARIADNE [42] implementation of the Colour Dipole Model [42–45], used to generate QCD radiation. The input PDFs used were extracted from a next-to-leading order (NLO) QCD DGLAP fit to a previous measurement of F_2 made with the H1 detector [46].

Models used for Diffractive DIS

The RAPGAP [47] programme implements the Resolved Pomeron model of diffraction and was used to simulate $\sim 2,800,000$ diffractive DIS events with an elastic proton. QED radiation, detailed in section 1.6.2, is simulated via an interface to the HERACLES programme, while QCD radiation uses an interface to the ARIADNE programme. The input PDFs for the Pomeron component of the process are extracted from a previous H1 measurement under the assumption of Regge factorisation [48]. The sub-leading meson component uses a parameterisation for the π-meson taken from PDFLIB [49, 50]. Finally, the DIFFVM [51] programme was used to simulate diffractive DIS events with proton dissociation in order to correct the cross-section back to the defined kinematic phase-space, detailed in section 4.3.2.

Models used for Background Processes

Elastic QED-Compton events, $ep \to ep\gamma$, can fake NC processes and are modelled by the COMPTON [52] programme. Elastic $\gamma\gamma$ events, $ep \to epl^+l^-$, (LPair) can also fake NC processes, particularly when the final state leptons are an electron-positron pair, and are modelled by the LPAIR [53] programme.

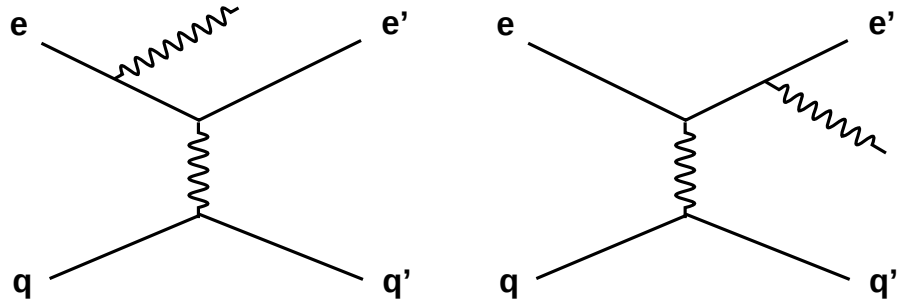

Figure 1.12: *The Diagrams for Initial State Radiation (left) and Final State Radiation (right).*

1.6.2 Simulating QED Radiation

Simulations of QED radiation are used to account for the exchange or emission of photons before, during or after the Born-level process. These processes are enhanced by large $\log Q^2/m_e^2$ terms and in the Leading Logarithmic Approximation (LLA) these terms are assumed to dominate, allowing an analytical calculation to be made. The photon self-energy is accounted for by a running α_{em} and is discussed in no further detail here. Emission of photons from either the incoming or outgoing quark is accounted for by an additional QED term in the DGLAP evolution equations. This contribution is estimated to be small and only at very large x and Q^2 reaches the level of 1%.

The remaining contributions come from emission of photons from the incoming and outgoing lepton, called Initial State Radiation (ISR) and Final State Radiation (FSR) respectively, and are shown in figure 1.12. In addition, virtual loops also contribute despite being higher order. The HERACLES programme is used to simulate these processes.

Chapter 2

HERA and the H1 Detector

The measurement presented in this thesis was made using data taken by the H1 detector [54, 55] at the HERA accelerator at DESY in Hamburg, Germany during 1999 and 2000. This chapter consists of a brief overview of the HERA machine followed by a description of the H1 detector[1] with particular emphasis on those parts of the detector of relevance to this analysis. The final part of this chapter describes briefly the Data Acquisition and Triggering system at H1.

2.1 HERA

The HERA accelerator is a 6.4 km circumference ring situated at DESY in Hamburg, Germany. A schematic view of the HERA accelerator complex is shown in figure 2.1. The main design goal of the accelerator is to collide electrons with protons at a high centre of mass energy to enable precision measurements of QCD. To achieve this HERA consists of two storage rings, one which stores electrons at an energy of 27.6 GeV, the other of which stores protons at an energy of 920 GeV.

The particles in each ring are stored in bunches which consist of approxi-

[1]The H1 Detector has since undergone a major upgrade. The description presented in this chapter is of the H1 Detector as it was during 1999 and 2000.

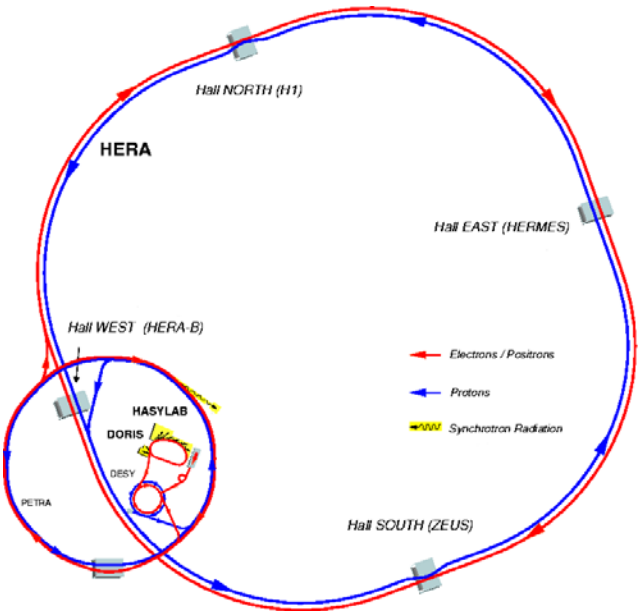

Figure 2.1: The HERA accelerator complex.

mately 10^{11} particles with a Gaussian density distribution of $\sigma \approx 11$ cm. Each ring can store up to 220 bunches and the time between consecutive bunches is 96 ns. These bunches can then be crossed to produce the *ep* interactions of physics interest, henceforth referred to as *ep* interactions, and in good running conditions the number of colliding bunches is ≈ 175. Some of the bunches are left empty, so-called "pilot-bunches", in order to study the backgrounds arising from the beams interacting with residual gas in the beampipe and the beamwall itself.

The two particle beams are brought together at two approximately geometrically opposite points on the HERA ring. Two detectors have been built around these interaction points, the H1 detector at the northerly point and ZEUS at the southerly point. In addition the HERMES experiment has been built at the eastern point where the electron beam is first polarised and then collided with a stationary hydrogen-, deuterium- or helium-gas target for the purpose of measuring the spin-structure of the nucleon.

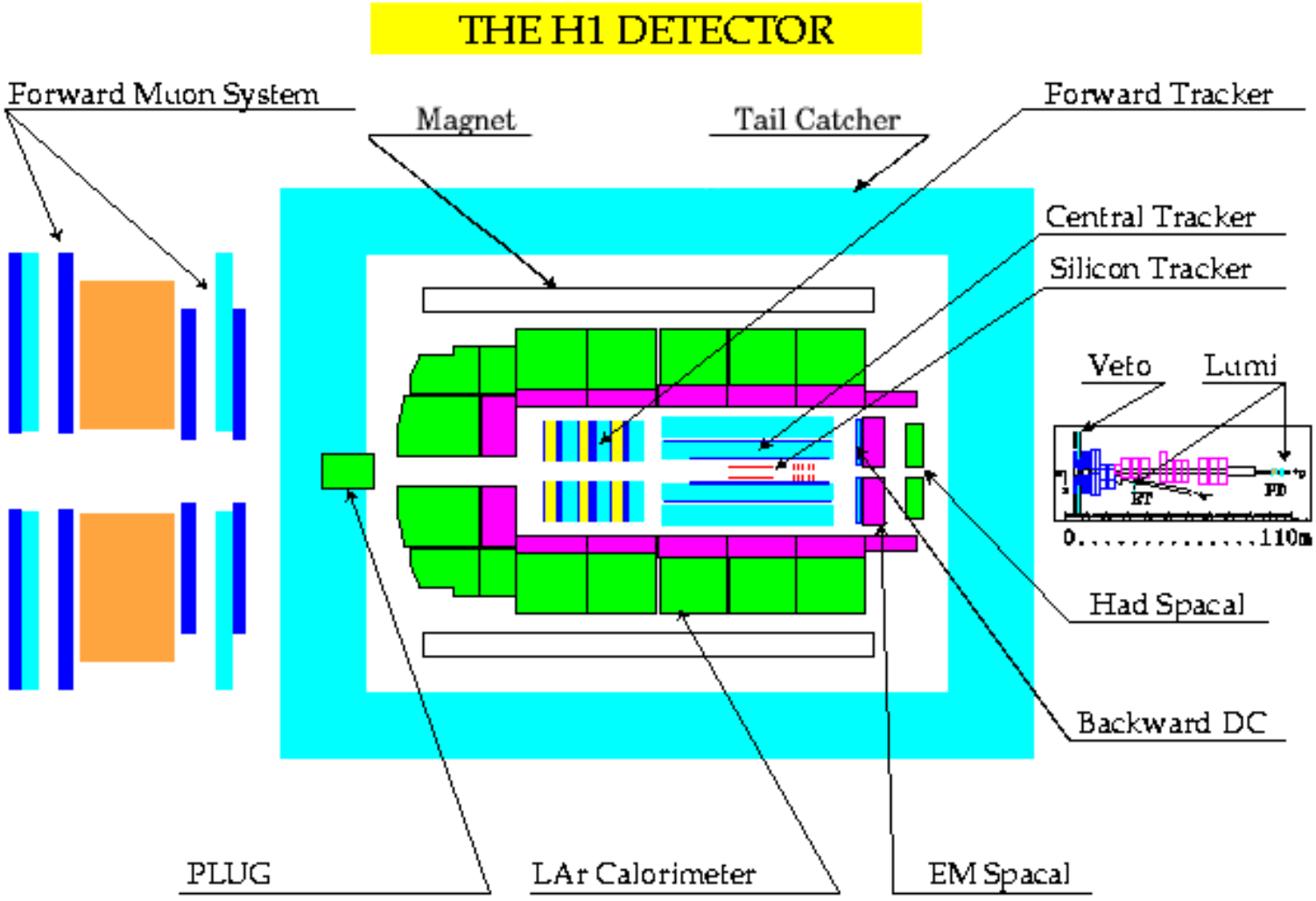

Figure 2.2: A schematic view of the H1 Detector.

2.2 Overview of the H1 Detector

The H1 detector is a multi-purpose detector designed for studying ep interactions produced by the HERA machine. It provides nearly hermetic coverage of the interaction region, the main limitation coming from the space occupied by the beampipe itself. A right-handed Cartesian coordinate system is used to describe the orientation of the detector, such that the z-axis follows the direction of the proton beam, the y-axis points vertically upwards with respect to the Earth's surface and the x-axis points to the centre of the HERA machine. The origin of the coordinate system is the nominal interaction point within the detector.

Given the detector's cylindrical symmetry, it is also convenient to use cylindrical polar coordinates at times and indeed it is usual in the description of the detector components to switch between the two systems. In this system r lies perpendicular to the z coordinate, the polar angle is defined as $\theta = 0^\circ$ in the proton beam direction, $\theta = 180^\circ$ in the electron beam direction. Finally the azimuthal angle ϕ is defined such that it is positive-valued for all positive values of y.

Another useful variable used for describing the detector is pseudorapidity, defined as $\eta = -\ln(\tan\frac{\theta}{2})$. The proton has a substantially larger momentum than the electron with the result that the majority of the products of the ep interactions are produced with large positive values of pseudorapidity in a region also known as the "forward" region. This asymmetry is mirrored in the design of the H1 detector so that the forward region is more highly instrumented than the "backward" region (the region having large negative values of pseudorapidity).

Figure 2.2 shows a schematic view of the H1 detector. The nominal interaction point is surrounded by tracking detectors which are divided into a central, a forward and a backward part. The tracking detectors are surrounded by calorimetry; the Liquid Argon Calorimeter (LAC) which covers the central

and forward regions, a backward calorimeter and the PLUG calorimeter which covers the forward region very close to the beampipe.

The calorimeters are contained within a 1.15 T homogeneous magnetic field provided by a superconducting magnet. The iron return yoke of this magnet is instrumented with streamer tubes which provide calorimetry for those particles escaping the main calorimetry. As these particles are in the tail of the hadronic energy distribution the instrumented iron is also known as the "Tail Catcher". Forward of the Tail Catcher is the Forward Muon Detector (FMD), which is composed of six layers of drift chambers separated by a toroidal magnet.

The Time-of-Flight system, which is used to reject background, consists of several plastic scintillators positioned at various points along the beampipe. The Luminosity System consists principally of the Electron Tagger located at $z = -33.4$ m and the Photon Detector at $z = -103.1$ m. These two detectors are used to measure the Bethe-Heitler process $ep \to ep\gamma$ which has a precisely calculable cross-section in QED.

There are numerous subdetector components. The following detail those parts of the detector which are of particular relevance to this measurement. For a more complete and detailed description of the H1 detector see [54, 55].

2.3 Tracking

Figures 2.3 and 2.4 show the layout of the H1 tracking system longitudinally and radially respectively. Closest to the beampipe is the Central Silicon Tracker (CST), which consists of two concentric cylinders of double sided, double metal silicon sensors allowing track reconstruction down to several hundred μm. This device is surrounded by the Central Track Detector (CTD), which is composed of two multiwire proportional chambers (MWPC), two z drift chambers and two Jet chambers.

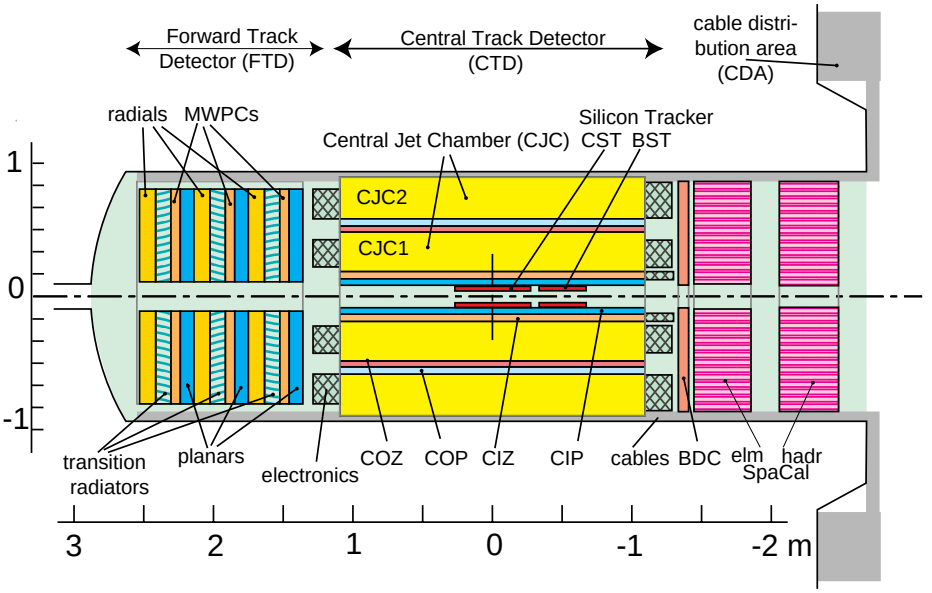

Figure 2.3: The H1 Tracking System viewed longitudinally.

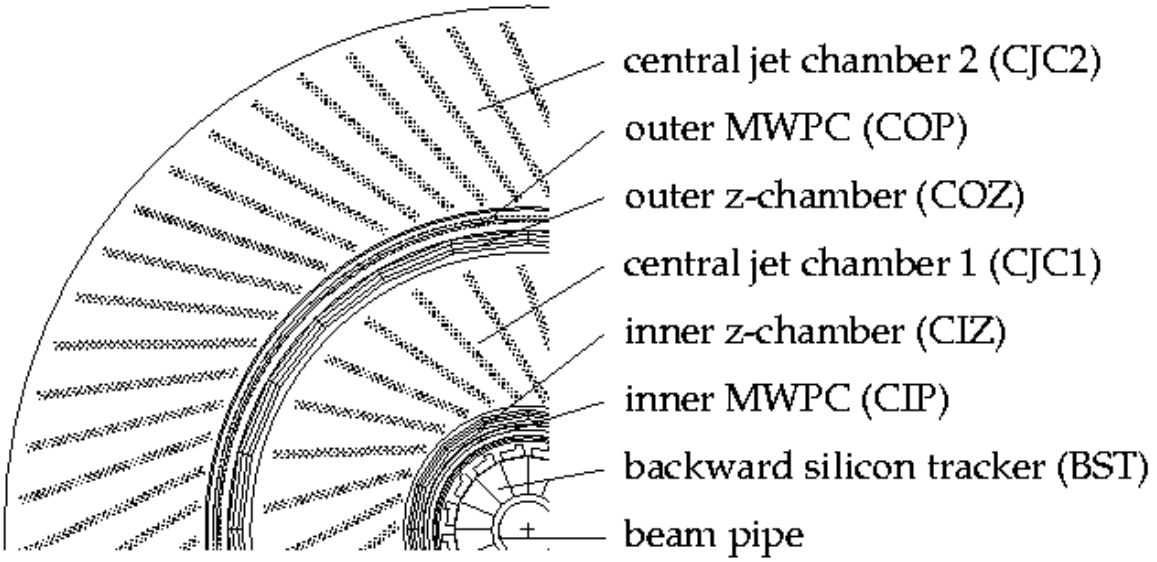

Figure 2.4: The H1 Tracking System viewed radially.

2.3.1 The Central Track Detector

The Central Inner and Outer proportional chambers (CIP and COP) [56] are used primarily for triggering purposes as MWPCs have an intrinsically fast response time. The Central Inner and Outer z-chambers (CIZ and COZ) [57, 58] are drift chambers designed to provide an accurate measurement of the z-position of tracks originating from the interaction vertex, hence their sense wires are strung perpendicular to the beampipe with a drift direction in the z direction. The main purpose of the Central Jet Chambers (CJC1 and CJC2) [59] is to provide an accurate measurement in the $r - \phi$ plane, hence their sense wires run parallel to the beampipe.

The combined angular coverage of the CTD is $25.0° \leq \theta \leq 155.0°$, with a radial coverage of 150 mm $\leq r \leq$ 850 mm. The CJC has a spatial resolution of $\sigma_{r\phi} = 170$ μm and $\sigma_z = 22.0$ mm while the corresponding quantities for the z-Chambers are $\sigma_{r\phi} = 25$ and 58 mm and $\sigma_z = 350$ μm [54].

2.3.2 The Forward Track Detector

The Forward Track Detector (FTD) provides track detection in the forward region with an angular coverage of $7.0° \leq \theta \leq 25.0°$. It consists of three identical supermodules, shown in figure 2.3, each of which contains three "Planar" drift chambers (where the sense-wires have the same orientation as the CJCs) one MWPC, one "Radial" drift chamber (where the sense-wires have the same orientation as the CIZ and COZ) and one transition radiator. The momentum resolution of the FTD is $\sigma_p/p^2 < 0.03$ GeV^{-1} and its angular resolution is $\sigma_{\theta,\phi} < 1$ mrad [60].

Most of the tracks used in this analysis are reconstructed using the CTD and are used to determine the interaction vertex, the track of the scattered electron and the hadronic final state.

2.4 Calorimetry

The calorimetry of the main H1 detector is composed of four main parts, as can be seen in figure 2.2. The Liquid Argon Calorimeter (LAC) is by far the greatest of these components, with an angular coverage of $4^\circ \leq \theta \lesssim 154^\circ$ covering most of the central and forward regions. The SPACAL calorimeter covers the backward region with an angular coverage of $153^\circ < \theta < 177.8^\circ$ being limited by the beampipe. The PLUG calorimeter covers the very forward region closest to the beampipe ($0.6^\circ \lesssim \theta \lesssim 3.5^\circ$) closing the gap between the forward part of LAC and the beampipe. Finally, the encompassing Tail Catcher provides hadronic calorimetry in the region $4^\circ < \theta < 176^\circ$.

In this measurement the LAC plays the principle role in the detection and measurement of the scattered electron at high Q^2, as well as measuring the mass of the hadronic final state M_X. It is also used to determine the leading edge of hadronic activity in the event, and thus the edge of the rapidity gap. The PLUG calorimeter is used with the other forward detectors to define an empty forward region to indicate an elastic proton and rapidity gap. The SPACAL plays only a minor role in this analysis and the Tail Catcher was not used at all[1]; they will not be described in any further detail.

2.4.1 The Liquid Argon Calorimeter

The LAC [61] is divided up into eight "wheels" as shown in figure 2.5(a), each wheel having an innermost electromagnetic part (EMC) followed by a hadronic part (HAC)[2]. Each wheel is segmented in ϕ into eight identical octants, shown in figure 2.5(b). This structure leads to dead regions in the detector, "z-cracks" between adjacent wheels and "Phi-cracks" between each adjacent wheel-octant, which need to be accounted for at the analysis stage.

The LAC is a non-compensating sampling (or sandwich) calorimeter de-

[1] The Tail Catcher has an energy resolution of $\sigma(E)/E \approx 100\%/\sqrt{E\ [\mathrm{GeV}]}$ for pions [54].

[2] As can be seen in the diagram, the backwardmost wheel only has an EMC part and the outermost forward wheel only a HAC part.

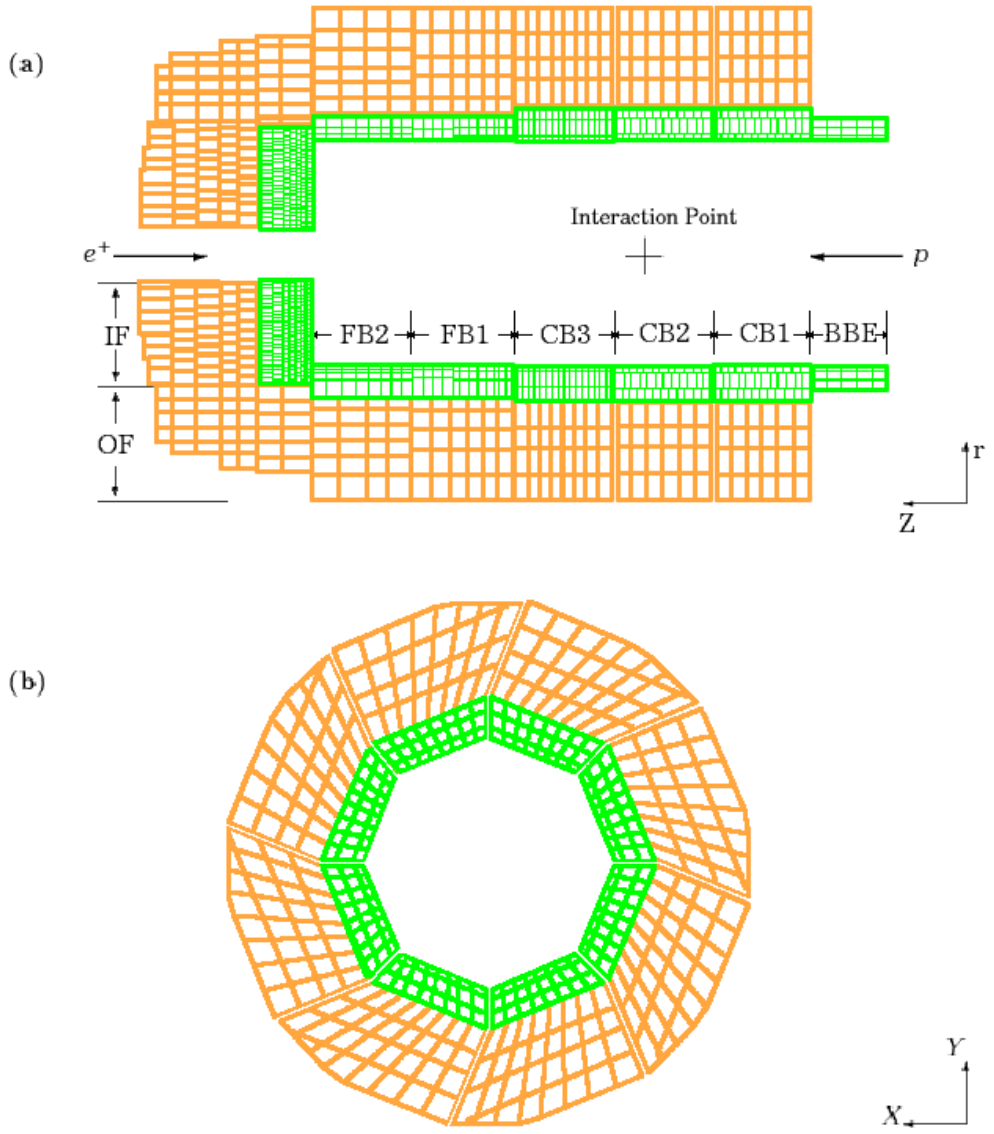

Figure 2.5: The Liquid Argon Calorimeter showing a) The wheel structure and b) The wheel octant structure.

signed to provide clear particle identification of electrons, muons and neutral particles, as well as containing high energy hadronic jets. It has a high granularity for this purpose and contains 44,000 cells, each cell containing plates of absorber (or sampling) medium, the active medium which is liquid Argon, one readout plane and one high voltage plane.

The absorber medium used in the EMC is lead which results in the electromagnetic shower being almost always entirely contained within the EMC. The EMC cells are further segmented longitudinally to have 3 to 4 absorber plates (20 to 30 radiation lengths) within them and the orientation of the cells is optimised for the identification of the scattered electron. Test beams showed that the EMC has an energy resolution of $\sigma_{em}(E)/E = 0.11/\sqrt{E\ [\mathrm{GeV}]} \oplus 0.01$ for electrons [62].

The HAC absorber medium is stainless steel, with a longitudinal segmentation of between 4 and 6 plates in each cell (over 5 to 8 interaction lengths). The LAC is non-compensating and so the charge output for hadrons is $\approx 30\%$ smaller than for electrons, requiring an offline correction for the HAC to the signal measured on the electromagnetic scale. The HAC was found to have an energy resolution of $\sigma_{had}(E)/E = 0.50/\sqrt{E\ [\mathrm{GeV}]} \oplus 0.02$ for charged pions in test beams [62].

2.4.2 The PLUG Calorimeter

The PLUG calorimeter was specifically designed to fill the gap in acceptance between the LAC and the beampipe ($0.6^\circ \lesssim \theta \lesssim 3.5^\circ$) in order to minimise the loss of transverse momentum from the H1 detector in the forward direction. Given the geometrical constraints the PLUG is very compact in design. It is also a sampling calorimeter and uses 9 sheets of copper as the absorber medium interleaved with 8 layers of large area silicon detectors as the active medium. Owing chiefly to the large amount of dead material in front of the detector it has a rather poor resolution of $\sigma(E)/E \approx 150\%/\sqrt{E\ [\mathrm{GeV}]}$ [63].

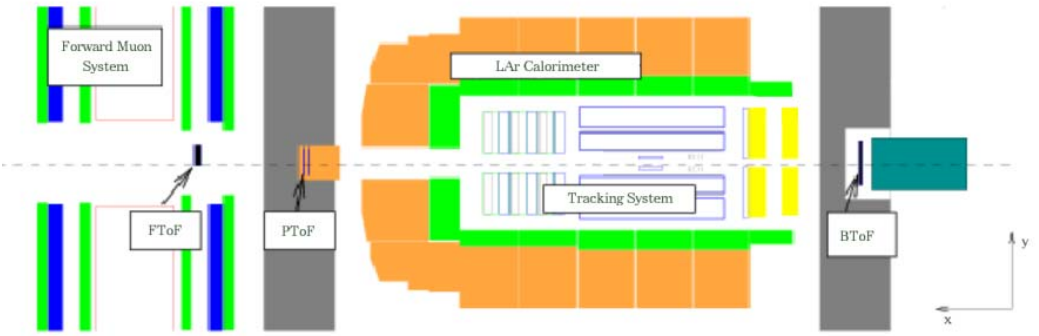

Figure 2.6: The Time of Flight System.

2.5 The Time of Flight System

The Time of Flight (ToF) system is used to reject background from beam-wall and beam-gas interactions. It works on the principle that interactions arising from these background processes occur at a different time to those arising from the ep interactions at the nominal vertex within the main H1 detector. Three plastic scintillators, used for their intrinsically good timing resolution of 1 ns [64], are placed along the beampipe at the positions shown in figure 2.6. Two "Veto Walls", large layers of scintillator, situated at $z = -650$ cm and $z = -810$ cm supplement the system. Any signals in these scintillators occuring at a time consistent with background processes can be used to reject events.

2.6 The Luminosity System

The luminosity measurement at H1 relies on measuring the rate of the Bethe-Heitler process $ep \to ep\gamma$ [65] which has an accurately calculable cross-section within QED. The measurement is made using the Electon Tagger (ET) at $z = -33.4$ m and the Photon Detector (PD) at $z = -103.1$ m shown in figure 2.7. The rate measurement uses the PD alone, using coincident hits in the ET

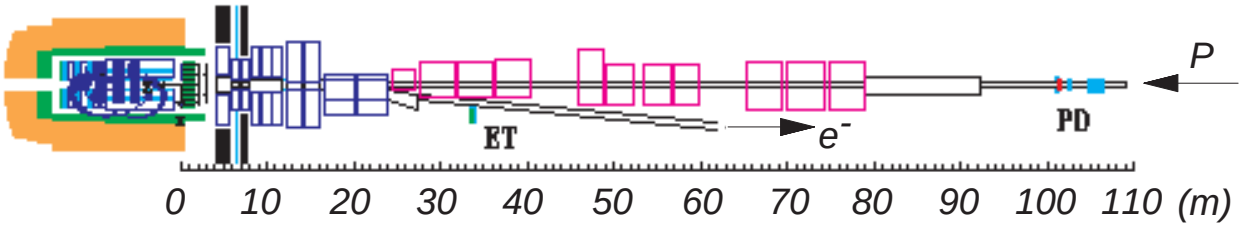

Figure 2.7: The Luminosity System.

to verify the events. This online measurement is used by the HERA operation crew to optimise luminosity delivery at the start of each fill. Offline the measured rate is corrected for background events using the methods discussed previously.

2.7 The Forward and Very Forward Components of the H1 Detector

In elastic diffractive DIS processes, described in section 1.4, the forward region of the H1 detector is empty. The definition of an empty forward region relies on the use of some of the forward and very forward detectors at H1, which are described in the following.

2.7.1 The Forward Muon Detector

The Forward Muon Detector [66] consists of two sets of three double-layers of drift chambers which are separated by a toroidal magnet, as can be seen in figure 2.8. Four of the double-layers are constructed with their wires strung tangentially to the beampipe to enable a measurement of θ, a "Theta-layer", two of the double-layers have their wires strung radially to enable a ϕ measurement, a "Phi-layer" and the overall angular coverage is $3° < \theta < 18.0°$. The presence

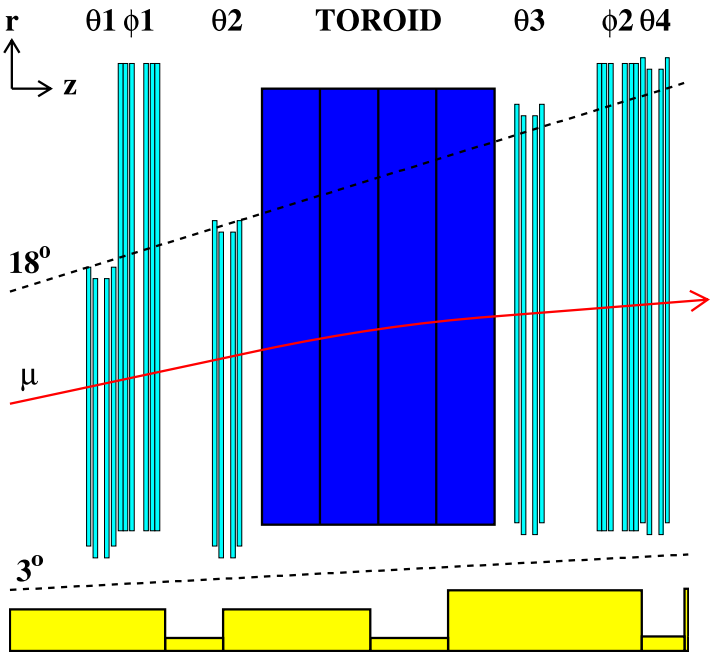

Figure 2.8: The Forward Muon Detector.

of the toroid magnet allows for a momentum measurement to be made in the range $5 < p < 100$ GeV. It also means that the post-toroid layers are inherently noisier than the pre-toroid layers, due to the amount of dead-material and synchrotron radiation, and for the purposes of this analysis only the pre-toroid layers are considered.

2.7.2 The Proton Remnant Tagger

The Proton Remnant Tagger (PRT), at $z = 24$ m, consists of seven individual detectors, each constructed from two separate layers of plastic scintillator separated by 2 mm of lead, which surround the beampipe in the configuration shown in figure 2.9. A coincidental hit in both layers of a detector, at a time consistent with an *ep* interaction in the main detector, results in a signal being registered for data acquisition.

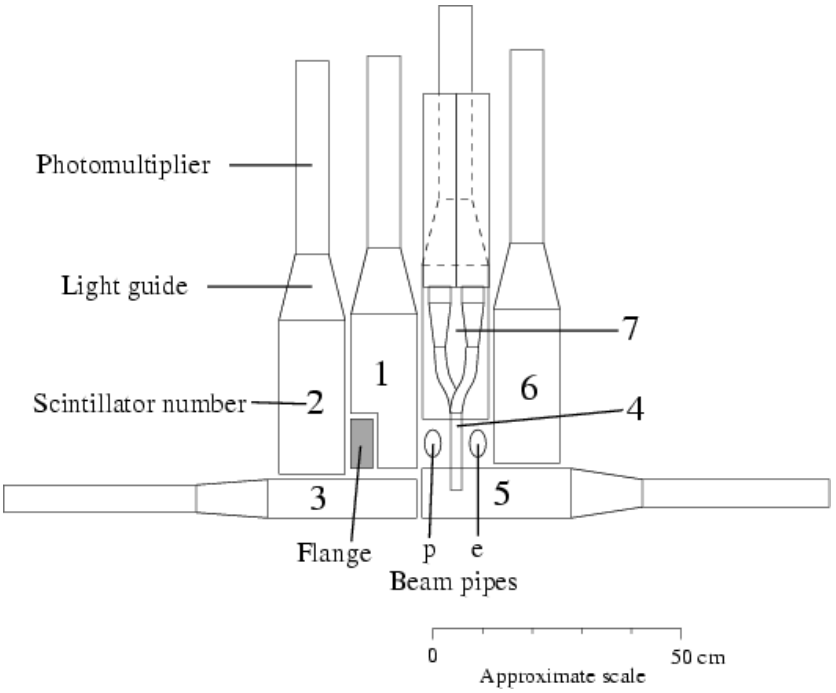

Figure 2.9: The Proton Remnant Tagger.

2.8 Data Acquisition and Triggering

The time between consecutive *ep* interactions is determined by the distance between beam bunches and is 96 ns. However, the time taken to read all of the information from the various detector components is an order of magnitude greater than this which would result in the loss of most *ep* events. When the experiment is not recording *ep* events it is said to be running in deadtime. To reduce this problem the H1 detector uses a multi-stage triggering system to reject background events and record as many *ep* interactions as possible, a schematic of which is shown in figure 2.10.

At the first trigger level (L1) each detector component provides information, called "trigger elements", to the central trigger logic (CTL) which makes logical combinations of this information to form 128 "subtriggers". Not all detectors can provide this information within 96 ns, the limiting component being the LAC which requires 2.1 μs. The full detector information is therefore sent into pipelines where it is stored until all detectors have provided their

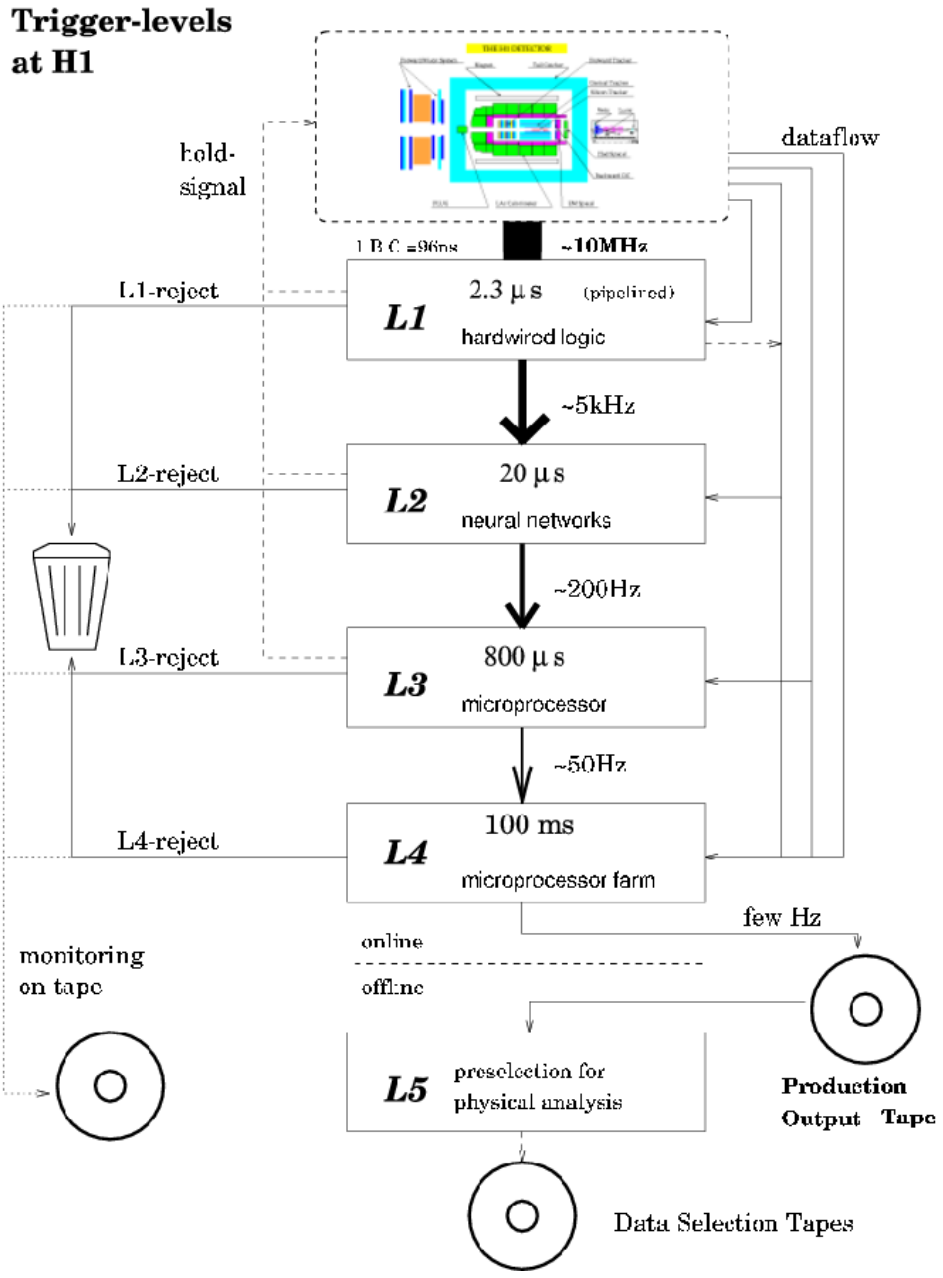

Figure 2.10: The H1 Trigger System.

trigger elements. If the CTL finds that the event fulfills any one of the 128 subtrigger conditions then the corresponding event is read from the pipeline and passed to the next trigger level. Thus the L1 trigger level is deadtime free as any rejected events are simply overwritten in the pipeline.

The next level of triggering, L2, takes advantage of the increased amount of time available (20 μs) to make a decision to run more complicated algorithms on the available information. L2 can therefore base a decision on neural networks as well as topological conditions. Again if the event passes any of the L2 criteria it is passed onto the next level in the chain. In theory this would be level 3, which has 2 ms time to make a decision, but to date this has not been implemented.

The next level is therefore L4 where the full event information is available and a partial event reconstruction is performed. L4 runs asynchronously to the HERA machine on a processor farm of 32 PCs. Each event that was accepted by an L1 trigger is verified with higher precision and the events are written to tape at a rate of $\approx$ 10 - 20 Hz.

Finally, although the events have been written to tape a further level of processing, L5, performs a complete reconstruction of the event and determines to which physics event class it belongs. If none is found then the event is rejected, otherwise the event is written to a Data Summary Tape (DST) which then provides the basis for physics analysis.

Chapter 3

Selection of Diffractive DIS Events

In this chapter the method used to select the high Q^2 diffractive DIS event sample is presented. Section 3.1 details the inclusive high Q^2 NC DIS selection, while in section 3.2 the method of selecting the diffractive subsample of these events is given. Distributions of event sample quantities are presented and compared with simulations in sections 3.1.6 and 3.2.6 for the inclusive and diffractive samples, respectively.

3.1 Selection of High Q^2 NC DIS Events

The high Q^2 NC DIS event sample is defined as being the sample of events with a good electron candidate in the LAC. The efficiency of finding the electron candidate and sources of background to these events must be well understood.

3.1.1 The High Q^2 Electron Finder

The principle criteria for the identification of an electron at high Q^2 are based solely on the expected calorimeter topology. This is the observation of a compact and isolated energy deposit in the electromagnetic part of the LAC with little or no activity in the hadronic part of the LAC behind this deposit. The

electron finder QESCAT [67] used in this analysis employs estimator variables which quantify the shower-shape properties of an electron candidate and then performs a selection based on these variables.

The first set of estimators are used to define a compact cluster. The total energy of the electron candidate cluster, ETOT, must be greater than 5 GeV and the number of cells assigned to the candidate, NCEL, must be greater than 3. The fraction of the total energy which is contained in the first 2 layers of the EMC (increased to 3 layers in the forward region), EAEM, must be large and the fraction of EAEM which is in the hot core of the cluster, EAHN, must also be large. The transverse dispersion of the cluster, EATR, defined in equation 3.1, must be small.

$$EATR = \sqrt{\sum_i \frac{E_i R_i^2}{V_i} - \left(\sum_i \frac{E_i R_i}{V_i} \right)^2} \tag{3.1}$$

In this equation both sums are over each cell of the electron candidate and E is the energy of the cell, R the radius of the cell and V the volume.

An isolation cone, defined in $\eta - \phi$ space, is then used to sample the calorimeter deposits surrounding the electron candidate cluster. The fraction of energy in the isolation cone should be small and conversely the ratio of the total energy of the electron candidate to the isolation cone energy, EAIF(=ETOT / isolation cone energy), should be large. The hadronic energy in the isolation cone, EAHD, should also be small.

Details of the selection criteria are shown in table 3.1. Note that in the forward region of the LAC the selection cuts are loosened due to the limited resolution. In the case that QESCAT identifies more than one electron candidate the scattered electron is taken to be the candidate with the highest transverse momentum.

The efficiency of QESCAT for finding electrons is found to be $> 99\%$ [68], except in those regions of the detector where the electron can directly enter the hadronic section of the calorimeter without causing a shower in the

Estimator Variable	Description	Cut value
ETOT	Total cluster energy	> 5 GeV
EAEM	Energy fraction in first 2 (3 in IF) layers of EMC	$> 0.94 + 0.05\cos(2\theta)$
EAHN	Energy fraction in Hot Core (Hot Core Energy / EAEM)	$> 0.8(0.4)$ in bwd (fwd) region
EATR	Transverse dispersion	$< 7.5(3)$ in bwd (fwd) region
NCEL	Number of cells assigned to electron candidate	> 3
EAIF	Energy fraction in isolation cone (ETOT / Isolated Energy)	EAIF > 0.98
EAHD	Hadronic energy in Isolation Cone	EAHD ≤ 300 MeV and EAIF > 0.95

Table 3.1: *Table of the cluster estimators, the description of the parameters and the cut values which are used by QESCAT.*

electromagnetic section. These inefficient regions are removed from the event sample.

The probability of misidentifying a hadronic particle as an electron, found using simulated NC events, is found to be $< 0.2\%$ [68]. The additional requirement of demanding a track that points to the electron energy cluster from the primary vertex[1], a "Track-link" requirement, efficiently reduces this background. The selection is performed by making a cut on the distance of closest approach (dca) of an extrapolated track to the electron candidate. A loose requirement of dca < 12 cm is chosen to keep the selection efficiency high [68].

3.1.2 The Detector Operation and Trigger Selections

In order to ensure that the detector efficiency is high and stable a run selection is applied which selects only those runs where those parts of the H1 detector which are essential to this analysis are operational. In addition to the LAC the SPACAL calorimeter and CTD are required for the final state measurement, as well as helping to reduce backgrounds, as discussed in 3.1.4. The luminosity system is essential for the accurate determination of the luminosity measurement and the ToF system is again vital for reducing backgrounds. Observations of periods of coherent noise in the LAC which lead to a loss of efficiency in electron identification require a further run selection to remove these periods.

The sub-triggers used to keep high Q^2 NC events, together with a brief description, are presented in table 3.2. An event is kept in the analysis if any of these sub-triggers fired and the event also subsequently passed the L4 verification trigger level.

The energy thresholds of the triggers are increased up to a factor of 5 in the very forward regions of the LAC, again due to the poorer resolution. Regions of the LAC for which the ST67 trigger is not 100% efficient are removed from

[1] see section 3.1.3

Subtrigger	Description
ST67	Energy in EMC $>$ 3.8 GeV
ST71	Central Vertex && $\geq$ 3 Central Tracks with $p_T > 420$ MeV && A Track Combined with a Cluster in the LAC
ST75	Energy in EMC $>$ 2.8 GeV && $\geq$ 1 Central Track with $p_T > 420$ MeV
ST77	Missing Transverse Energy in the LAC

Table 3.2: *A description of the high Q^2 NC DIS Triggers used in this analysis.*

the sample [13].

3.1.3 Reconstruction of the Inclusive Final State

The reconstruction of a primary vertex is essential for measuring the final state accurately and also for reducing background from non *ep* events and out-of-time events. Vertices found by the CTD (Central Vertices) are supplemented at low y or high Q^2 by vertices found by the FTD (Forward Vertices) in order to keep events where the hadronic system or the electron track respectively are at the edge of the acceptance of the CTD. All events are required to have a vertex reconstructed to within 35 cm of the nominal *ep* interaction point. Simulations of the z position of the vertex, z_{vtx}, show both a shift in the mean position and that the simulation underestimates the width of the z_{vtx} distribution. The simulated z_{vtx} distribution is reweighted to the data distribution resulting in a good description, as can be seen in figures 3.2 and 3.9.

The measurement of the hadronic final state relies on the use of both the full calorimeter and tracking information. This overconstrains the final state and a variety of methods can be used to reconstruct the kinematic variables given in equation 1.1. It is possible to measure the kinematics either from

the electron information alone, the hadronic information alone, the angular information of the electron and hadronic system (the Double-Angle or DA method), or a combination of the information.

The Electron Method

The Electron method uses only information from the scattered electron to determine the kinematics of the *ep* interaction. The electron beam energy, E_e, is required together with the energy and angle of the scattered electron, $E_e^{'}$ and θ_e. The Electron method is defined as:

$$Q_e^2 = 4E_e E_e^{'} \cos\frac{\theta_e}{2}^2, \qquad y_e = 1 - \frac{E_e^{'}}{E_e}\frac{(1-\cos\theta_e)}{2}, \qquad x_e = \frac{Q_e^2}{sy_e} \tag{3.2}$$

The Double-Angle Method

The Double-Angle (DA or da) method combines the angular information of both the scattered electron and the hadronic final state to reconstruct the kinematics of the *ep* interaction. It is defined as:

$$y_{da} = \frac{\sin\theta_e(1-\cos\gamma_h)}{\Upsilon}, \quad Q_{da}^2 = \frac{4E_e^2\sin\gamma_h(1+\cos\theta_e)}{\Upsilon}, \quad x_{da} = \frac{Q_{da}^2}{sy_{da}} \tag{3.3}$$

where γ_h is the polar angle of the hadronic system and

$$\Upsilon = \sin\gamma_h + \sin\theta_e - \sin(\theta_e + \gamma_h).$$

The Σ Method

The Σ method combines information from both the scattered electron and the hadronic system. It is defined as:

$$y_\Sigma = \frac{\Sigma}{E_{mpz}}, \qquad Q_\Sigma^2 = \frac{(E_e^{'}\sin\theta_e)^2}{1-y_\Sigma}, \qquad x_\Sigma = \frac{Q_\Sigma^2}{sy_\Sigma} \tag{3.4}$$

where Σ and E_{mpz} are defined as:

$$\Sigma = \sum_{i\neq n_e} E_i - p_{z,i}, \qquad E_{mpz} = \sum_i E_i - p_{z,i}. \tag{3.5}$$

The summation in the expression for Σ is over all final state objects (FSO) in the detector except for the scattered electron, n_e, whereas the summation in the expression for E_{mpz} is over all FSOs in the detector. A final state object here refers to an optimised combination of tracking and calorimeter information which avoids double-counting [69].

The eΣ Method

Two reconstruction methods were considered for this analysis. The first method considered is called the eΣ method as it combines the excellent precision of the electron-only method in measuring Q^2 with the best reconstruction of x at the inclusive level which uses the Σ method given in equation 3.4. The eΣ method is:

$$Q^2_{e\Sigma} = Q^2_e, \qquad x_{e\Sigma} = x_\Sigma, \qquad y_{e\Sigma} = \frac{Q^2}{sx}. \tag{3.6}$$

The y Weighted Average Method

The second method considered for this analysis is called the "y weighted average method" as it combines the excellent precision of the electron method at high y with the excellent precision of the DA method at low y. This method has the best resolution for inclusive diffraction and is the default method for this analysis. The reason for its superior resolution is that the hadronic final state is completely contained in the main calorimeter in the case of diffraction, as there are no forward energy losses, and so the resolution in the hadronic angle and therefore the DA method is excellent. The y weighted average method is:

$$y = y_e^2 + y_{da}(1 - y_{da}), \qquad Q^2 = \frac{4E_e^2(1-y)}{\tan^2\frac{\theta_e}{2}}, \qquad x = \frac{Q^2}{sy} \tag{3.7}$$

3.1.4 Background Rejection

The main sources of non ep background in the NC sample are cosmic ray and beam-halo events which produce muons. These muons can be misidentified as the scattered electron. The requirement of a primary vertex and a track-link

efficiently reduce this background to small levels [68]. The contamination is also reduced by requiring the CJC timing information to be consistent with an ep event. This contamination is finally reduced to negligible levels [68] by the application of dedicated background finders [70].

Sources of ep-induced background to the high Q^2 NC sample are photoproduction, low Q^2 DIS, QED Compton scattering and $\gamma\gamma$ events. Photoproduction and low Q^2 DIS, in which the scattered electron escapes the main detector and part of the final state is misidentified as the electron, are efficiently reduced by the track-link requirement. These events are also only found at high values of y and low values of $E_e^{'}$ and so additional cuts on y and an effective cut on the scattered electron energy reduce this source of contamination to small levels [13, 68]. In addition a cut on E_{mpz} (the total $E - p_z$) of the event reduces the photoproduction background. In a DIS event the kinematics determine that $E_{mpz} = 2E_e = 55$ GeV, whereas a photoproduction event will have a much lower value of E_{mpz} by virtue of the missing electron. The event selection requires that $E_{mpz} > 35$ GeV for all events in this measurement, which also reduces the Initial State Radiation corrections (see section 4.3.4).

The remaining photoproduction background is removed by studying scattered electron candidates that have the opposite sign charge to the electron beam, i.e. the track assigned to the electron candidate is measured to have a negative charge. Assuming that in a photoproduction event the track wrongly assigned to part of the hadronic final state has an equal probability of being positive or negative, then the total number of photoproduction events in the sample is twice the number of opposite-sign charge events and this background can be statistically subtracted. For electron energies less than 18 GeV this background is efficiently removed by applying this technique, above this electron energy the technique becomes less efficient due to mismeasurement of the charge of high p_T tracks. Using Pythia to simulate photoproduction, the photoproduction background is seen to fall to negligible levels for $E_e^{'} > 18$ GeV. The strategy employed in this analysis is to apply the tech-

nique only for $E_e^{'} < 18$ GeV. The systematic uncertainty arising from this procedure is cautiously estimated to be given by the largest subtracted value in any of the affected bins.

QED Compton and $\gamma\gamma$ background events are rejected via their distinctive final state; two electromagnetic clusters of energy with no hadronic deposits and only one or two tracks.

3.1.5 The Final Inclusive DIS Selection

The primary requirement of the inclusive DIS selection is that there is a good electron candidate in the LAC, as defined in section 3.1.1. Further topological requirements demand a good ep interaction vertex and a track linking that vertex with the electron candidate in the LAC. Regions of the detector where the efficiency for electron identification is low are removed from the event sample. In addition one of the high Q^2 NC triggers must have fired and the event subsequently passed the L4 verification level.

Kinematic cuts on the y and E_{mpz} of the event and an effective cut on the electron energy reduce the photoproduction and low Q^2 DIS backgrounds to negligible levels. The remaining backgrounds from elastic QED Compton, elastic $\gamma\gamma$ events and beam-induced backgrounds are removed via the application of the dedicated background-finders discussed in section 3.1.4.

The final selection cuts used to select high Q^2 NC events are summarised in table 3.3.

3.1.6 Inclusive DIS Control Distributions

In this section control distributions are used to demonstrate the level at which the high Q^2 NC DIS event sample is understood. Sets of distributions are shown which compare the data to the sample of events made with the DJANGO MC simulation. The electron calibration described in [68] is also briefly studied.

Selection Description	Values
A good electron candidate in the LAC	See Section 3.1.1
High Q^2 NC triggers	$ST67 \parallel ST71 \parallel ST75 \parallel ST77$
Track pointing at the electron cluster	$dca \leq 12.0$ cm (not required for $\theta_e < 30^\circ$)
Electron not in a crack in the LAC	z-crack at $15.0 < z^e_{impact} < 25.0$ cm 2° either side of Octant edge
A Central or Forward vertex	Forward vertices only accepted if $y_e < 0.1 \parallel Q^2_e > 1000.0$ GeV^2
z position of vertex	$-32.2 < z_{vtx} < 37.8$ cm
CJC Timing consistent with ep event	≤ 25 ns of nominal interaction time
y cut	$y_e < 0.9$
E_{mpz} cut	$E_{mpz} > 35.0$ GeV
Electron Energy cut	$y_e < 0.63 \parallel Q^2_e > 890.0$ GeV^2
Not a QED Compton / LPair event	See Section 3.1.4
Event not found by Background finders	See Section 3.1.4

Table 3.3: *A list of the cuts made to select the inclusive high Q^2 NC DIS event sample.*

General Inclusive DIS Control Distributions

Figure 3.1 shows the energy, θ and ϕ distributions of the electron in the inclusive high Q^2 NC DIS event sample for both data and simulation. In general the agreement between data and the DJANGO simulation is very good. The electron energy distribution, which peaks as expected at the electron beam energy, is well described by DJANGO although the predicted resolution in the simulation is better. This can be attributed to detector resolution effects not modelled by the detector simulation; as the final event sample does not show this effect no attempt was made in this analysis to correct the simulation. The θ distribution shows the expected peak at the highest values of θ, corresponding to the edge of the LAC, and the simulation describes this well. The ϕ distribution shows some detailed structure, corresponding to regions of the detector that are removed from the event sample (see section 3.1.1). This structure is also modelled by the simulation.

The z position of the ep interaction vertex, z_{vtx}, and the z position at which the electron enters the LAC, z^e_{impact}, are shown in figure 3.2. The z_{vtx} distribution, after reweighting (see section 3.1.3), is well described by the simulation. The z^e_{impact} distribution is also well described by the simulation, including two notable features; the z-crack at $15.0 < z^e_{impact} < 25.0$ cm and the edge of the BBE at $z^e_{impact} = 152.5$ cm, both of which can be clearly seen.

Figure 3.3 shows the distributions of y, E_{mpz} and Q^2 for the inclusive high Q^2 NC DIS event sample. The y distribution is peaked at low values of y and the effect of the cut $y_e < 0.63 \parallel Q^2_e > 890.0$ GeV^2 can be clearly seen; both features are described by the simulation. The E_{mpz} distribution shows the cut of $E_{mpz} > 35$ GeV and peaks at $2E_e = 55$ GeV, as expected; the distribution is well described by the simulation. The Q^2 distribution peaks at low Q^2 and then decreases rapidly with increasing Q^2, as expected from equation 1.4.

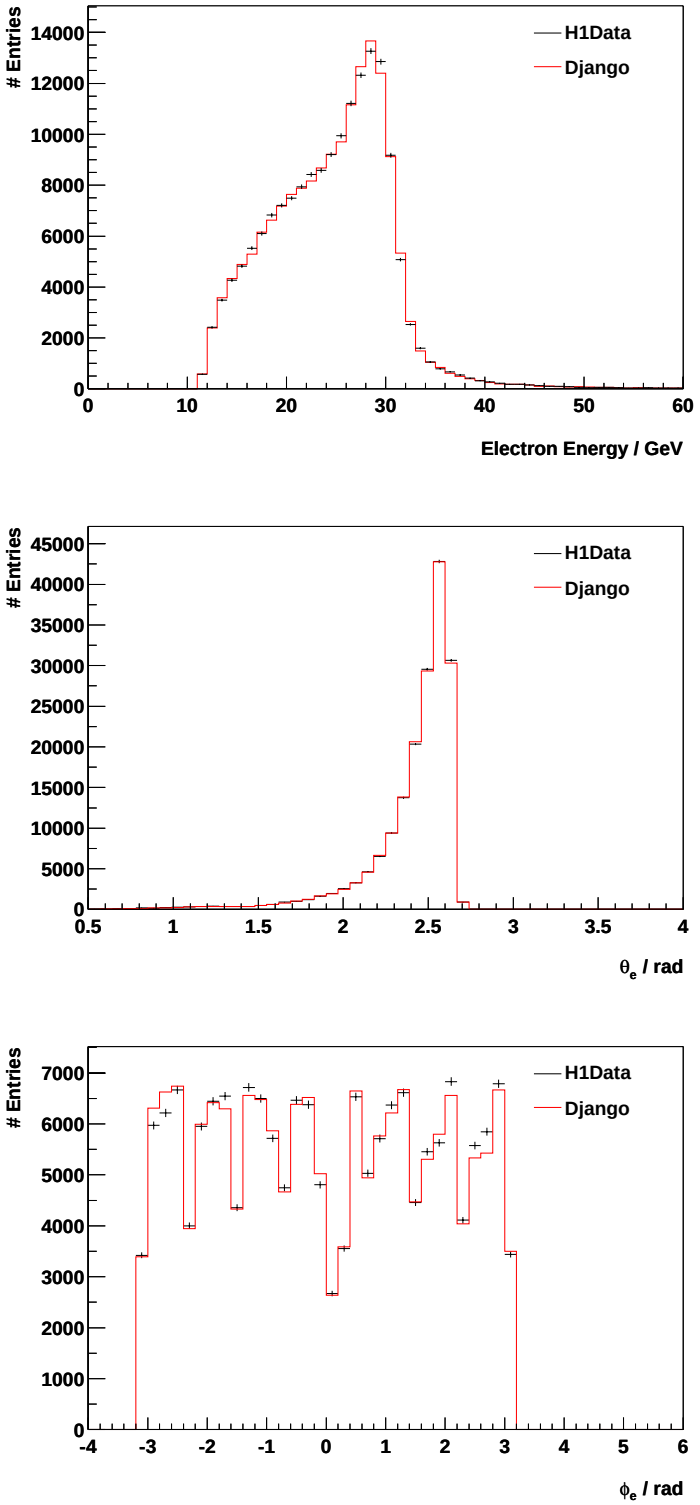

Figure 3.1: *Distributions of the energy (top), the polar angle (middle) and the azimuthal angle of the scattered electron. The data are shown as points, the predictions of the DJANGO simulation are shown as solid red histograms.*

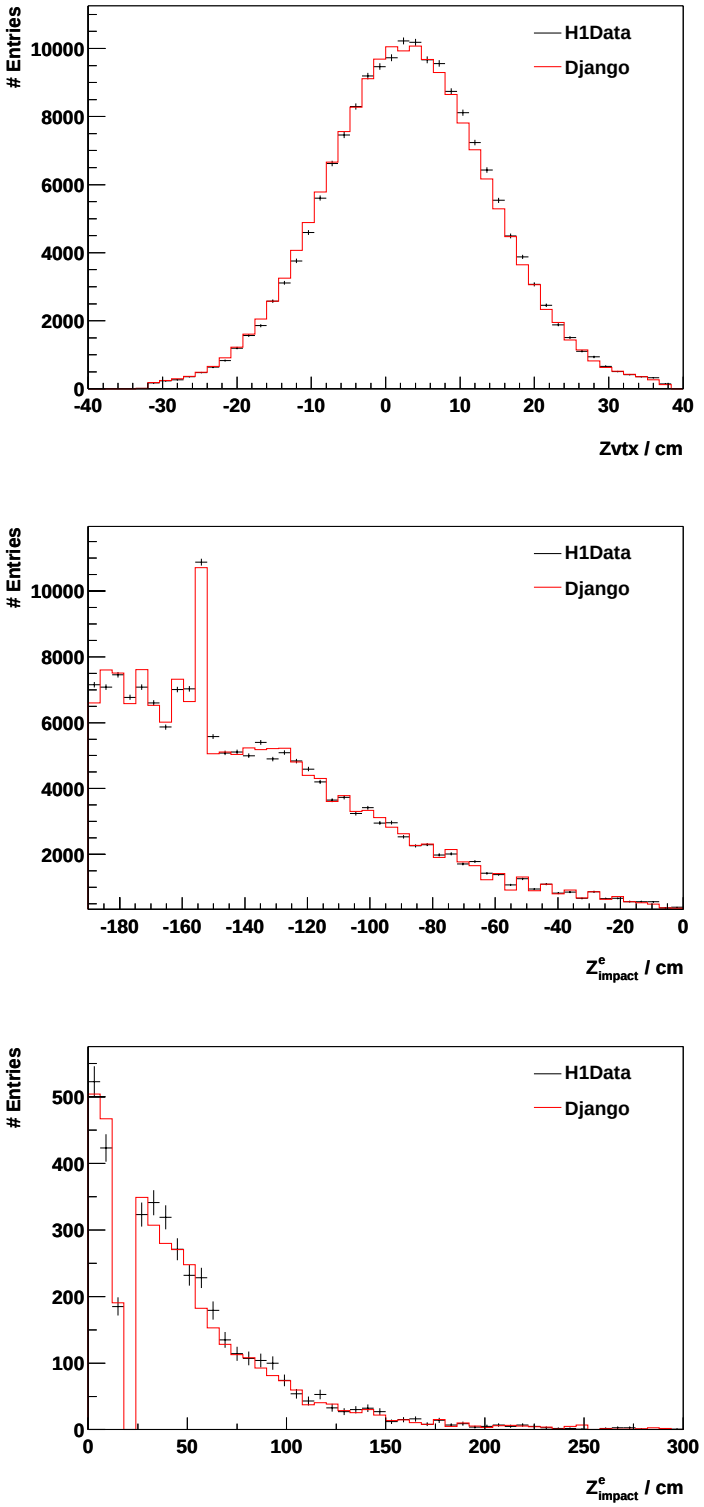

Figure 3.2: *Distributions of the z_{vtx} of the event (top) and z^e_{impact} shown in two ranges, $-190 < z^e_{impact} < 0$ cm (middle) and $0 < z^e_{impact} < 300$ cm (bottom). The data are shown as points, the predictions of the DJANGO simulation are shown as solid red histograms.*

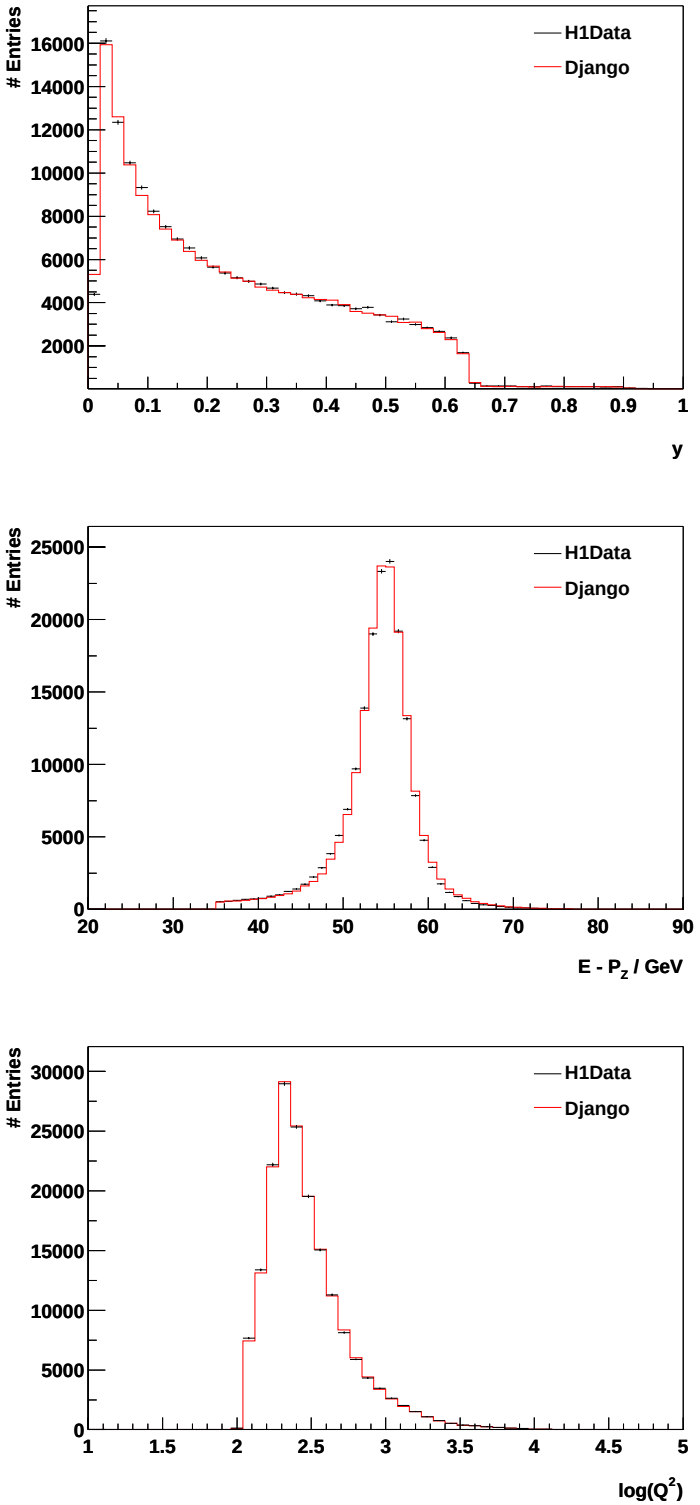

Figure 3.3: *Distributions of the reconstructed y of the event (top), the E_{mpz} (middle) and $\log Q^2$ (bottom). The data are shown as points, the predictions of the DJANGO simulation are shown as solid red histograms.*

The Electron Calibration

The procedure used to calibrate the electron energy measured in the LAC is described in detail in [68]. The energy of the electron as measured using the DA kinematic reconstruction method, E_{da}, is used as the calibration scale. Figure 3.4 shows the ratio of the calibrated energy to E_{da}, in four bins of z^e_{impact} and as a function of ϕ, for data and the DJANGO simulation. The agreement between data and simulation is very good and an uncertainty of 1%, increasing to 3% in the forward region, on the electromagnetic energy scale is obtained.

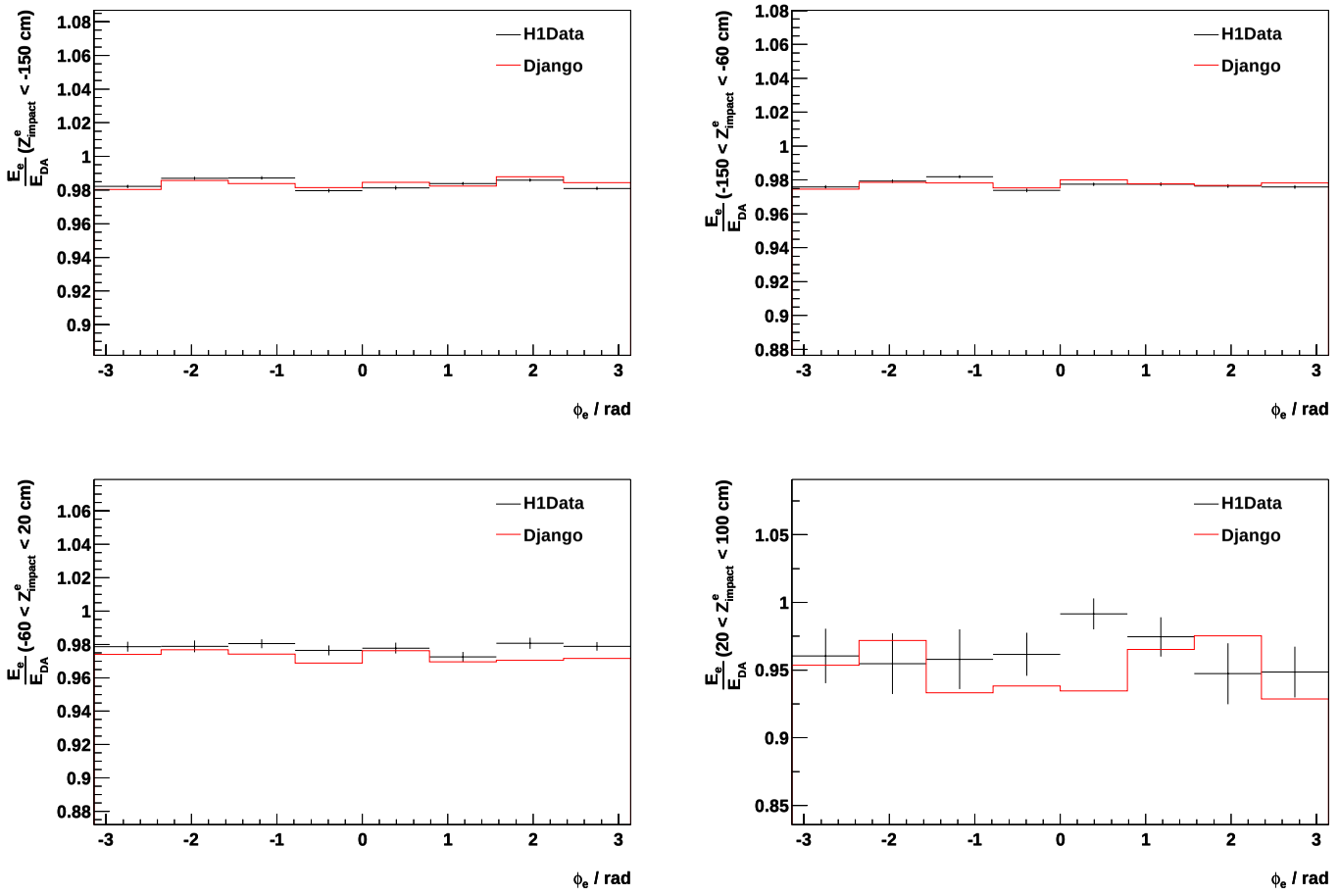

Figure 3.4: *The ratio of E_{da} to the calibrated electron energy E'_e versus ϕ of the electron in four bins of z^e_{impact}; $z^e_{impact} < -150$ cm (top left), $-150 < z^e_{impact} < -60$ cm (top right), $-60 < z^e_{impact} < 20$ cm (bottom left), $20 < z^e_{impact} < 100$ cm (bottom right). The data are shown as points, the predictions of the DJANGO simulation are shown as solid red histograms.*

3.2 Selection of Diffractive DIS events

The diffractive subsample of the high Q^2 inclusive NC DIS event sample is defined as the sample of events where there are two distinct final-state systems, X and Y, separated by a large gap in rapidity, signalling a colour-singlet exchange. The selection demands that a quasi-elastic proton (Y), which escapes undetected down the beampipe, is well separated from the photon-dissociation system X, which is contained in the main detector.

It is experimentally possible to measure the leading proton using the Forward Proton Spectrometer (FPS) and thus measure M_Y and t. This method is unfortunately very limited in statistics by the geometric acceptance of the FPS. The selection method presented here is known as the rapidity gap selection technique and relies on the indirect detection of the leading proton by demanding no activity in the forward detectors of H1. The cross-section is defined for the kinematic range:

$$M_Y < 1.6 \text{ GeV}, \qquad |t| < 1.0 \text{ GeV}^2 \tag{3.8}$$

The variable η_{max} quantifies, at a given noise threshold, the rapidity of the FSO which is furthest forward in the LAC. A pure sample of diffractive events can be selected by demanding $\eta_{max} < 2.0$, with standard DIS events predominantly being at larger values. However, the statistics and phase-space of the sample can be vastly improved by lowering this cut; the forward detectors of H1 must then be used to guarantee the rapidity gap between the X and Y systems. The cut on η_{max} used in this analysis is

$$\eta_{max} \leq 3.3. \tag{3.9}$$

The principle component used in the forward detector selection is the FMD. The FMD was originally designed to measure high energy muons but it is also sensitive to secondary particles resulting from proton dissociation decay products interacting with the beampipe and so provides an effective veto for proton dissociation events. The Proton Remnant Tagger was designed to veto

events with activity in the forward direction. The PLUG calorimeter covers the gap in rapidity between the LAC and the FMD and requiring no deposit in this calorimeter above noise levels guarantees the large rapidity gap.

The run selection for these detectors only demands that the FMD and PLUG be operational. Periods when the PRT were not operational are treated as an inefficiency incorporated into the detector simulation. Run periods when the PRT or PLUG experienced high levels of noise are excluded from the event sample.

The following details the procedure used for selecting the diffractive event sample and estimating the uncertainty in the final measurements which result from the current lack of understanding of the underlying process.

3.2.1 The Forward Muon Detector Selection

Only the three pre-toroid layers of the FMD are used for this analysis as they are shielded from synchrotron radiation by the toroidal magnet unlike the noisier post-toroid layers. The total number of hit-pairs in each of these layers is used to perform the selection, thus the FMD is used very much as a tagging detector. Demanding activity at the level of one total hit-pair in the first two layers of the FMD, and two total hit-pairs in the first three layers of the FMD reduces the level of background in these detectors to $\sim 2.7\%$. This can be corrected for using "Random Trigger" events, events that are taken without a physics trigger, which allows the level of noise as a function of time to be studied. Simulated noise is then added in event by event to the simulation based on these studies.

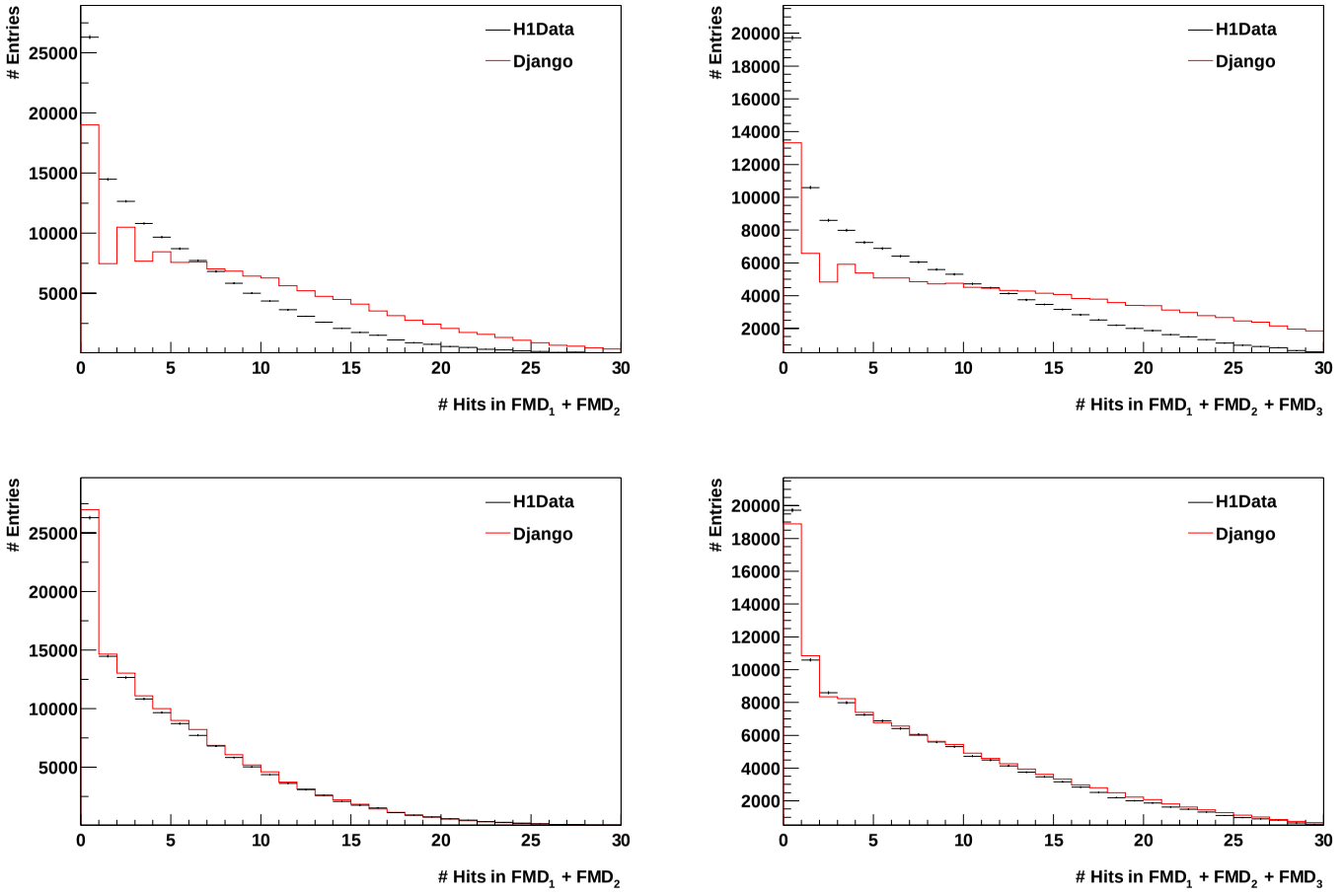

Figure 3.5: *The summed number of hit pairs in FMD layers 1 and 2 [and 3] before (top left [right]) and after (bottom left [right]) reweighting. The data are shown as points, the predictions of the DJANGO simulation are shown as solid red histograms.*

The activity after the addition of random noise events in the FMD detector for inclusive DIS events with forward activity ($\eta_{max} > 3.3$), i.e. non-diffractive events, is shown in figure 3.5. It can be seen that the simulation's description of the data is quite poor. Studies revealed that the only remaining source for this discrepancy must be the DJANGO event generator[1]. The simulated distribution for the sum of the first two layers of the FMD was therefore reweighted to the data distribution for the DJANGO simulation only in order to obtain a better description of non-diffractive events and thus reject them from the event sample. Although the layers are not independent and therefore a perfect description was not achievable, the resulting description, seen in figure 3.5, is sufficient for this analysis.

The uncertainty of the efficiency of the FMD for rejecting non-diffractive events is estimated as 10%, which is the change in the efficiency of the FMD after reweighting; this is included as a systematic uncertainty on the final result. The final results were found to be independent of this reweight.

The diffractive event selection requires that there be less than two hit-pairs in the sum of the first two layers and less than three hit-pairs in the sum of all three pre-toroid layers:

$$\sum_{i=0}^{1} N_{FMD,i} \leq 1 \tag{3.10}$$

$$\sum_{i=0}^{2} N_{FMD,i} \leq 2. \tag{3.11}$$

3.2.2 The Proton Remnant Tagger Selection

Shown in figure 3.6 is the activity in the PRT for inclusive DIS events with forward activity. It can be seen that the efficiency of the PRT for detecting

[1]Possibile sources that were ruled out are a.) the model of forward energy flow used, b.) a year-dependence of the data not included in the detector simulation [72], c.) an incorrect year-dependent change in the detector simulation [73], d.) a Q^2-dependence of the data [74] and e.) trivial error [71]. None of these five possibilities could produce the observed discrepancy.

events with forward activity is consistently overestimated in the DJANGO simulation. This can be attributed to the poor simulation of the very forward region in the standard detector simulation and is corrected scintillator by scintillator by applying a correction factor which degrades the efficiency in the simulation to match the data. After these corrections are applied the DJANGO simulation still shows more activity than the data, attributed to the simulation predicting more correlations between layers than the data, and so a further downgrading of the overall efficiency of the simulation is applied. The final results are shown in figure 3.6. Note that the final two layers of the PRT are excluded from the analysis as they are between four and five times noisier than the other layers which have a negligible level of noise.

The diffractive event selection requires no activity in the PRT:

$$\sum_{i=0}^{4} N_{PRT,i} = 0. \tag{3.12}$$

3.2.3 The PLUG Calorimeter Selection

The DJANGO simulation also lacks any simulation of noise in the PLUG calorimeter; this was again corrected using randomly-triggered events to add noise into the simulation event by event. The energy scale of the PLUG calorimeter is only known to $\pm 30\%$ which is included as a systematic uncertainty on the final results. The energy distribution for the PLUG calorimeter for events with forward activity is shown in figure 3.7; again the description is quite poor. However, the efficiency for the PLUG calorimeter rejecting a non-diffractive event ($\eta_{max} > 3.3$) with an energy greater than 3.5 GeV is well described by the simulation.

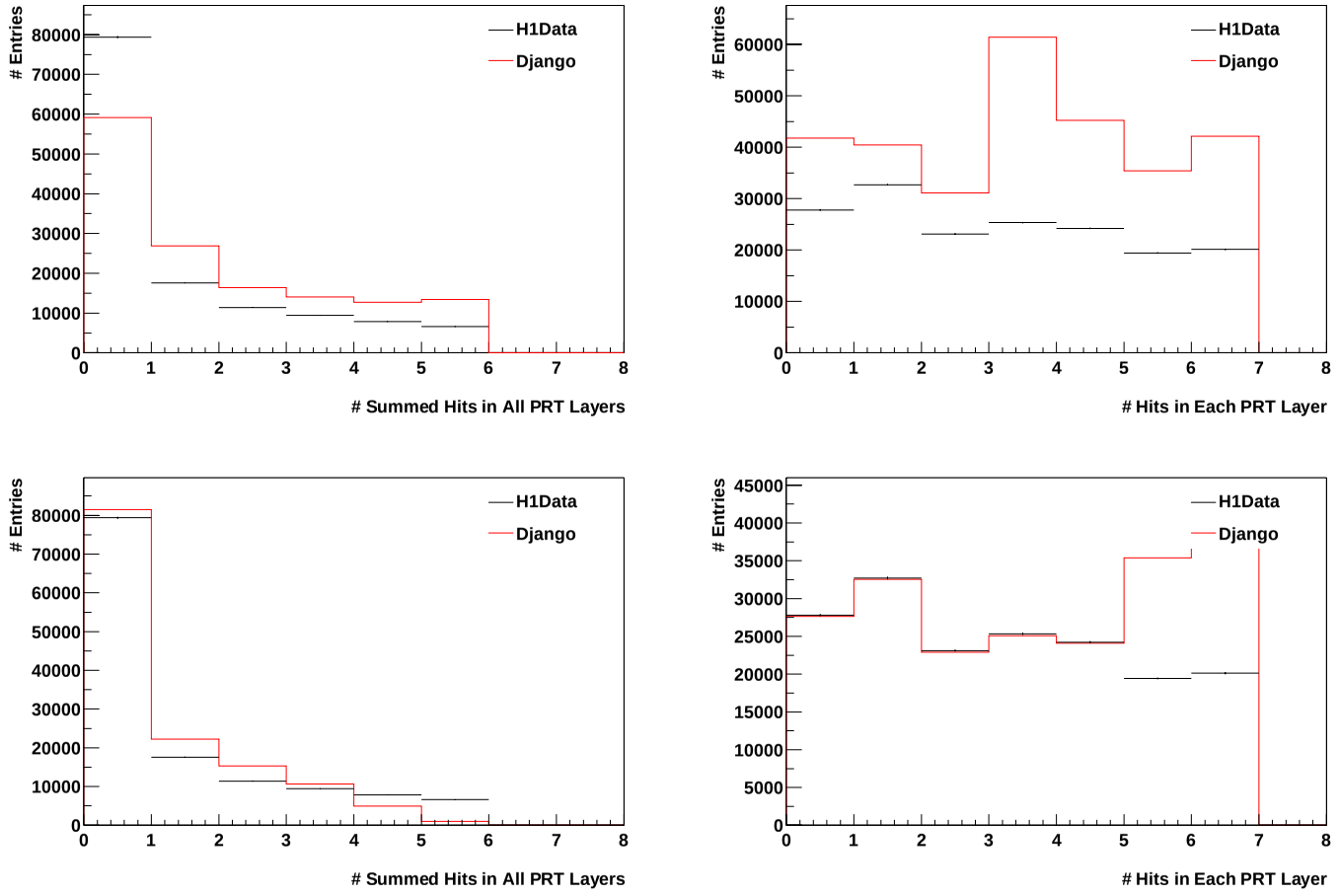

Figure 3.6: *Summed activity in the PRT (left) and the activity in each layer of the PRT (right) before (top) and after (bottom) correction. The data are shown as points, the predictions of the DJANGO simulation are shown as solid red histograms.*

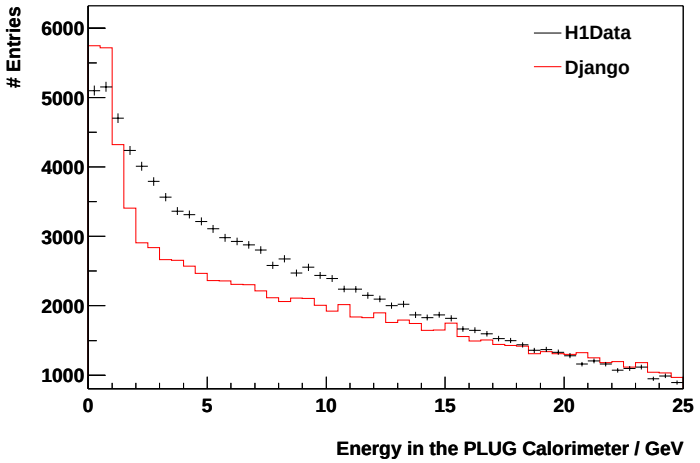

Figure 3.7: *The energy distribution in the PLUG calorimeter. The data are shown as points, the predictions of the DJANGO simulation are shown as solid red histograms.*

The diffractive event selection requires no activity in the PLUG calorimeter above noise levels:

$$E_{PLUG} \leq 3.5 \text{ GeV}. \tag{3.13}$$

3.2.4 The Stability of the Forward Detector Selection

Given the poor description of the data by the available model it is important to determine the extent to which the event selection is dependent on this description. Table 3.4 shows the efficiencies, for data and the DJANGO simulation, of rejecting events with forward energy flow ($\eta_{max} > 3.3$) for several combinations of the forward detectors before and after all corrections and reweights. The efficiency increases with the number of detectors used in the selection and there is very good agreement between data and simulation for the final forward detector selection after applying the reweights.

Selection	Data	Simulation	Simulation (corrected)
FMD ‖ PRT ‖ Plug	0.94	0.97	0.94
PRT ‖ Plug	0.87	0.93	0.88
FMD ‖ Plug	0.91	0.94	0.91
FMD ‖ PRT	0.83	0.92	0.83
FMD	0.73	0.83	0.73
PRT	0.40	0.59	0.40
Plug	0.79	0.83	0.81

Table 3.4: *The efficiency of several diffractive selections for rejecting events with forward energy ($\eta_{max} > 3.3$).*

Selection Description	Values
No forward deposit in the LAC	$\eta_{max} \leq 3.3$
No activity in the FMD	$\sum_{i=0}^{1} N_{FMD,i} \leq 1$ $\sum_{i=0}^{2} N_{FMD,i} \leq 2$
No activity in the PRT	$\sum_{i=0}^{4} N_{PRT,i} = 0$
No activity in the PLUG	$E_{PLUG} \leq 3.5$ GeV

Table 3.5: *The list of cuts used to select diffractive events.*

MC	Allowed Phase-Space
DJANGO	$x_{IP} > 0.15 \parallel M_Y > 5.0$ GeV
RAPGAP	$x_{IP} < 0.15$ & $M_Y \leq M_{proton}$

Table 3.6: *The allowed phase-space for the DJANGO and RAPGAP simulations.*

3.2.5 The Final Diffractive Event Selection

The final selection used to select diffractive events restricts the photon-dissociation system, X, to be fully contained in the main H1 detector while the Y system, a quasi-elastic proton, escapes undetected down the beampipe. The two systems are separated by a large gap in rapidity, guaranteed by the cut on $\eta_{max} < 3.3$ and the lack of any activity in any of the PLUG ($3.5 < \eta < 5.5$), FMD ($5.0 < \eta < 6.5$) or PRT ($6.0 < \eta < 7.5$) above noise levels. The cut values are summarised in table 3.5.

3.2.6 Diffractive DIS Control Distributions

In this section control distributions are used to evaluate the level at which the final high Q^2 diffractive DIS event sample is understood. Several distributions are shown which compare the data to the sample of events made with the RAPGAP MC simulation, with background contributions modelled by the DJANGO, COMPTON and LPAIR MC simulations. The hadronic calibration described in [68] is also briefly studied.

To prevent overlapping in phase-space the DJANGO and RAPGAP simulations are each restricted to non-diffractive DIS and diffractive DIS phase-space respectively. The prescription used is given in table 3.6

General Diffractive DIS Control Distributions

The electron energy distribution of the diffractive subsample of NC events, shown in figure 3.8, is quite different from the inclusive sample, in particular it shows no obvious peak at the electron beam energy. This behaviour is well modelled by the sum of the RAPGAP MC simulation, which peaks at low values of the electron energy, and the sum of the simulations of background processes (dominated by DJANGO) which peak at the electron beam energy.

Both the θ and ϕ distributions resemble, as expected, lower statistic versions of their parent inclusive distributions shown in figure 3.1. Again the sum of the RAPGAP simulation and the total of the background simulations model the data well.

The z_{vtx} and z^e_{impact} distributions shown in figure 3.9 also resemble, as expected, lower statistic versions of the inclusive distributions shown in figure 3.2 and are very well described by the sum of the RAPGAP and background simulations. The distributions of y, E_{mpz} and Q^2 are shown in figure 3.10. While the E_{mpz} and Q^2 distributions resemble their parent distributions in figure 3.3, the y distribution is very different. The diffractive selection, specifically the cut on $\eta_{max} < 3.3$, constrains the measurement to low x and therefore high y, hence the removal of the low y peak.

The Hadronic Calibration

The calibration of the hadronic final state is described in detail in [68]. The first quantity of interest is the "P_T balance", which is the ratio of the P_T of the total hadronic system (P^h_T) and the P_T of the electron (P^e_T). This would be equal to unity for NC events in a perfect detector. The second quantity of interest is the "y balance", the ratio of y measured using the hadrons-only method (y_h) and y measured using the DA method (y_{da}). This would again be equal to unity in a perfect detector. Figure 3.11 shows plots of these two quantities versus the "hadronic angle" (γ_h) which is the polar angle of the hadronic final state. The agreement between data and the sum of the RAPGAP simulation

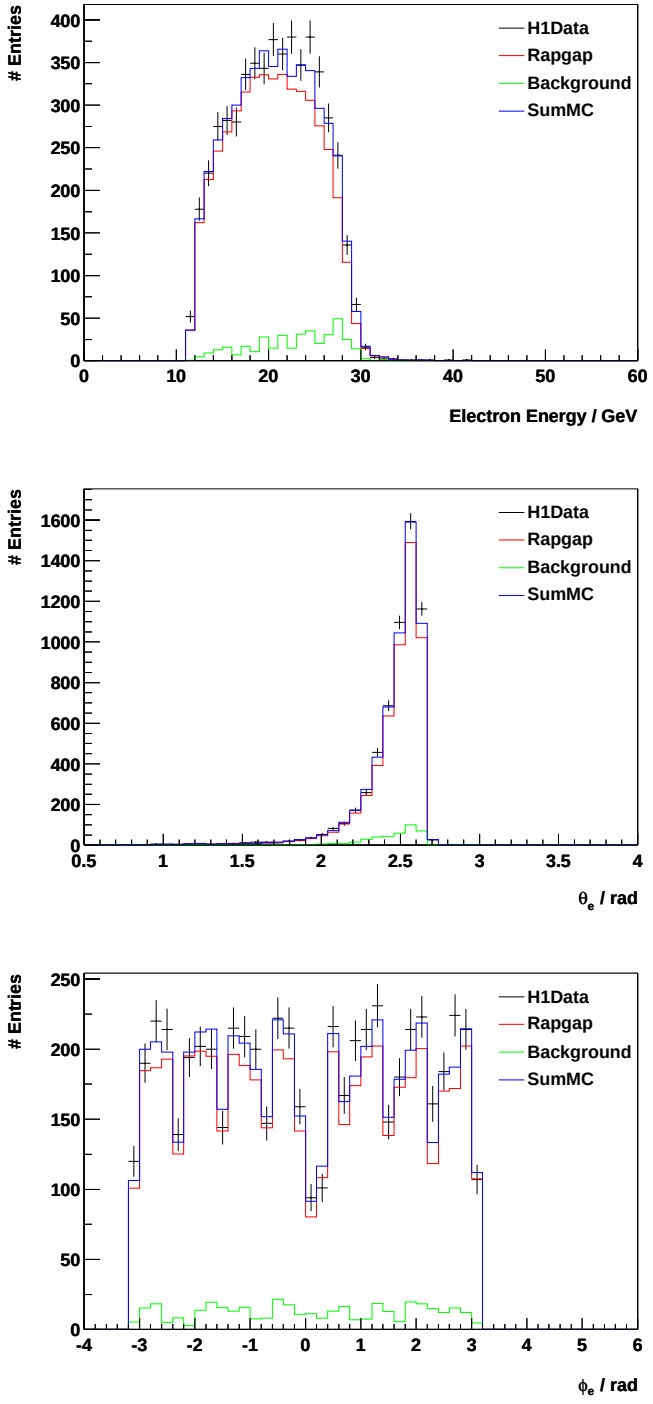

Figure 3.8: *Distributions of the energy (top), the polar angle (middle) and the azimuthal angle of the scattered electron. The data are shown as points, the predictions of the RAPGAP simulation are shown as the solid red histograms, the total background simulation predictions are the solid green histograms and the sum of both are the solid blue histograms.*

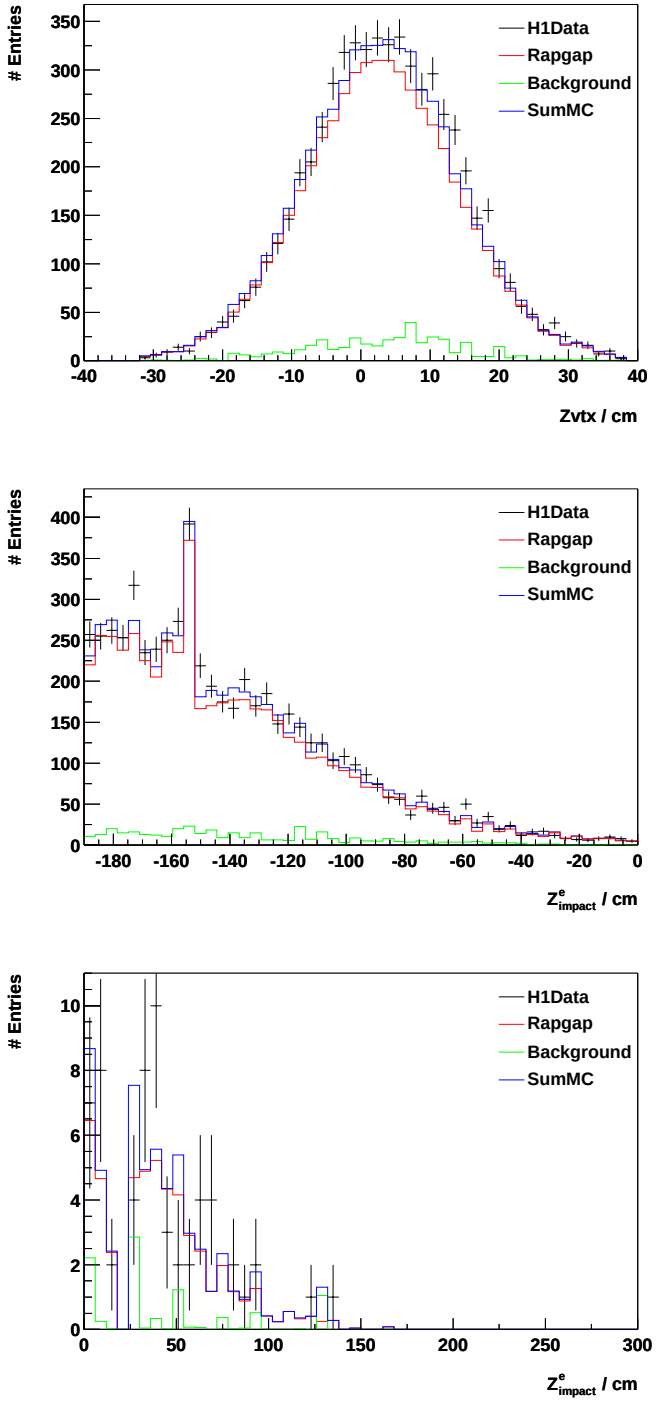

Figure 3.9: *Distributions of the z_{vtx} of the event (top) and z^e_{impact} shown in two ranges, $-190 < z^e_{impact} < 0$ cm (middle) and $0 < z^e_{impact} < 300$ cm (bottom). The data are shown as points, the predictions of the RAPGAP simulation are shown as the solid red histograms, the total background simulation predictions are the solid green histograms and the sum of both are the solid blue histograms.*

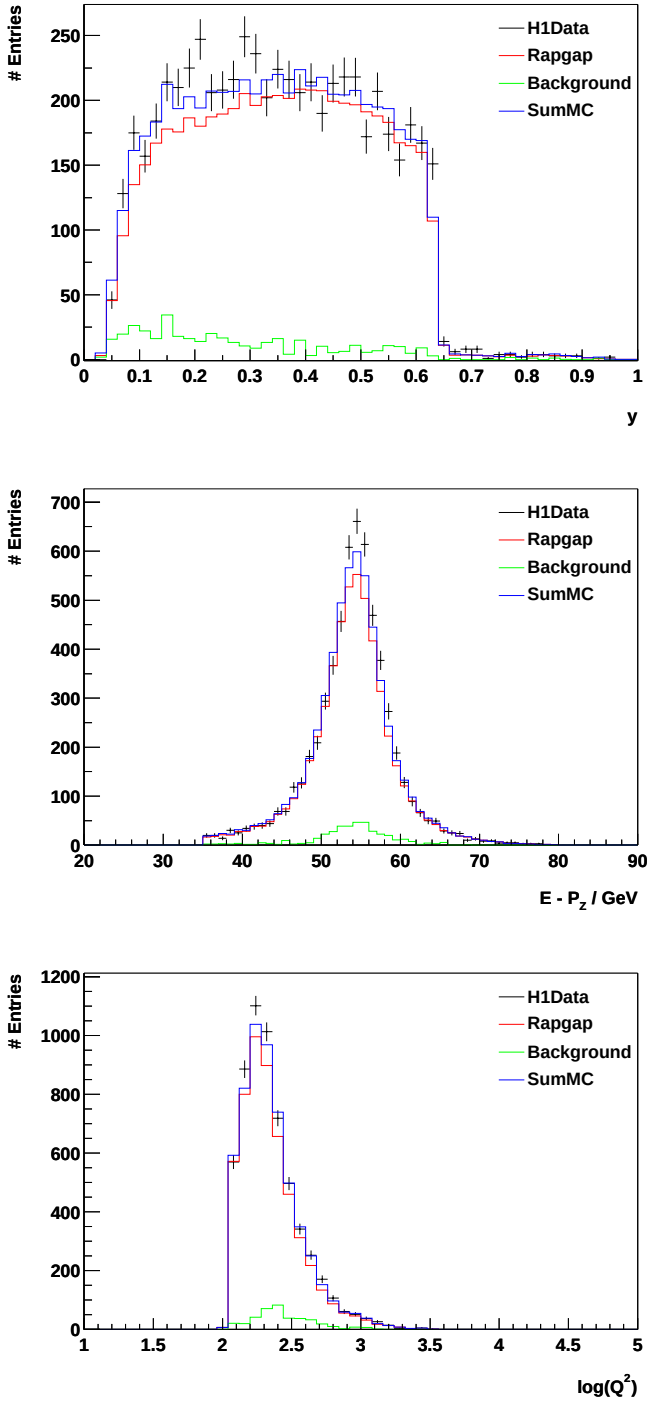

Figure 3.10: *Distributions of the reconstructed y of the event (top), the E_{mpz} (middle) and* $\log Q^2$ *(bottom). The data are shown as points, the predictions of the RAPGAP simulation are shown as the solid red histograms, the total background simulation predictions are the solid green histograms and the sum of both are the solid blue histograms.*

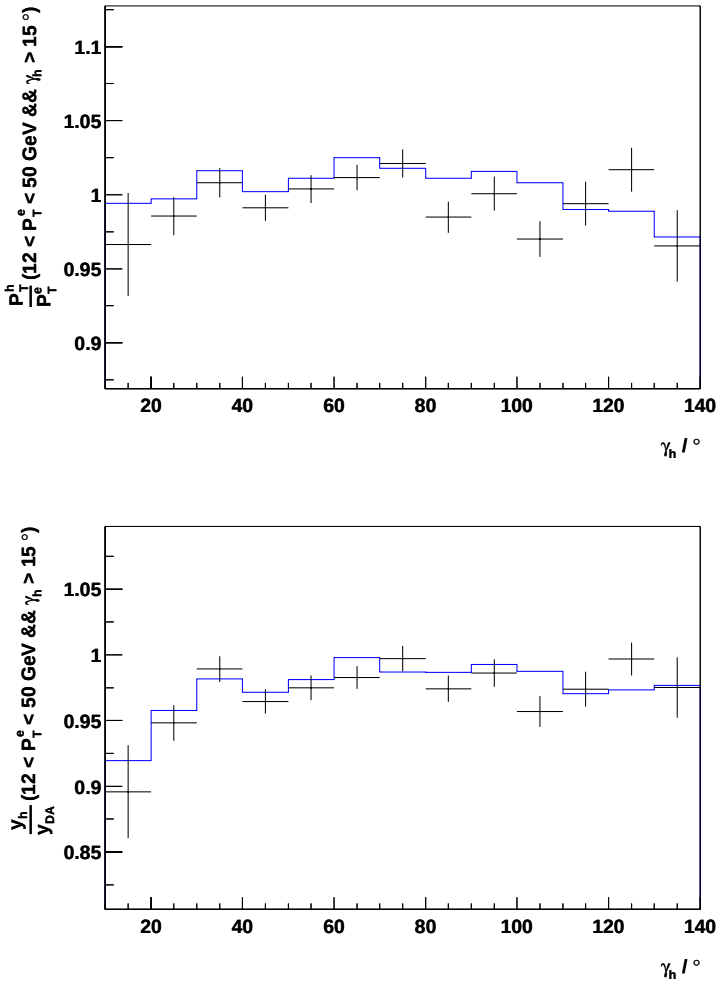

Figure 3.11: *The ratio of the P_T of the hadronic final state system to the P_T of the scattered electron (top) and the ratio of y measured using the hadrons-only method to the y measured using the double-angle method; both quantities are plotted as a function of the hadronic polar angle, γ_h. The data are shown as points, the sum of the RAPGAP and total background simulations is shown as the solid blue histogram.*

and the total background simulations is very good and an uncertainty of 2% on the hadronic calibration is obtained.

3.2.7 Reconstruction of Diffractive Variables

The final state variable necessary to measure the diffractive kinematics shown in equations 1.19 is the mass of the hadronic final state system, M_X. It is obtained in the usual way from the X system with an additional reweight to take advantage of the more optimal resolution in y of the kinematic reconstruction method used. The resulting expression for M_X is shown in equation 3.14.

$$M_X^2 = (E^2 - p_x^2 - p_y^2 - p_z^2)_{hadrons} \cdot \frac{y}{y_h}. \tag{3.14}$$

The M_X Correction

The reconstructed mass of the X system was found to be underestimated on average by $\sim 7\%$, as can be seen in figure 3.12. At high ($M_X > 20$ GeV) this underestimation was found to vary very slightly and linearly with M_X. At lower values of M_X the underestimation becomes much worse as M_X decreases. The quantity

$$\delta(M_X^{rec}) = \frac{M_X^{gen}}{M_X^{rec}} \tag{3.15}$$

was evaluated for the RAPGAP simulation. Two functions were then fitted to the distribution in the two M_X ranges enabling the calculation of an M_X-dependent correction factor; a linear function for $M_X > 20$ GeV and a 7th order polynomial (chosen as it gave the best description) for $M_X \leq 20$ GeV. The correction factor is then applied to both data and simulation in order to correctly reconstruct M_X. Figure 3.12 shows the quantity $\delta(M_X^{rec})$ as a function of M_X^{rec} together with the two functions. The final reconstruction of M_X is then:

$$M_X^2 = (E^2 - p_x^2 - p_y^2 - p_z^2)_{hadrons} \cdot \frac{y}{y_h} \cdot \delta(M_X). \tag{3.16}$$

As t is not measured in this analysis the diffractive kinematics are reconstructed according to equation 3.17.

$$\beta = \frac{Q^2}{Q^2 + M_X^2}, \qquad x_{IP} = \frac{x}{\beta} \tag{3.17}$$

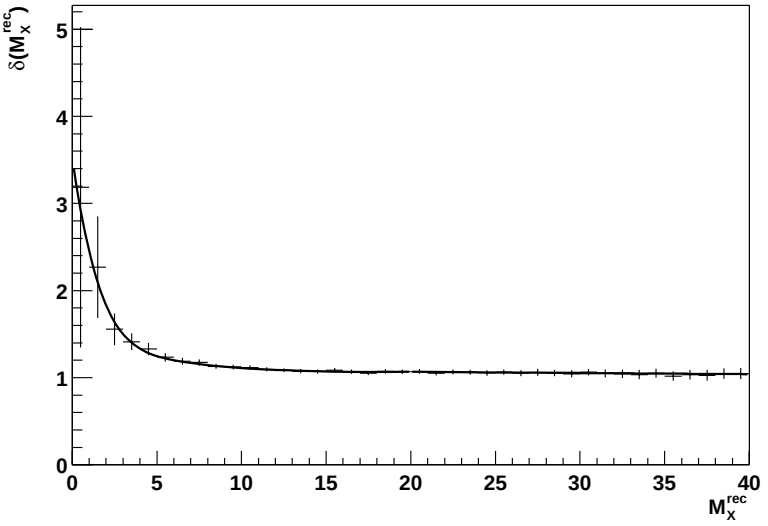

Figure 3.12: *The quantity $\delta(M_X^{rec})$ as a function of M_X together with the two functions fit to $M_X \leq 20$ GeV and $M_X > 20$ GeV.*

Figure 3.13 shows the reconstructed $\log x_{IP}$ and β distributions for the diffractive event sample. The rising slope of the $\log x_{IP}$ distribution, the position of the peak and the fall of the distribution at high $\log x_{IP}$ are all well described by the sum of the RAPGAP simulation and the total of the background simulations. The background processes, which are dominated by non-diffractive DIS, are seen to contribute predominantly at large $\log x_{IP}$. The steep rise of the β distribution followed by a gradual fall towards larger values of β is also well described by the total simulation. The background processes, which are again dominated by non-diffractive DIS, are approximately flat as a function of β. In the highest β bin the elastic QED Compton process is predicted to dominate, a detail not visible in figure 3.13.

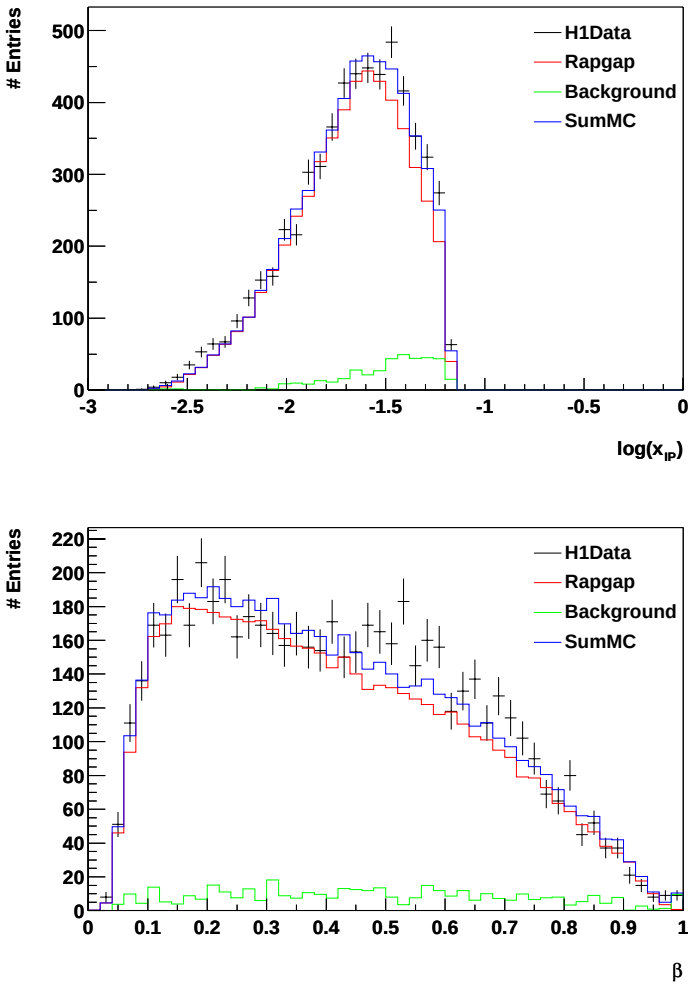

Figure 3.13: *The logarithm of the reconstructed x_{IP} of the event (top), and the reconstructed β (bottom). The data are shown as points, the predictions of the RAPGAP simulation are shown as the solid red histograms, the total background simulation predictions are the solid green histograms and the sum of both are the solid blue histograms.*

Chapter 4

Extraction of the Diffractive Reduced Cross-Section $\sigma_r^{D(3)}$

In this chapter the procedure used to extract the diffractive reduced cross-section $\sigma_r^{D(3)}$ is presented. The choice of binning scheme is presented first followed by the definition of the cross-section. The definitions used to quantify the quality of a bin and the model-dependent corrections that are applied to extract the cross-section are then explained. Finally, the full set of systematic error sources for the measurement are presented.

4.1 Bin Selection

Two binning schemes are used in the measurement. The first binning scheme is used to test the Regge factorisation hypothesis (see section 1.5.2). According to this hypothesis the reduced cross-section should not depend on x_{IP} other than in normalisation which can be parameterised by a flux factor, $f_{x_{IP}}$. The measurement is therefore binned in x, Q^2 and x_{IP} and the diffractive reduced cross-section can be extracted using:

$$\sigma_r^{D(3)}(\beta, Q^2, x_{IP}) = \frac{xQ^4}{4\pi\alpha^2(1-y+\frac{y^2}{2})}\frac{d^3\sigma_{ep\to eXY}}{dxdQ^2dx_{IP}}. \tag{4.1}$$

The main goal of the second binning scheme is to measure the diffractive

reduced cross-section using the highest resolution possible. This allows an extraction of the greatest number of data points possible to provide the best constraints for a fit and the best comparisons with various theoretical models. The measurement is therefore binned in x, Q^2 and β and the diffractive reduced cross-section is extracted using:

$$\sigma_r^{D(3)}(\beta, Q^2, x_{IP}) = \frac{\beta^2 Q^4}{4\pi\alpha^2(1 - y + \frac{y^2}{2})} \frac{d^3\sigma_{ep\to eXY}}{dx dQ^2 d\beta}. \tag{4.2}$$

The first binning scheme allows a full QCD fit to the data within the scope of QCD Hard Scattering Factorisation (see section 1.5.1). However, due to the limited resolution in x_{IP} available the approach used is to test the Regge factorisation hypothesis using the first binning method and then perform a fit to the data using the second binning method.

A view of the $Q^2 - \beta$ kinematic plane is shown in figure 4.1, where the phase-space covered by previous diffractive measurements by the H1 collaboration are shown, along with the phase-space covered by this measurement. This measurement extends the phase-space in both Q^2 and β of diffractive measurements and increases the statistical significance of the data; it supercedes the previous H1 measurement at high Q^2 [75].

4.2 Cross-Section Definition

The cross-section is given by:

$$\frac{d^3\sigma_{ep\to eXY}}{d\beta dQ^2 dx} = \frac{N_{Data} - N_{BG}}{\mathcal{L}} \frac{BCC * RC}{\mathcal{A}} \tag{4.3}$$

where N_{Data} is the measured number of events in the data, N_{BG} is the total number of events from all background processes and $\mathcal{L}$ is the integrated luminosity of the data. The *Acceptance* correction, $\mathcal{A}$, Bin Centre Corrections (BCC) and Radiative Corrections (RC) are detailed in the following section. It should also be noted that equation 4.3 is also valid in the other binning scheme. This is also true of the expressions used in section 4.3.3 with an appropriate change of variables.

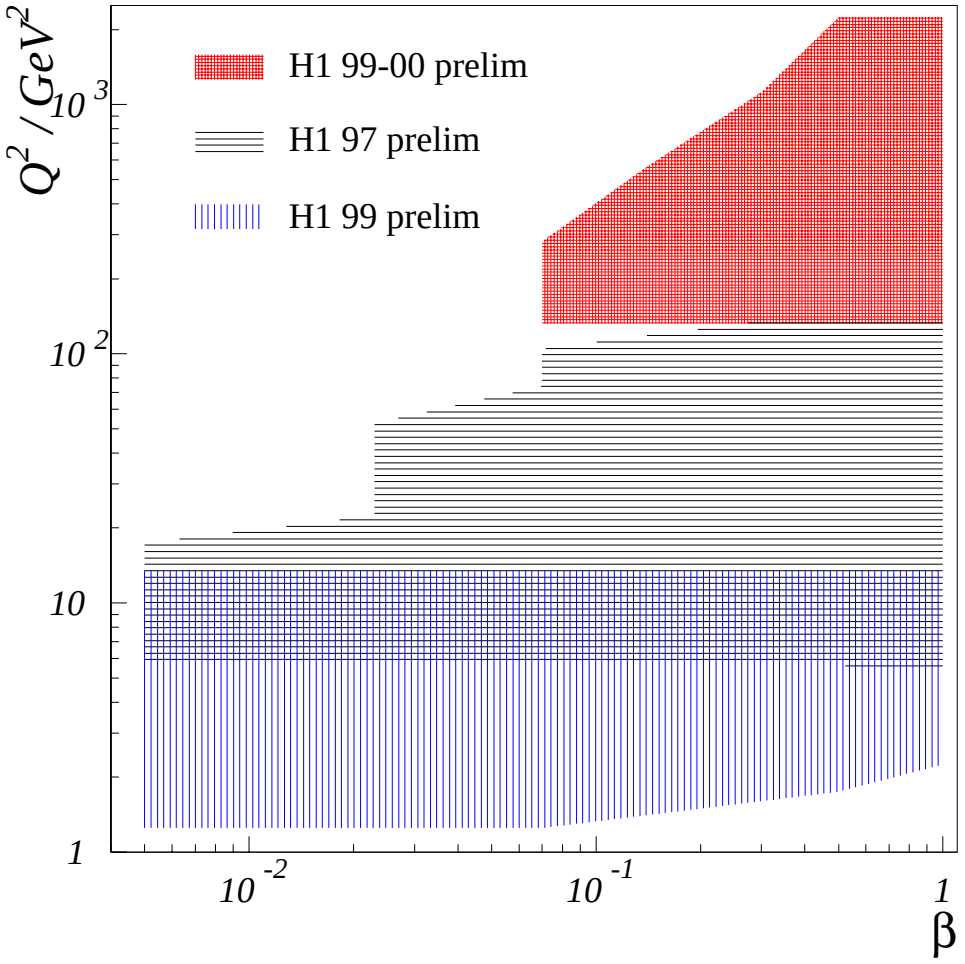

Figure 4.1: *The $Q^2 - \beta$ kinematic plane showing the phase-space covered by previous diffractive measurements from the H1 collaboration and the phase-space covered by this measurement.*

4.3 Correcting Data Using Simulations

In order to extract a true measurement from the data several effects need to be corrected for. Firstly, the measurement is made using a real detector, consisting of detector components which have finite resolutions, efficiencies and geometric acceptances. These effects are corrected for by the *Acceptance* correction. Secondly, the cross-section measurement is divided up into bins of finite size. In the case of this measurement these bins are cubic, but kinematic and geometric cuts can reduce the effective size of these bins. In addition, the shape of the cross-section will almost certainly change across the bin; the BCCs correct for these effects. Finally, QED radiation can change the measured kinematics of the event from the kinematics of the underlying event; RCs correct for this effect.

4.3.1 The *Acceptance* Correction

In order to extract a true measurement from the data the various effects of the detector need to be corrected for, i.e. the finite detector resolutions, efficiencies and geometric acceptances. To do this, events from a MC generator, RAPGAP in the case of this analysis, are compared before and after they are passed through the detector simulation, labelled generator (GEN) level and reconstructed (REC) level, respectively. If the REC level events describe the data in every detail, then it is possible to correct the data for the effects of the detector. If deficiencies are found in the simulation, for example the resolution of a particular detector is not modelled correctly, then the simulated resolution is corrected to the data in order to obtain a better description. The remaining differences between data and simulation are accounted for by systematic errors.

The effects of the detector are studied by looking at the relationships between GEN level events and REC level events. Cuts are placed on a simulated event at both the GEN and REC levels. This leaves four scenarios which can

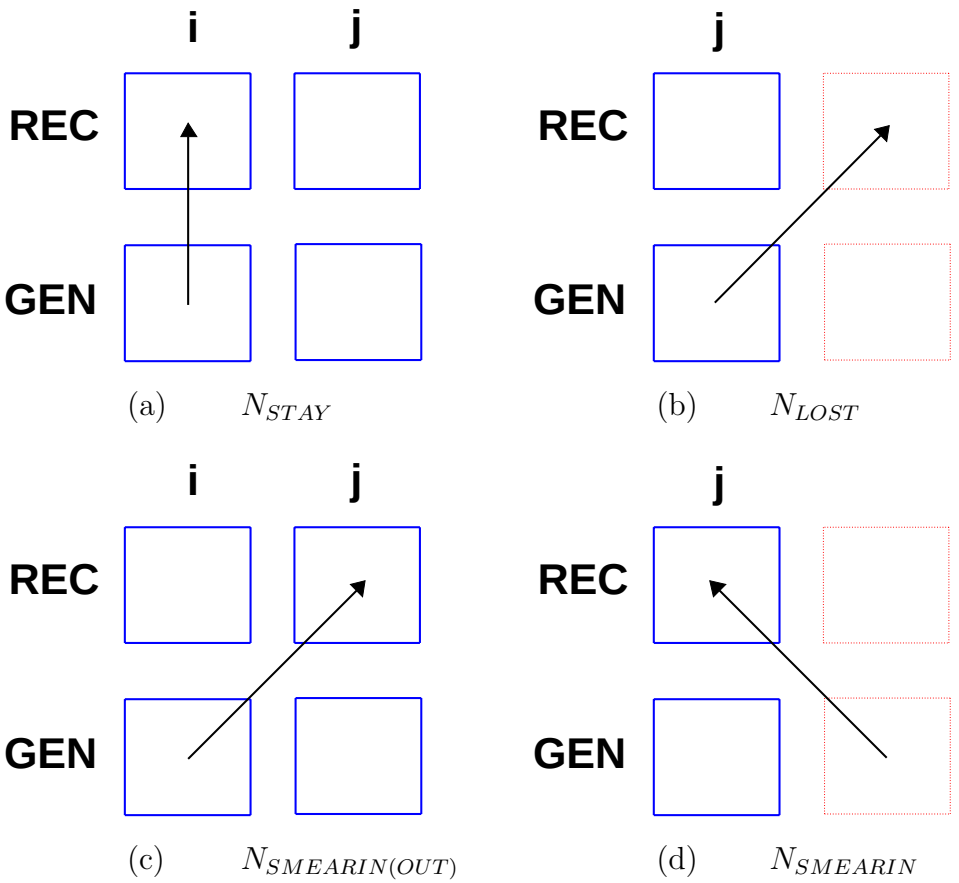

Figure 4.2: *Schematic showing the dynamics of bin migrations, arrows show the path of an event from the GEN level to the REC level, thick-blue squares are bins inside the measured phase-space, dotted-red squares are bins outside of the measured phase-space; (a) is an illustration of the situation where an event has the same GEN and REC bin; (b) shows a GEN event being lost from the REC sample by being reconstructed outside of the measured phase-space; (c) illustrates an event smearing out of a GEN bin into a REC bin; finally, (d) shows an event smearing into a REC bin from outside of the GEN phase-space, i.e. a reconstructed event without a GEN bin.*

be described by four independent variables, illustrated in figure 4.2.

The four independent variables are defined as:

- N_{STAY} = The number of events which have the same GEN and REC bin number (i)
- N_{LOST} = The number of events with a GEN bin (j) but no REC bin
- $N_{SMEARIN}$ = The number of events which smeared into a REC bin (j)

- $N_{SMEAROUT}$ = The number of events which smeared out of a GEN bin (i)

The total number of GEN and REC events are then defined as:

- $N_{REC} = N_{STAY} + N_{SMEARIN}$
- $N_{GEN} = N_{STAY} + N_{SMEAROUT} + N_{LOST}$

Using these definitions the following three variables are used to quantify the relationships between GEN and REC events:

$$Acceptance = \frac{N_{REC}}{N_{GEN}} \tag{4.4}$$

$$Purity = \frac{N_{STAY}}{N_{REC}} \tag{4.5}$$

$$Stability = \frac{N_{STAY}}{N_{GEN} - N_{LOST}}. \tag{4.6}$$

Binomial errors are calculated for *Acceptance*, *Purity* and *Stability* using the four independent variables.

The *Acceptance* of a bin quantifies the number of events reconstructed in a bin compared to the true number of events generated in that bin for an area of phase-space defined by the bin. This quantity is also known as the "Smeared Acceptance" as all reconstruction effects are accounted for, i.e. all smearing effects are included. The true number of events present in the data, N_{True}, is recovered by applying the *Acceptance* correction, i.e.

$$N_{True} = N_{Data} \times \frac{N_{GEN}}{N_{REC}} = \frac{N_{Data}}{\mathcal{A}} \tag{4.7}$$

The effects of smearing are quantified using *Purity* and *Stability*. The *Purity* of a bin quantifies the fraction of REC events which had the same GEN bin. The *Stability* quantifies the fraction of GEN events which have the

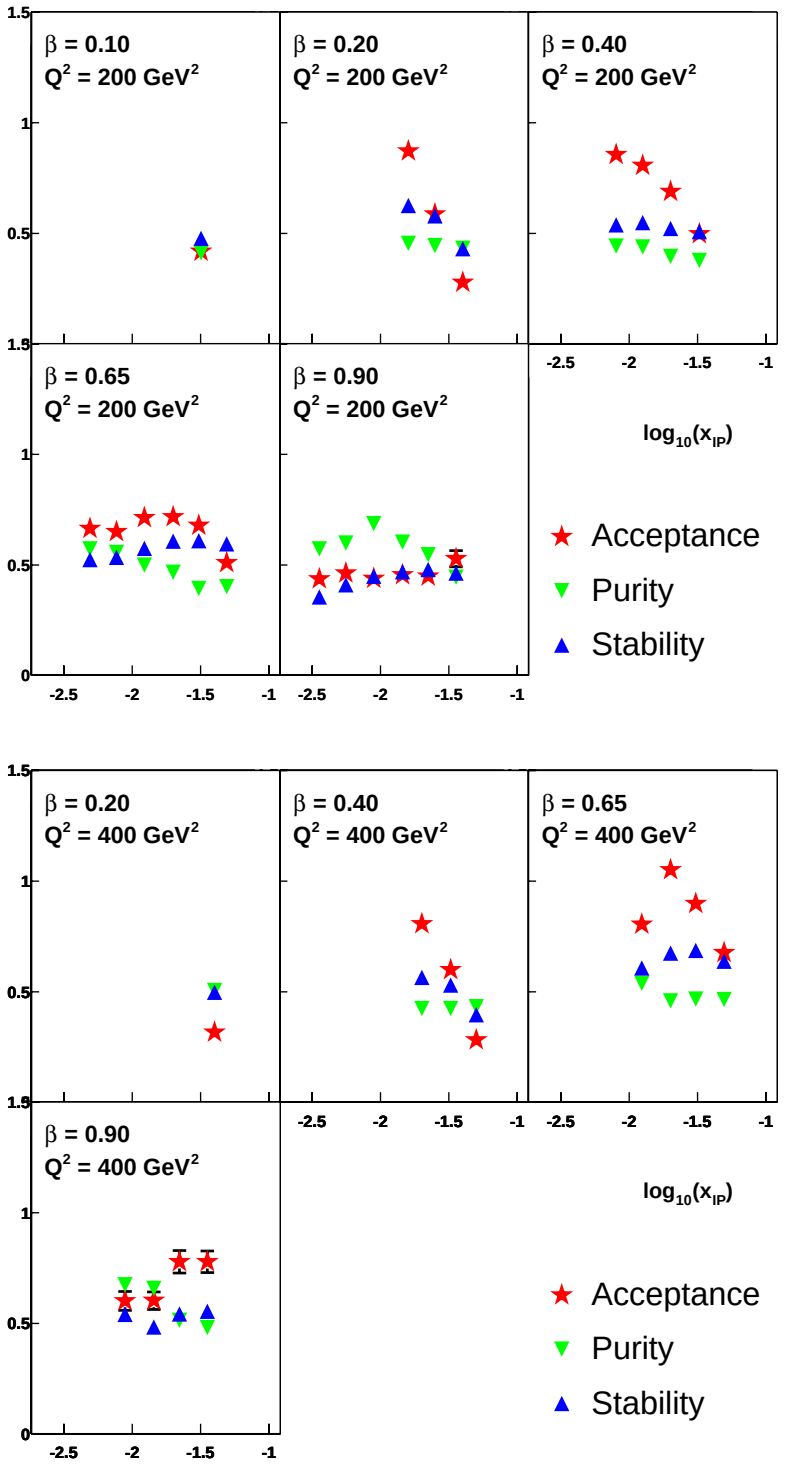

Figure 4.3: *The Acceptance, Purity and Stability of the measurement for* $Q^2 = 200.0$ *(top) and* $Q^2 = 400.0$ GeV^2 *(bottom), shown as a function of* $\log_{10} x_{IP}$ *in bins of fixed* β.

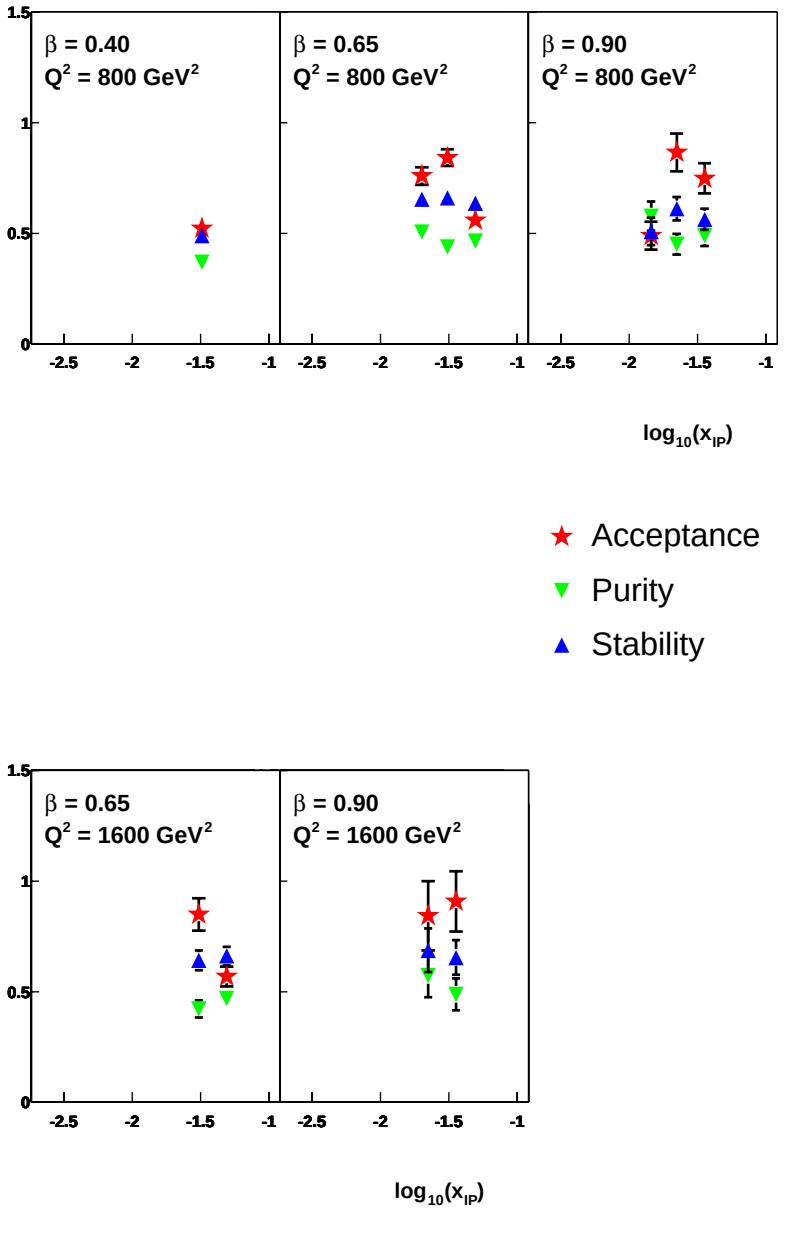

Figure 4.4: *The Acceptance, Purity and Stability of the measurement for* $Q^2 = 800.0$ *(top) and* $Q^2 = 1600.0$ GeV^2 *(bottom), shown as a function of* $\log_{10} x_{IP}$ *in bins of fixed* β.

same REC bin, without taking into account events that are lost (as this is taken into account by the *Acceptance*).

The values of *Acceptance*, *Purity* and *Stability* are plotted as a function of $\log_{10} x_{IP}$ in bins of constant Q^2 and β in figures 4.3 and 4.4. The effect of the η_{max} cut can clearly be seen on the *Acceptance* of the measurement at low β; the η_{max} cut is equivalent to a cut on the X system, so at the lowest β, which corresponds to the highest M_X, the *Acceptance* decreases as x_{IP} increases (as $x = \frac{x_{IP}}{\beta}$). As β increases the effect is less pronounced as M_X is smaller for the same value of x_{IP}. As Q^2 increases M_X is larger for the same value of β, resulting in the decrease in the number of β bins. The *Purity* of all bins is approximately flat across the measured phase-space, except at the highest x_{IP} and lowest β where it decreases due to high M_X events smearing into the sample. The *Stability* is also approximately flat across the measured phase-space, with a slight tendency to decrease with increasing x_{IP} due to the increasingly poor resolution in x_{IP} with increasing x_{IP}.

The values of *Acceptance*, *Purity* and *Stability* for each bin used in this measurement must satisfy:

$$\begin{aligned} \textit{Acceptance} &> 30\% \\ \textit{Purity} &> 30\% \\ \textit{Stability} &> 30\% \end{aligned}$$

in order to guarantee that the contents of the bin are well understood. The low values are due to the cubic geometry of the bins required for this analysis, i.e. events are able to migrate in three dimensions. 30% is approximately equivalent to 1 σ in each of the three dimensions, i.e. $(68\%)^3 \simeq 30\%$.

4.3.2 The Proton Dissociation Acceptance Correction

The measured range in M_Y and t is defined by the acceptance of the forward detectors and is given in equation 3.8. There will also be migration of events across these kinematic boundaries from proton dissociation events and this

needs to be accounted for. The RAPGAP programme currently only simulates elastic proton events and therefore the DIFFVM programme was used to simulate proton dissociation events in order to estimate this acceptance correction. The proton dissociation acceptance correction, $PDAC$, is defined as:

$$PDAC = \frac{N^{PD}_{REC} + R^{EL}_{PD} N^{PD}_{GEN}}{N^{PD}_{GEN}(M_Y < 1.6 \text{ GeV}, |t| < 1 \text{ GeV}^2) + R^{EL}_{PD} N^{PD}_{GEN}} \tag{4.8}$$

where N^{PD}_{REC} is the number of reconstructed proton dissociation events, N^{PD}_{GEN} is the total number of proton dissociation events, $N^{PD}_{GEN}(M_Y < 1.6$ GeV, $|t| < 1$ GeV^2) is the number of proton dissociation events generated in the kinematic range given by equation 3.8 and R^{EL}_{PD} the ratio of the elastic to the dissociative cross-sections. The value of R^{EL}_{PD} is estimated to be 1 but is only constrained by experiment to be in the range $0.5 < R^{EL}_{PD} < 2.0$ [76–78]. Note that the number of reconstructed elastic events in equation 4.8 is taken to be the number of generated events as the effects of smearing of elastic proton events is already contained in the *Acceptance* correction calculated using the RAPGAP programme. The final value of the *Acceptance* correction used in equation 4.3 is then the product of the *Acceptance* correction calculated using the RAPGAP programme and $PDAC$.

The value of $PDAC$ was found to be:

$$PDAC = 1.081 \pm 0.003 \tag{4.9}$$

where the error is the statistical error only. The sources of systematic errors on this correction are discussed in section 4.4.

4.3.3 Bin Centre Corrections

The Bin Centre Corrections adjust the measurement of the cross-section in a bin of finite size to the quoted bin centres. There are two effects to consider, firstly the effect of the finite size and geometric shape of the bin, which may or may not be cubic, and secondly the shape of the cross-section across the bin. The bin centres are chosen so as to keep this correction small and are denoted using obvious notation as β_C, Q^2_C, x_C so that the corrections are given by:

$$BCC = \frac{\frac{d^3\sigma}{d\beta dQ^2 dx}\big|_{\beta=\beta_C, Q^2=Q^2_C, x=x_C}}{\int_{\beta_{min}}^{\beta_{max}} \int_{Q^2_{min}}^{Q^2_{max}} \int_{x_{min}}^{x_{max}} \frac{d^3\sigma}{d\beta dQ^2 dx} d\beta dQ^2 dx} \tag{4.10}$$

All generator-level cuts are applied when calculating the BCCs to take account of any non-cubic nature of the bins, which is important at the edges of phase-space.

The bin centre corrections are plotted as a function of $\log_{10} x_{IP}$ in bins of constant Q^2 and β in figures 4.5 and 4.6. The value of the BCC has been multiplied by the bin volume, under the assumption that it is cubic, for each bin, in order to show the non-trivial effects of non-cubic bins and the shape of the cross-section across a bin.

In the highest Q^2 bin the corrections are approximately unity in the highest $\log_{10} x_{IP}$ bin with the effect of the y cut, $y_e < 0.9$, being to increase the correction in the lower $\log_{10} x_{IP}$ bin. In the lower Q^2 bins the effective electron energy cut, $y_e < 0.63 \parallel Q^2_e > 890.0$ GeV^2, produces the same effect at a higher value of $\log_{10} x_{IP}$. Finally, the lowest Q^2 bin shows both the effect of the effective electron energy cut and the electron theta cut, $\theta_e < 153.0°$, which increases the value of the correction with increasing $\log_{10} x_{IP}$, giving rise to the $V-$shape.

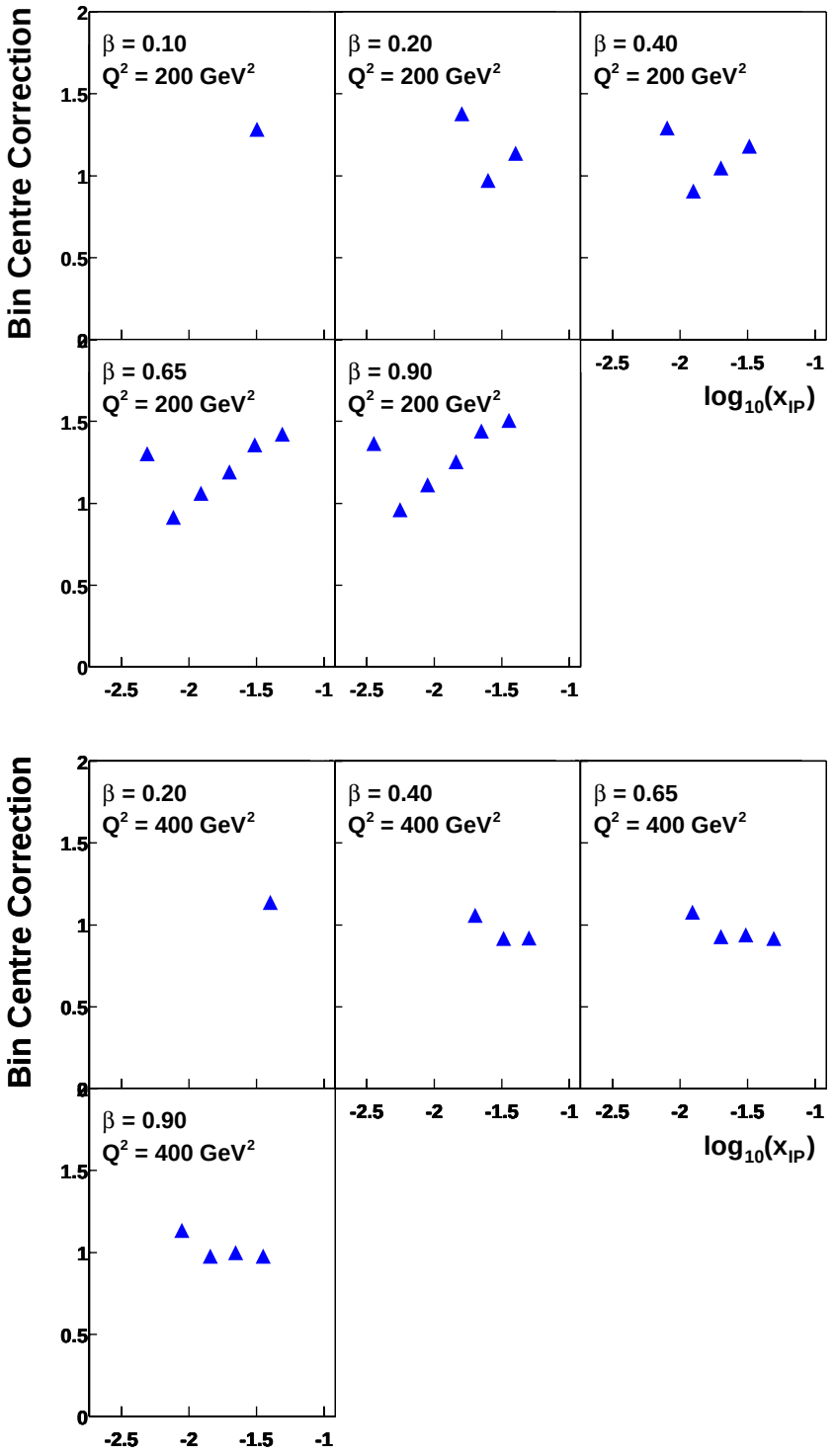

Figure 4.5: *The Bin Centre Corrections calculated for this measurement for* $Q^2 = 200.0$ *(top) and* $Q^2 = 400.0$ GeV^2 *(bottom), shown as a function of* $\log_{10} x_{IP}$ *in bins of fixed* β*. The bin volume effects have been removed (see text).*

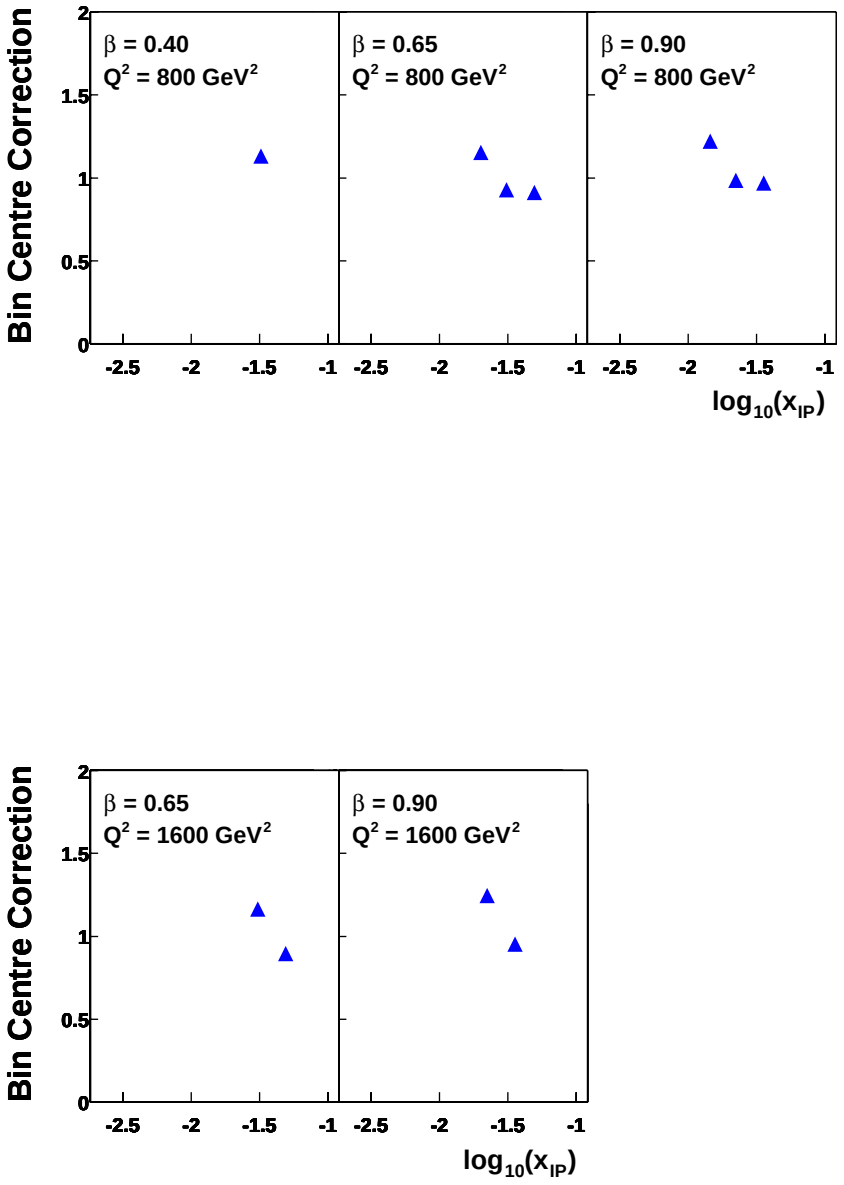

Figure 4.6: *The Bin Centre Corrections calculated for this measurement for* $Q^2 = 800.0$ *(top) and* $Q^2 = 1600.0$ GeV^2 *(bottom), shown as a function of* $\log_{10} x_{IP}$ *in bins of fixed* β*. The bin volume effects have been removed (see text).*

4.3.4 Radiative Corrections

The sources of radiative corrections are discussed in section 1.6.2. FSR tends to produce a photon which is collinear with the electron and hence the electron-photon pair are detected as a single electromagnetic energy cluster. The electron-photon pair is then reconstructed as a single electron with the correct energy, resulting in only a small correction. ISR reduces the centre of mass energy, thereby having a large effect on the reconstructed kinematics of the event. This effect is reduced by the cut on E_{mpz} at 35.0 GeV, which allows a maximum photon energy of 10.0 GeV.

The radiative corrections are defined as the ratio of the cross-section, as calculated by RAPGAP and HERACLES, with and without QED radiation, i.e.

$$RC = \frac{\sigma}{\sigma_{RAD}}. \tag{4.11}$$

The radiative corrections are plotted as a function of $\log_{10} x_{IP}$ in bins of constant Q^2 and β in figures 4.7 and 4.8. The corrections are approximately equal to unity at the lowest $\log_{10} x_{IP}$ and increase with increasing $\log_{10} x_{IP}$. At high β there is a tendency for the correction to decrease again with increasing $\log_{10} x_{IP}$ at the highest $\log_{10} x_{IP}$; this effect is most pronounced in the lowest Q^2 bin.

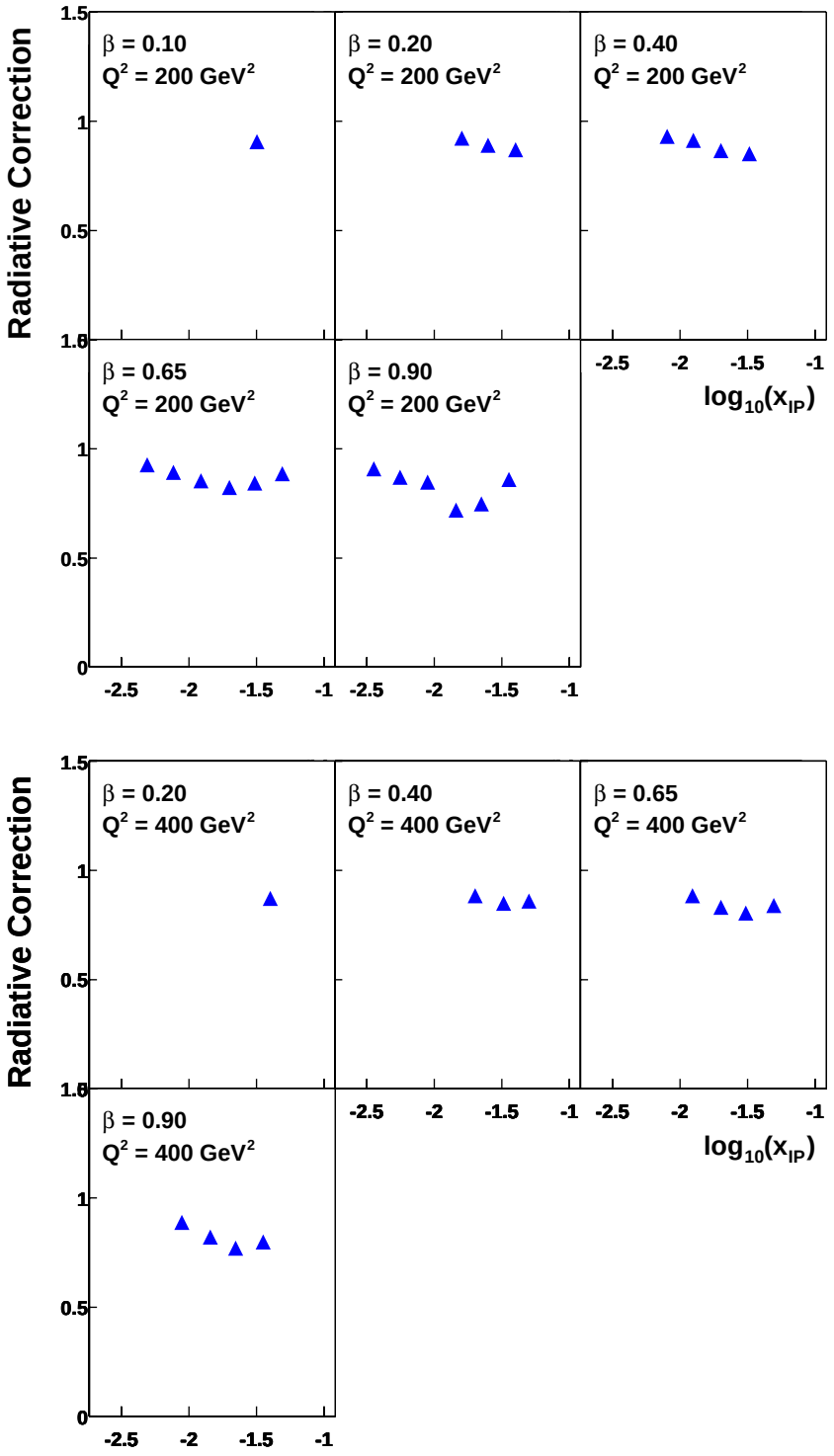

Figure 4.7: *The Radiative Corrections calculated for this measurement for* $Q^2 = 200.0$ *(top) and* $Q^2 = 400.0$ GeV^2 *(bottom), shown as a function of* $\log_{10} x_{IP}$ *in bins of fixed* β.

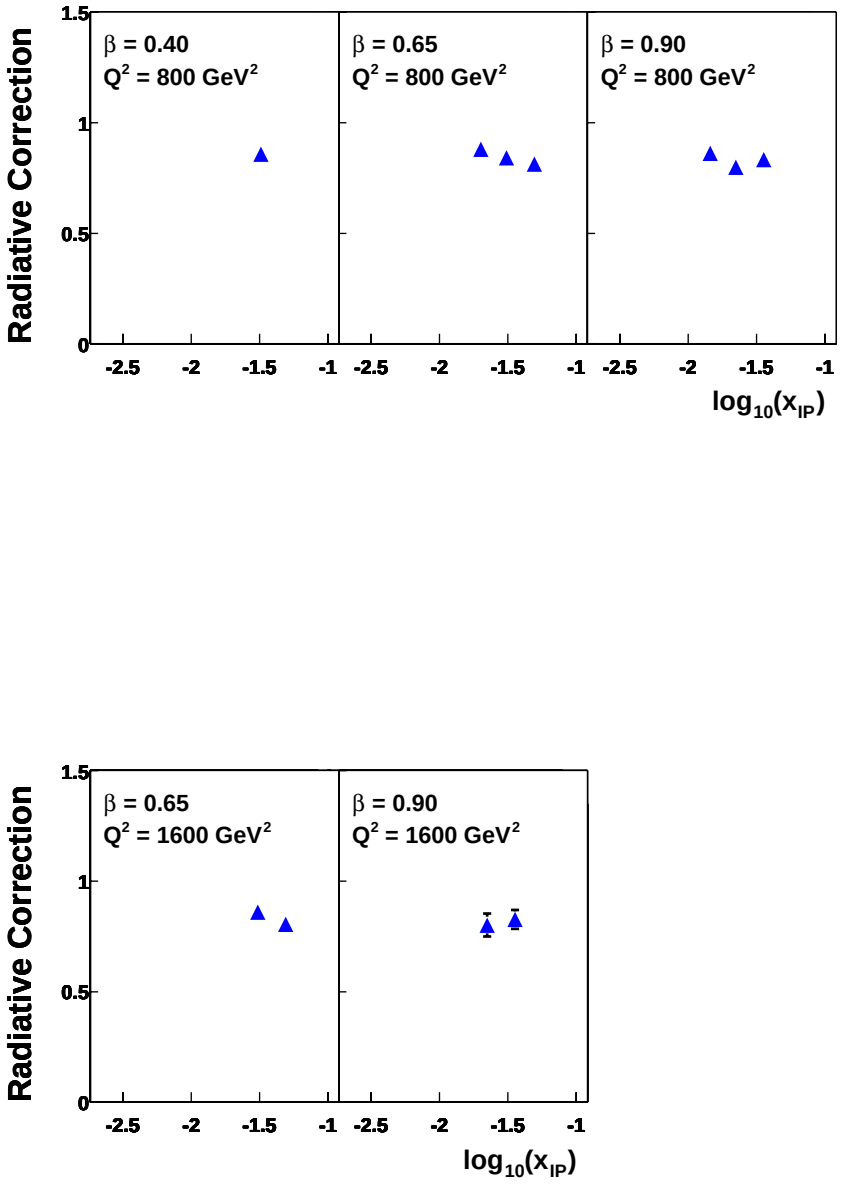

Figure 4.8: *The Radiative Corrections calculated for this measurement for* $Q^2 = 800.0$ *(top) and* $Q^2 = 1600.0$ GeV^2 *(bottom), shown as a function of* $\log_{10} x_{IP}$ *in bins of fixed* β.

4.4 Systematic Uncertainties on the Measurement

All of the sources of systematic uncertainties in the measurement lead to a corresponding error on the final measurement. Presented in the following is the fractional percentage error on the error source considered along with the resulting fractional percentage error on the diffractive reduced cross-section $\sigma_r^{D(3)}(\beta, Q^2, x_{IP})$, simply referred to as "the measurement" in the following. The fractional percentage error on the measurement is presented in the form $[L, A, H]$, where L is the lowest value of the uncertainty in any bin, A the average uncertainty and H the highest value of the uncertainty in any bin.

Sources of error which have a 100% bin-to-bin correlation give rise to the same error in all bins and are:

- The uncertainty due to the luminosity measurement is 1.5% [13], resulting in an uncertainty on all bins of the measurement of 1.5%.

- The uncertainty on the M_Y distribution used in DIFFVM arises from our *a priori* ignorance of it. The input distribution is reweighted by a factor of $(\frac{1}{M_Y^2})^{\pm 0.3}$ resulting in an uncertainty on all bins of the measurement of 0.07 %.

- The t dependence of the proton-dissociation cross-section used in DIFFVM is better constrained than that for the elastic cross-section. The input distribution is reweighted by $e^{\pm t}$ resulting in an uncertainty on all bins of the measurement of 0.09%.

- The efficiency of the PRT is not well modelled by the simulation and results in an uncertainty on $PDAC$. The systematic error on $PDAC$ is estimated by applying 0.5 and 2 times the overall reweight factors used and results in an uncertainty on the measurement, which is the same for all bins, of 4.8%.

- The efficiency of the FMD is also not well modelled by the simulation and results in an uncertainty on $PDAC$. The systematic error on PDAC

is estimated by decreasing the FMD efficiency by 10 %. The resulting uncertainty on the measurement is 1.1% and is the same for all bins.

- The uncertainty on the energy scale of the PLUG calorimeter is 30% and also results in an uncertainty on PDAC. The resulting uncertainty on all bins of the measurement is 0.2%.

Sources of error which are considered to have bin-to-bin correlations of less than 100% are:

- The uncertainty on the electron energy depends on the impact position in z of the electron in the LAC. It is 1% in the backward part of the LAC and 0.7% for the range $-150 < z^{e}_{impact} < 20$ cm [13] leading to an uncertainty on the measurement of $[0.02, 1.6, 5.3]$.

- The uncertainty on the electron polar angle is θ-dependent. For $\theta > 135^{\circ}$ it is 1 mrad increasing to 2 mrad for the range $135^{\circ} > \theta > 120^{\circ}$ and 3 mrad for $\theta < 120^{\circ}$ [13]. This leads to an uncertainty on the measurement of $[0.0, 0.7, 2.4]$.

- The uncertainty on the amount of hadronic energy measured in the LAC is determined in section 3.2.6 and is 2%. This leads to an uncertainty on the measurement of $[0.06, 1.2, 6.1]$.

- The uncertainty on the amount of hadronic energy measured in the SPACAL is 7% [79] and leads to an uncertainty on the measurement of $[0.0, 0.02, 0.5]$.

- The uncertainty on the amount of energy due to noise in the LAC is 25% [68]. This leads to an uncertainty on the measurement of $[0.5, 5.3, 23.0]$.

- The uncertainty on the number of background events in the final event sample is estimated by increasing the total background contribution beyond the point at which the sum of signal and background simulations can describe the data. The uncertainty estimated using this

method is 50% and this leads to an uncertainty on the measurement of $[0.2, 5.7, 17.0]$.

- The uncertainty on the amount of energy measured in tracks is 3% [13] and leads to an uncertainty on the measurement of $[0.0, 0.6, 4.1]$.

- The uncertainty on the x_{IP} distribution used in RAPGAP arises from our *a priori* ignorance of it. The input distribution is reweighted by $(\frac{1}{x_{IP}})^{\pm 0.1}$ corresponding to changes greater than can be constrained by the data. The resulting uncertainty on the measurement is $[0.4, 2.0, 3.5]$.

- The uncertainty on the β distribution used in RAPGAP arises from our *a priori* ignorance of it. The input distribution is reweighted by $\beta^{\pm 0.1}$ and $(1-\beta)^{\pm 0.1}$ resulting in an uncertainty on the measurement of $[0.8, 2.0, 3.7]$ and $[0.1, 2.4, 6.9]$ respectively. Again, the reweights are chosen to be larger than can be constrained by the data.

- The t dependence of the cross-section is parameterised as e^{Bt} where the parameter B used in RAPGAP is taken from a previous H1 measurement [48]. The input distribution is reweighted by $e^{\pm 2t}$ in order to reflect the uncertainty on the measured value of B resulting in an uncertainty on the measurement of $[0.05, 0.8, 5.3]$.

- The efficiency of the PRT is not well modelled by the simulation and a reweighting procedure was used (see section 3.2.2) to obtain a better description of the data. The systematic error is then estimated by applying 0.5 and 2 times the overall reweight factors used and results in an uncertainty on the measurement of $[0.0, 0.7, 1.9]$.

- The efficiency of the FMD is also not well modelled by the simulation and again a reweighting procedure was used (see section 3.2.1) to obtain a better description. The FMD efficiency is decreased by $\sim 10\%$ by this procedure and the systematic error is estimated by decreasing

the FMD efficiency by a further 10%. The resulting uncertainty on the measurement is $[0.0, 1.0, 4.9]$.

- The uncertainty on the energy scale of the PLUG calorimeter is 30% [63], resulting in an uncertainty on the measurement of $[0.0, 2.3, 5.3]$.

Sources of error on the measurement which are not correlated between bins are:

- The uncertainty on the efficiency of the NC triggers used is estimated from the variation of the inefficiencies of the individual subtriggers; the value used is 0.3% [13].

- There is a 0.5% uncertainty on the efficiency of the track-link requirement estimated from the remaining discrepancy between data and simulation [13].

- The uncertainty arising from the determination of the radiative and bin centre corrections is estimated by changing the kinematic distributions of RAPGAP and recalculating the corrections; the value used is 3% [80].

- An uncertainty of 0.5% on the electron identification efficiency is estimated by comparison of the cluster-based electron finder used to an independent track-based electron finder [13].

- The ratio of the proton-dissociation cross-section to the elastic proton cross-section, R_{PD}^{EL}, is varied between 0.5 and 2, corresponding to the limits set by previous measurements [76–78]. The resulting uncertainty on the measurement is 4.7%.

- The statistical uncertainty on the Acceptance correction leads to an uncertainty on the measurement of $[1.5, 5.0, 18.7]$.

4.4.1 Kinematic Reconstruction

The measurement should be independent of the kinematic reconstruction technique used. Shown in figures 4.9 and 4.10 are plots of the reduced cross-section as measured using the default reconstruction method given by equation 3.7 and the $e\Sigma$ method given in 3.6. No systematic differences are observed between the two reconstruction methods.

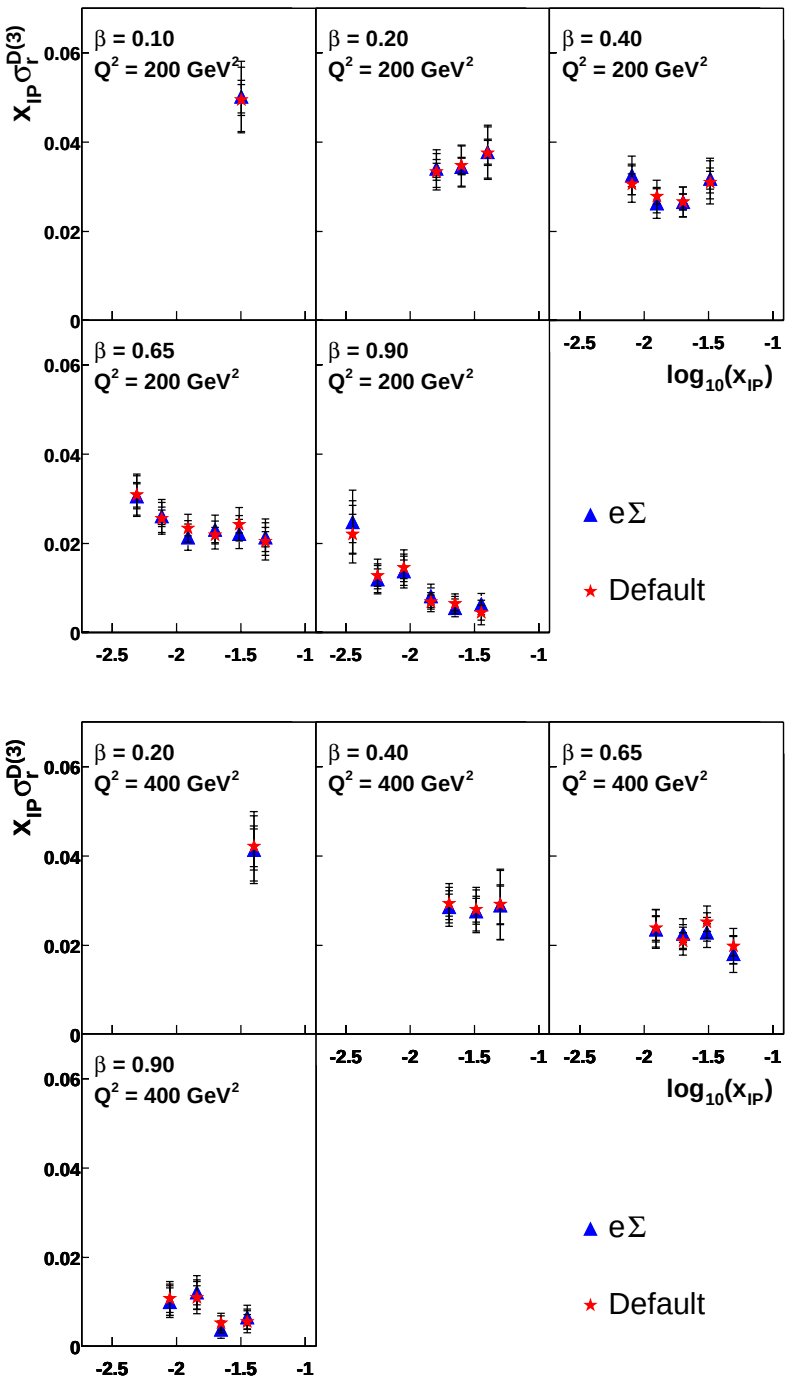

Figure 4.9: *The diffractive reduced cross-section $\sigma_r^{D(3)}$ multiplied by $x_{I\!P}$ as measured using the default kinematic reconstruction method and the $e\Sigma$ method. Inner error bars are statistical error alone, the outer error bars are the total statistical and systematic errors added in quadrature.*

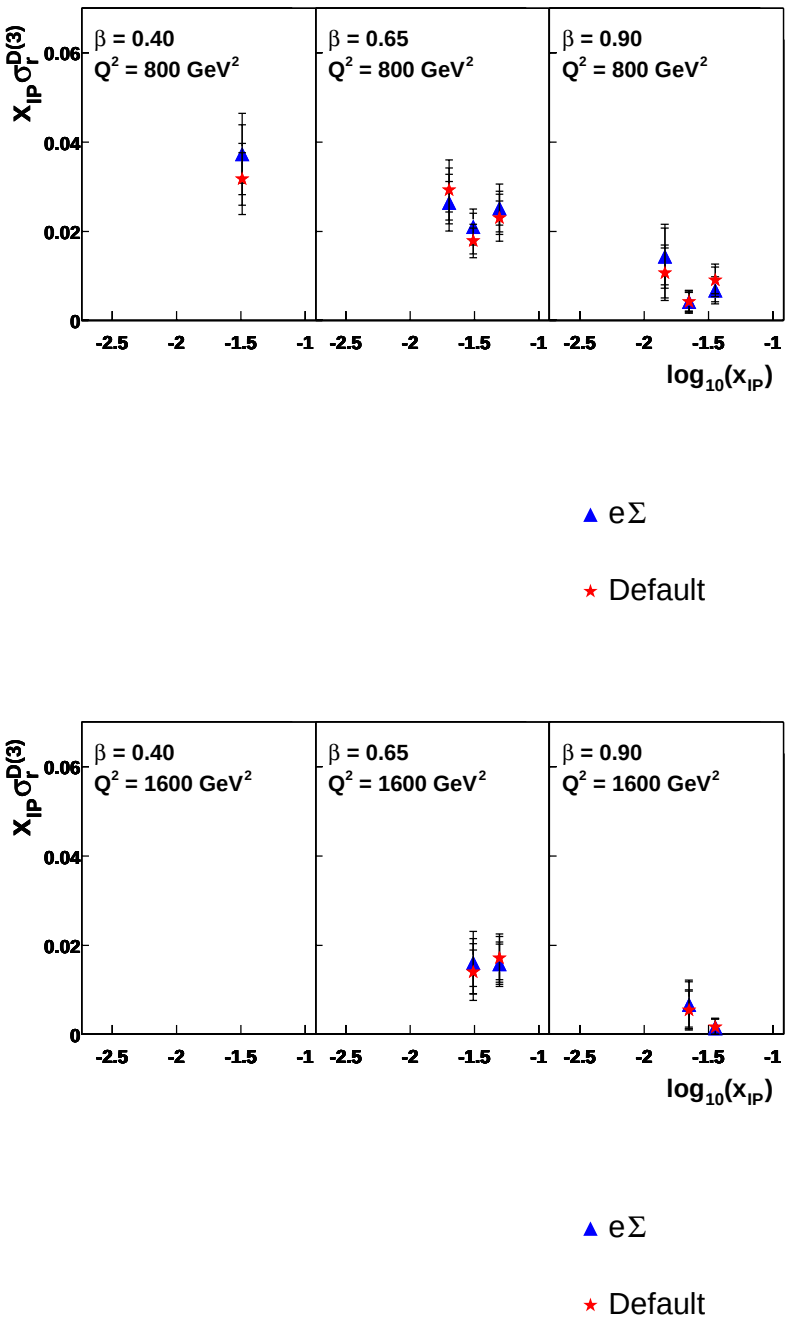

Figure 4.10: *The diffractive reduced cross-section $\sigma_r^{D(3)}$ multiplied by x_{IP} as measured using the default kinematic reconstruction method and the $e\Sigma$ method. Inner error bars are statistical error alone, the outer error bars are the total statistical and systematic errors added in quadrature.*

Chapter 5

Results and Interpretation

In this chapter the results of this analysis are presented in the form of the diffractive reduced cross-section $\sigma_r^{D(3)}$. The $x_{I\!P}$ dependence of the data is studied and the data are compared with the SCI and Semi-Classical models for diffraction introduced in sections 1.5.3 and 1.5.4, respectively. Two NLO DGLAP QCD fits [28,29] are compared to the data; the first fit, Fit 1, excludes the data presented in this analysis, the second fit, Fit 2, includes this data. A value for the effective Pomeron intercept $\alpha_{I\!P}(0)$ is extracted from Fit 2. Next the Q^2 and β dependencies of the data at fixed $x_{I\!P}$ are studied and finally, diffractive PDFs are extracted from both fits and compared. Tables of the cross-section results are presented in appendix A.

5.1 The Diffractive Reduced Cross-Section $\sigma_r^{D(3)}$

The diffractive reduced cross-section $\sigma_r^{D(3)}(x, Q^2, x_{I\!P})$ (multiplied by $x_{I\!P}$ to reduce the strong $x_{I\!P}$ dependence of the data) is shown as a function of $x_{I\!P}$ in bins of fixed β and Q^2 in figures 5.1 and 5.2 . The data are binned using the fixed β binning scheme (see section 4.1) allowing the $x_{I\!P}$ structure of the data to be studied. At low values of $x_{I\!P}$ the data are seen to rise as $x_{I\!P}$ decreases, consistent with the Pomeron trajectory. At the highest values of $x_{I\!P}$ there is the suggestion of an increase in the data as $x_{I\!P}$ increases which would be

indicative of the meson trajectory. As β increases the cross-section is clearly seen to decrease; there is no obvious dependence of the cross-section on Q^2.

5.2 Model Comparisons

Although the underlying mechanism behind diffraction is not theoretically understood several models of diffraction have been suggested. In this section the two models introduced in sections 1.5.3 and 1.5.4 are confronted with the data.

5.2.1 Soft Colour Interactions

Shown in figure 5.3 are two comparisons to the SCI model introduced in section 1.5.3. The dashed, black curve is the prediction of the original model, the solid, blue curve is the model incorporating the generalised area law. The original model is able to describe the data in the highest β bin at high x_{IP} but undershoots the data almost everywhere else. The model incorporating the generalised area law produces a much better overall description and is able to describe the data well everywhere except at the lowest β. In general the model has a slight tendency to overshoot the data at high β and undershoots the data at low β.

5.2.2 Semi-Classical Model

Shown in figure 5.4 is a comparison of the data to the Semi-Classical Model introduced in section 1.5.4. There is no attempt to model quark exchange, i.e. include a meson-like component, in this model and so the model is not expected to describe the data at high x_{IP}. At the lowest β the model produces a reasonable description of the data, but at higher β the prediction tends to undershoot the data. Of the 7 data points which satisfy the condition $x_{IP} < 0.01$ only one data point lies within one standard deviation of the prediction of the model; the other 6 data points all lie above the prediction of the model by significantly more than one standard deviation.

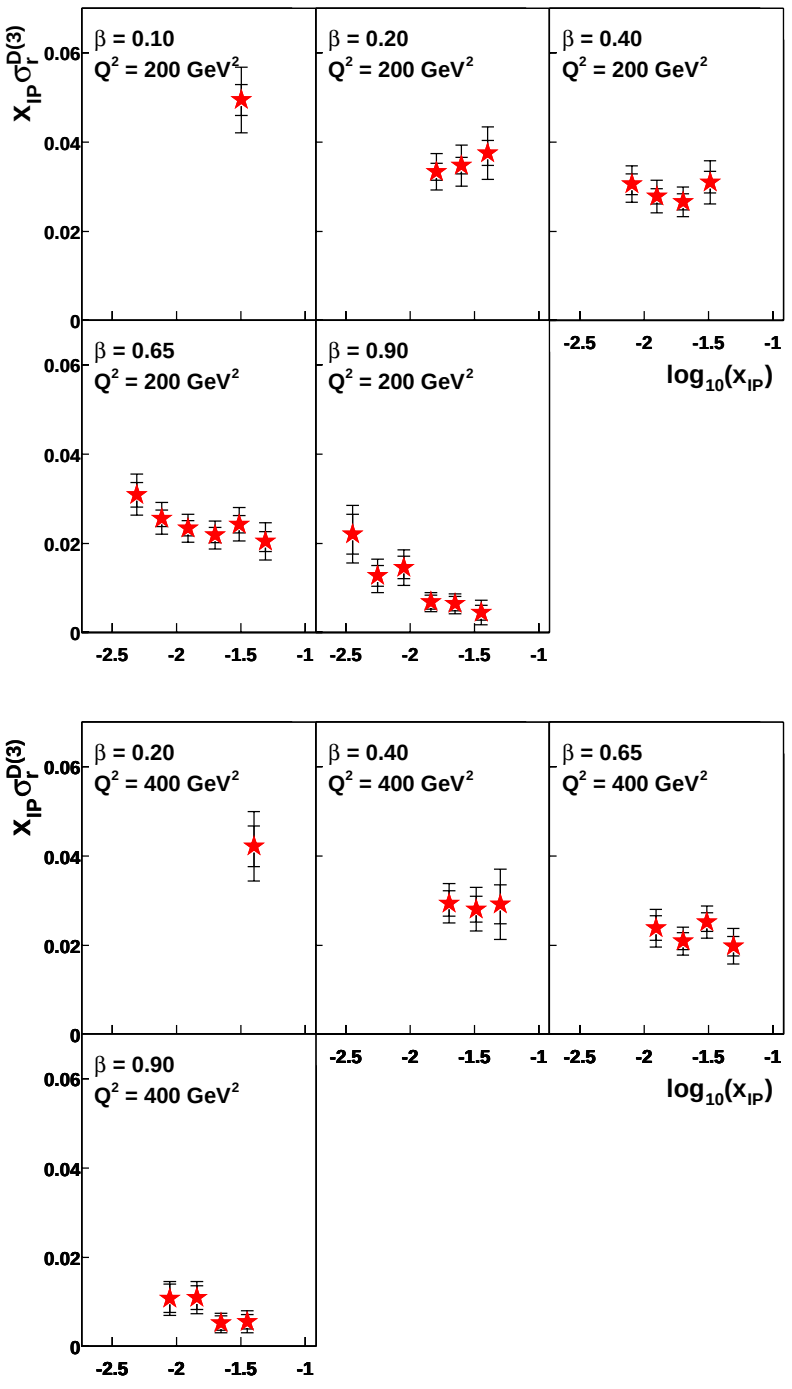

Figure 5.1: *The diffractive reduced cross-section* $\sigma_r^{D(3)}$ *multiplied by* x_{IP} *as a function of* $\log_{10} x_{IP}$ *in bins of fixed* β *and* Q^2 *for* $Q^2 = 200$ *and* 400 GeV^2. *Inner error bars are statistical errors alone, the outer error bars are the total statistical and systematic errors added in quadrature.*

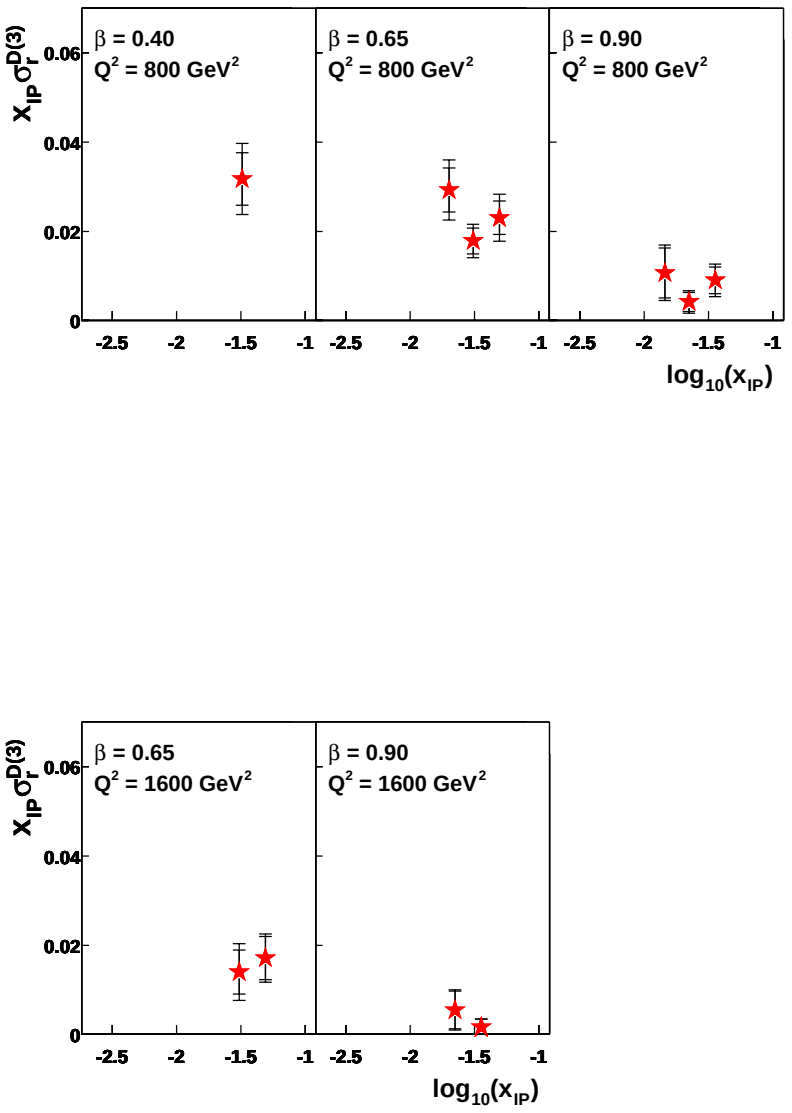

Figure 5.2: *The diffractive reduced cross-section* $\sigma_r^{D(3)}$ *multiplied by* x_{IP} *as a function of* $\log_{10} x_{IP}$ *in bins of fixed* β *and* Q^2 *for* $Q^2 = 800$ *and 1600* GeV^2. *Inner error bars are statistical errors alone, the outer error bars are the total statistical and systematic errors added in quadrature.*

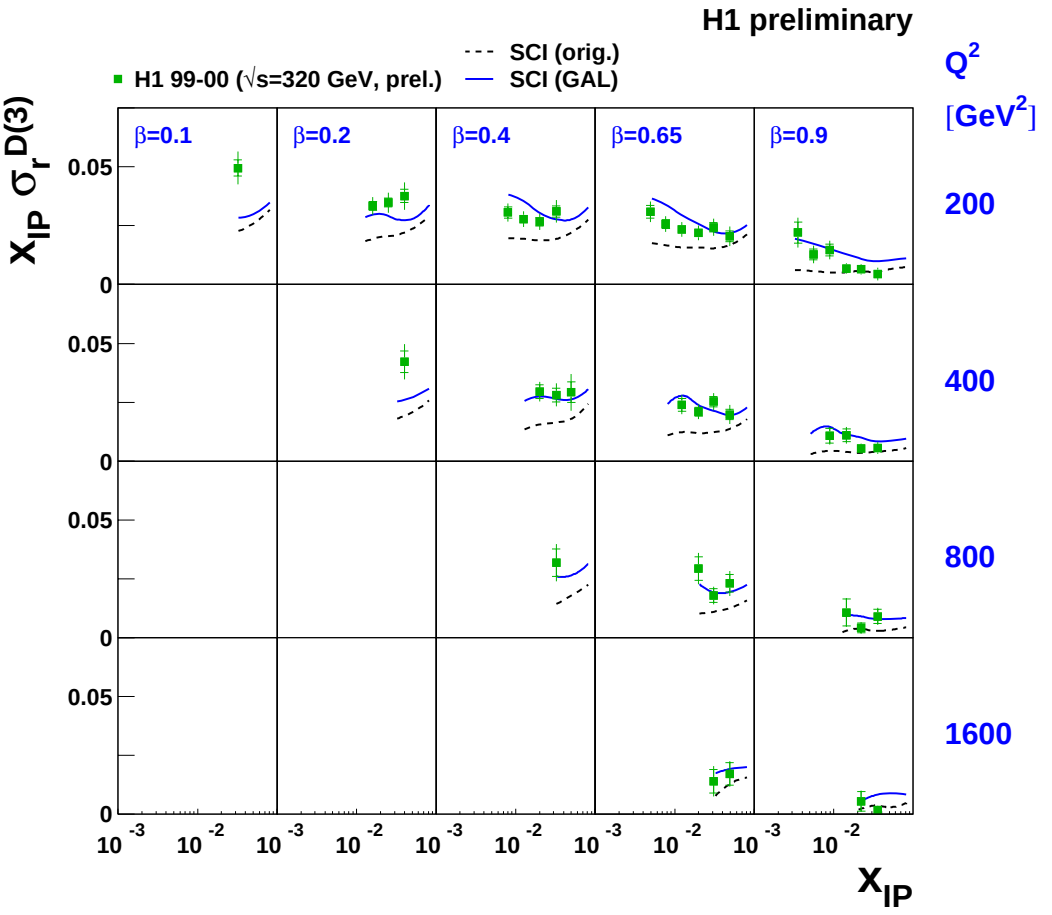

Figure 5.3: *The diffractive reduced cross-section $\sigma_r^{D(3)}$ multiplied by x_{IP} as a function of $\log_{10} x_{IP}$ in bins of fixed β and Q^2 as measured in this analysis (green points) compared to the original SCI Model (dashed black curve) and the SCI model incorporating the generalised area law (blue curve). Inner error bars are statistical errors alone, the outer error bars are the total statistical and systematic errors added in quadrature.*

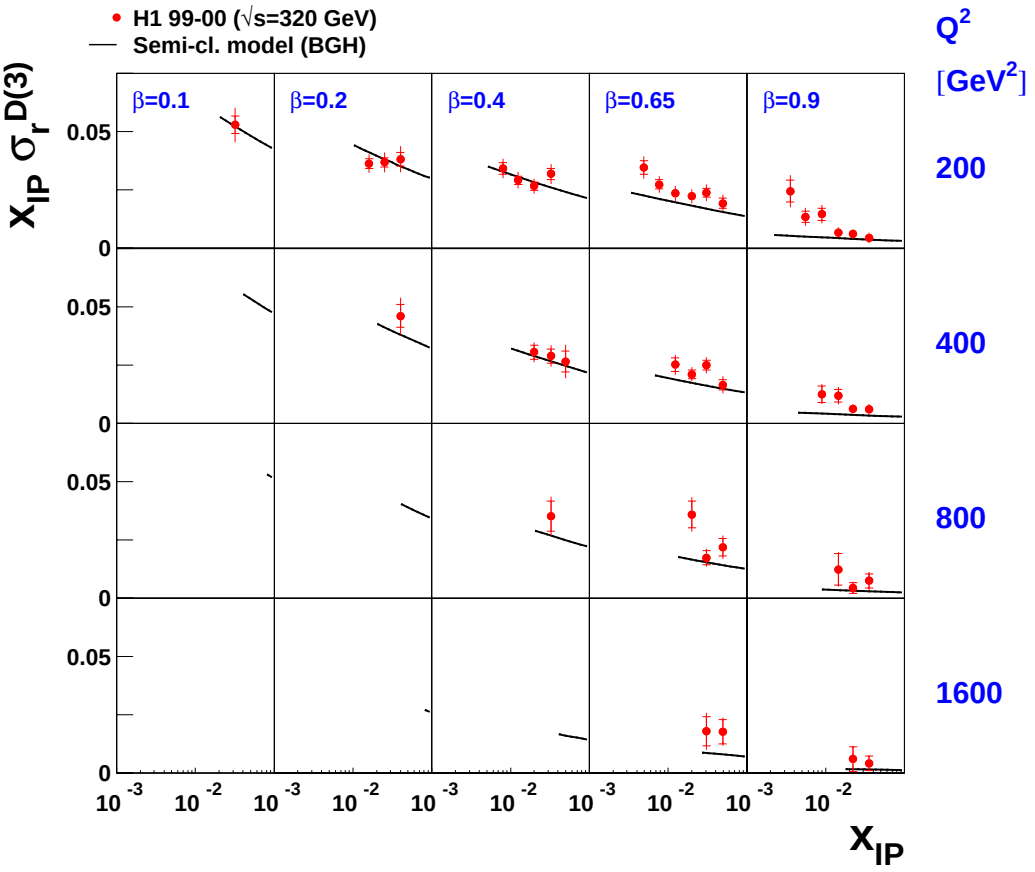

Figure 5.4: *The diffractive reduced cross-section $\sigma_r^{D(3)}$ multiplied by x_{IP} as a function of $\log_{10} x_{IP}$ in bins of fixed β and Q^2 as measured in this analysis (red points) compared to the Semi-Classical Model (black line). Inner error bars are statistical errors alone, the outer error bars are the total statistical and systematic errors added in quadrature.*

5.3 Comparisons with NLO QCD Fits and Previous Measurements

In this section the data are compared to two NLO QCD fits to the diffractive reduced cross-section. The first fit, Fit 1, is a fit made to lower Q^2 data and the high Q^2 data measured in a previous analysis [28, 29]. The second fit, Fit 2, uses the same lower Q^2 data set but replaces the previous high Q^2 data with the data presented in this analysis. Both fits are performed under the assumption of Regge factorisation, an assumption supported by the data.

5.3.1 Comparison of the Data with Fit 1

Figure 5.5 shows the data compared to Fit 1 which is made to data not including the data presented in this analysis. Also shown are the medium Q^2 data used in the fit and low Q^2 data (not used in the fit). The fit is seen to describe the data well across the full kinematic phase-space.

Figure 5.6 shows a comparison of this measurement with Fit 1 and a previous measurement using H1 data taken between 1994 and 1997 with an integrated luminosity of 35.6 pb^{-1} [75]; these data were used in the fit. The integrated luminosity of the data used in the analysis presented in this thesis is 63.0 pb^{-1}. This analysis extends the kinematic range in β, Q^2 and x_{IP} of diffractive measurements. In the region of overlap of the two measurements there is good agreement and no significant differences are seen. Fit 1 produces a good description of the data except at high β where the fit overshoots the data. Also shown is the Pomeron component of the fit, which clearly demonstrates the need for the inclusion of the sub-leading Reggeon component.

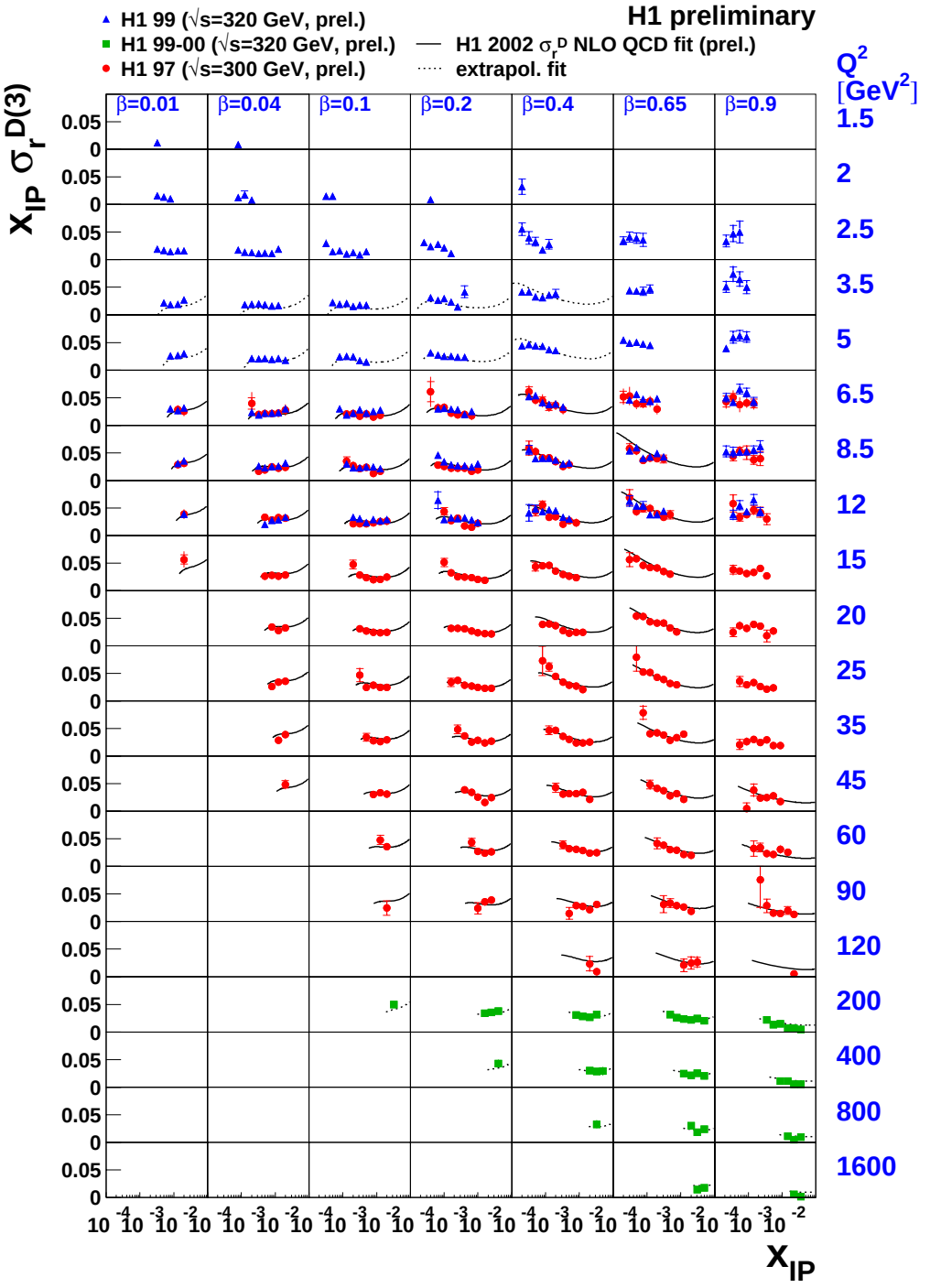

Figure 5.5: *The diffractive reduced cross-section $\sigma_r^{D(3)}$ multiplied by x_{IP} as a function of $\log_{10} x_{IP}$ in bins of fixed β and Q^2 as measured in this analysis (green points) and H1 analyses at medium Q^2 (red points) and low Q^2 (blue points). Also shown is a NLO QCD fit to H1 data (solid black curve), Fit 1 in the text, which includes the medium Q^2 data. Inner error bars are statistical errors alone, the outer error bars are the total statistical and systematic errors added in quadrature.*

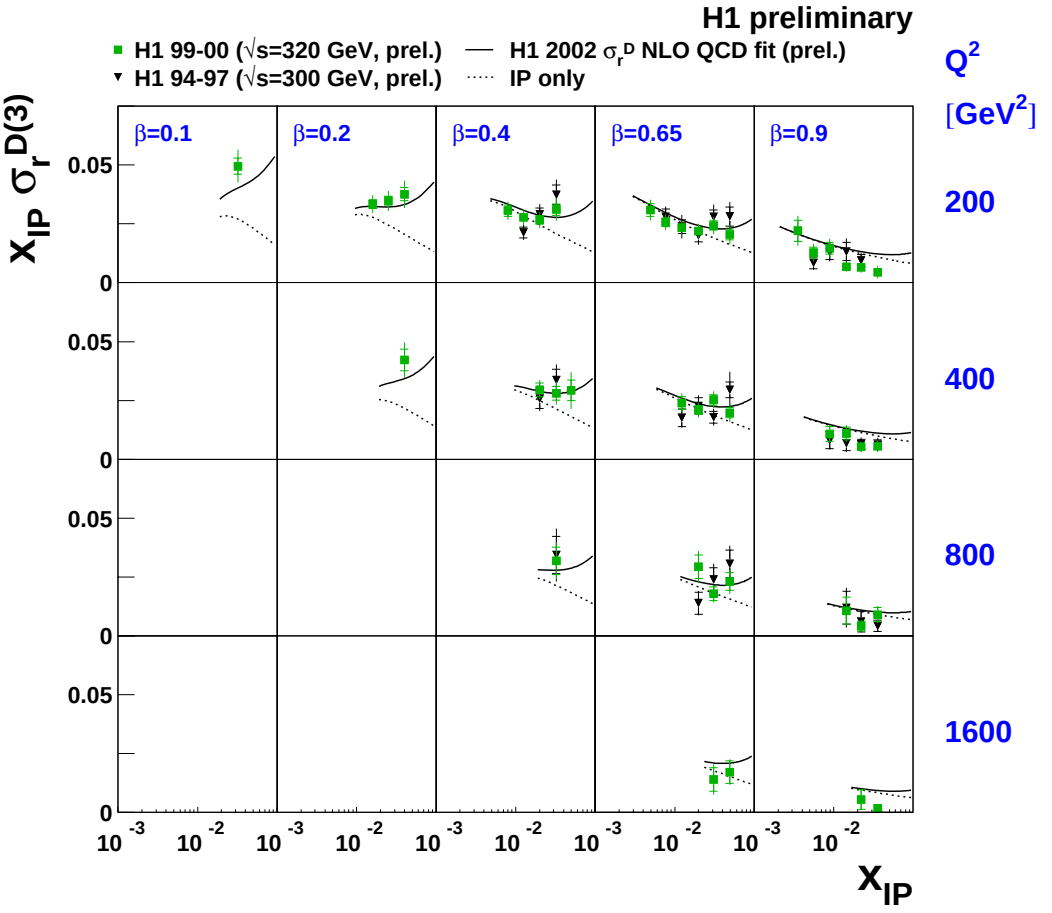

Figure 5.6: *The diffractive reduced cross-section $\sigma_r^{D(3)}$ multiplied by x_{IP} as a function of $\log_{10} x_{IP}$ in bins of fixed β and Q^2 as measured in this analysis (green points) compared to a NLO QCD fit to H1 data (solid black curve), Fit 1 in the text, and a previous measurement at high Q^2 used in the fit (black points). Also shown is the Pomeron component of the fit (dashed black line). Inner error bars are statistical errors alone, the outer error bars are the total statistical and systematic errors added in quadrature.*

5.3.2 Comparison of the Data with Fit 2

Figure 5.7 shows the data compared to Fit 2 which includes the data presented in this analysis (replacing the high Q^2 data measured in the previous analysis). The χ^2 per degree of freedom of the fit is very close to unity[1]:

$$\chi^2/dof = 325.6/324. \tag{5.1}$$

The new fit describes the data better at high β, although it does still overshoot the data, while retaining the good description at lower β. The effect of the fit on the data points is also shown in figure 5.7. At low β the fit is dominated by the lower Q^2 data, but at higher β the high Q^2 data of this analysis become more important. This is due to the constraint $M_X > 2$ GeV for all data points included in the fit in order to justify neglecting higher order effects not included in the fit. Also shown in the figure is the prediction of F_2^D from the fit, the effect of F_L^D on the fit can clearly be seen at high y.

5.3.3 Extraction of $\alpha_{IP}(0)$

The effective Pomeron intercept $\alpha_{IP}(0)$ is extracted from the data used in Fit 2 using the parameterisation given in equation 1.26 with flux factors parameterised according to equation 1.25. The value obtained is:

$$\alpha_{IP}(0) = 1.186 \pm 0.01 \tag{5.2}$$

which is consistent with previous H1 measurements [48]. This value is significantly above the value of ~ 1.08 obtained by Donnachie and Landshoff in their fit to pp and $p\bar{p}$ data [6].

5.3.4 Comparison of Lower Q^2 Data with Fit 2

Shown in figure 5.8 are the low Q^2 data included in Fit 2 compared to Fit 2. The fit describes the data very well across the measured kinematic range and

[1] The systematic errors of the data presented in this analysis are treated, as an exceptional case in the fit, as being fully correlated, which is a good approximation.

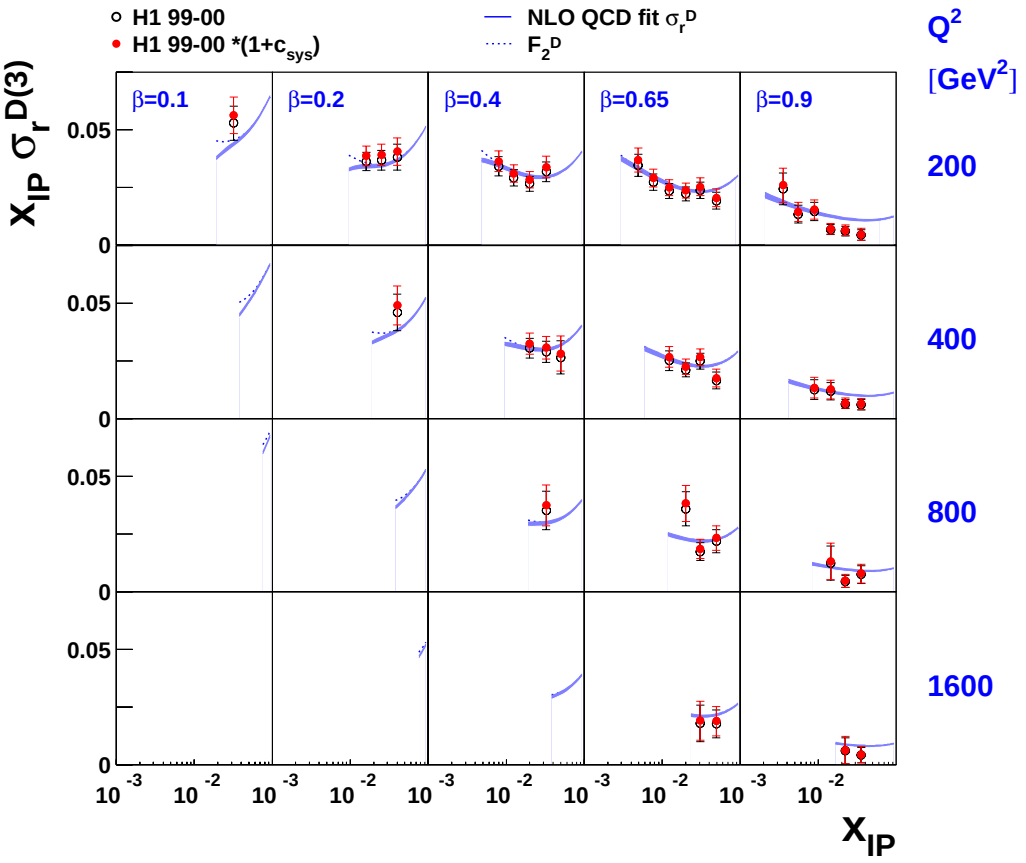

Figure 5.7: *The diffractive reduced cross-section $\sigma_r^{D(3)}$ multiplied by x_{IP} as a function of $\log_{10} x_{IP}$ in bins of fixed β and Q^2 as measured in this analysis (open points) compared to a NLO QCD fit to H1 data, Fit 2 in the text, which includes the data presented in this analysis (blue curve). The data points as shifted by the fit are also shown (solid red points) together with the prediction of F_2^D (dashed blue line). The error bars show the total statistical and systematic errors added in quadrature.*

the description at high β is improved.

5.3.5 The Q^2 Dependence of $\sigma_r^{D(3)}$

Shown in figures 5.9 and 5.10 is the diffractive reduced cross-section multiplied by x_{IP} as a function of Q^2 in bins of fixed β and x_{IP} compared to Fit 2. Also included in these figures are the medium Q^2 data used in the fit and the low Q^2 data not included in the fit. At the lowest β large positive scaling violations are seen in the data which persist until the largest measured value of β. These large scaling violations are indicative of a largely gluon-dominated structure. The scaling violations can be compared to the scaling violations of F_2 in figure 1.3. Scaling occurs at a fractional momentum $x \approx 0.13$ for the proton. In contrast scaling occurs at a fractional momentum $\beta \approx 0.66$ for diffractive exchanges.

5.3.6 The β Dependence of $\sigma_r^{D(3)}$

Shown in figures 5.11 and 5.12 is the diffractive reduced cross-section multiplied by x_{IP} as a function of β in bins of fixed Q^2 and x_{IP} compared to Fit 2. Also included in these figures are the medium Q^2 data used in the fit and the low Q^2 data not included in the fit. In the low x_{IP} bin the data are approximately flat as a function of β. In the high x_{IP} bin the data show a tendency to decrease with increasing β.

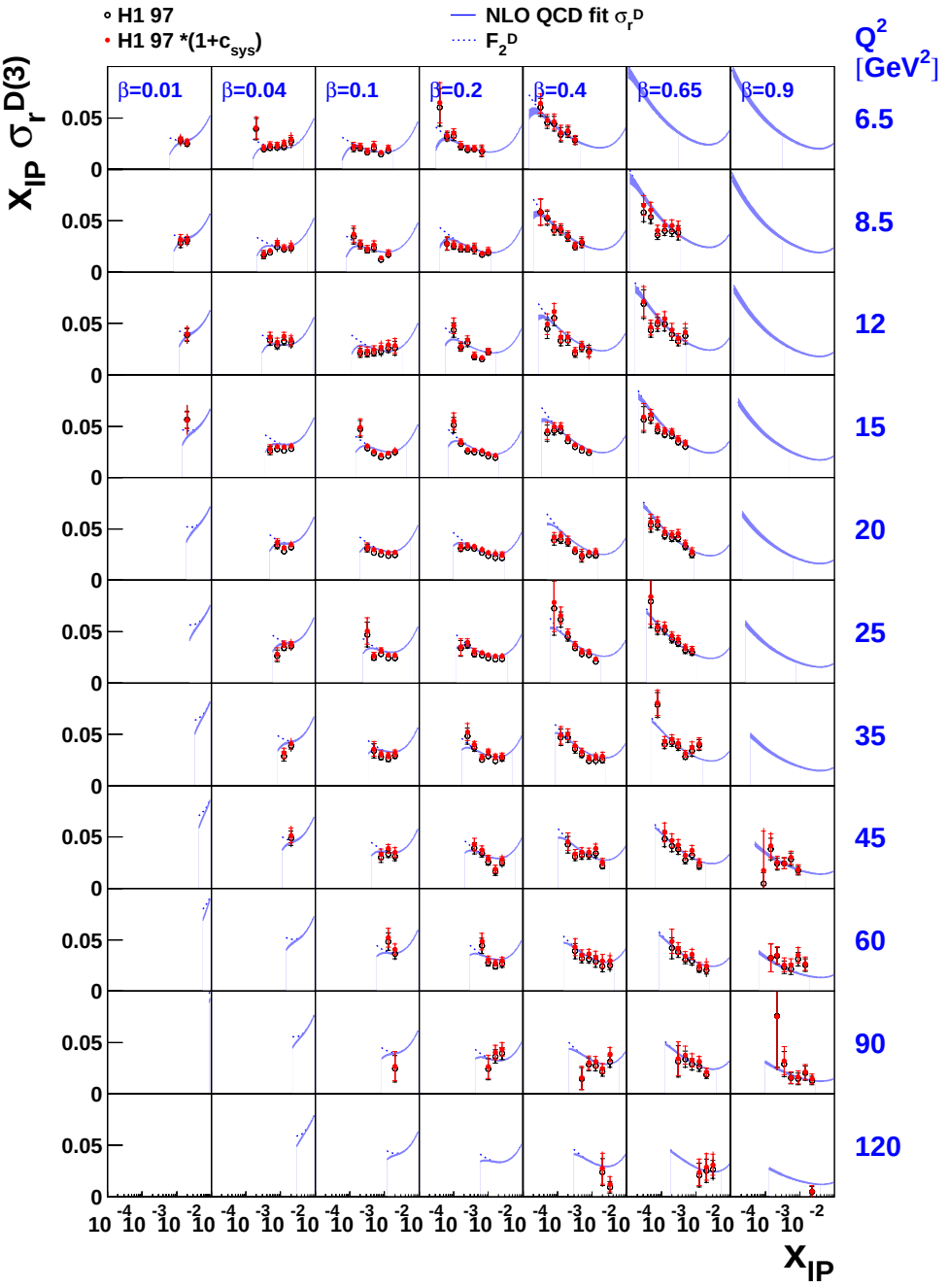

Figure 5.8: *The diffractive reduced cross-section $\sigma_r^{D(3)}$ multiplied by x_{IP} as a function of $\log_{10} x_{IP}$ in bins of fixed β and Q^2 as measured in a previous analysis using H1 data (red points) compared to the NLO QCD fit to H1 data, Fit 2 in the text, which includes that data and the data presented in this analysis (blue curve). The data points as shifted by the fit are also shown (solid red points). Inner error bars are statistical errors alone, the outer error bars are the total statistical and systematic errors added in quadrature.*

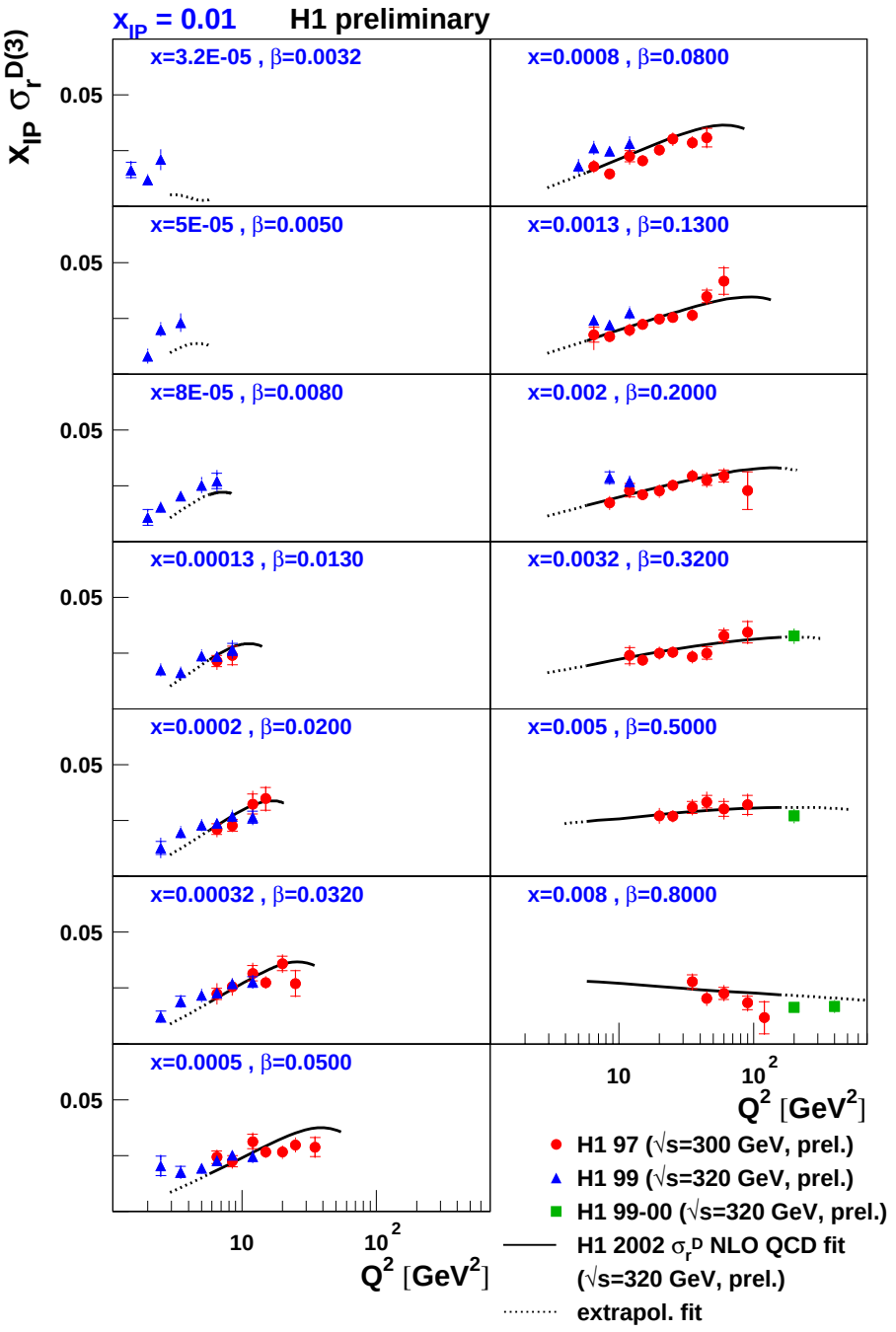

Figure 5.9: *The diffractive reduced cross-section $\sigma_r^{D(3)}$ multiplied by x_{IP} as a function of Q^2 in bins of fixed β and x_{IP} for $x_{IP} = 0.01$ as measured in this analysis (green points) and H1 analyses at medium Q^2 (red points) and low Q^2 (blue points). Also shown is a NLO QCD fit to H1 data (solid black curve), Fit 1 in the text, which includes the medium Q^2 data. Inner error bars are statistical errors alone, the outer error bars are the total statistical and systematic errors added in quadrature.*

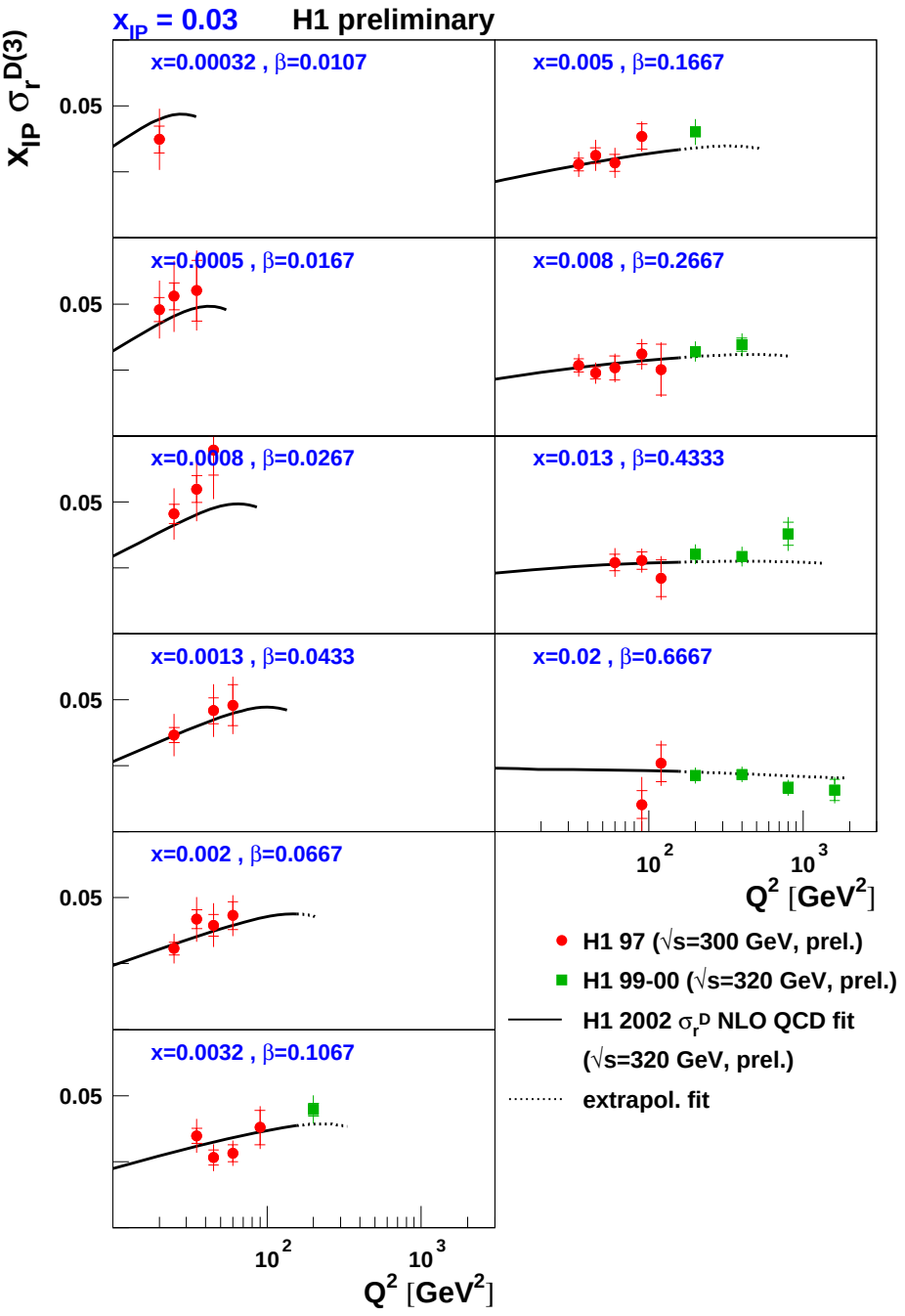

Figure 5.10: *The diffractive reduced cross-section $\sigma_r^{D(3)}$ multiplied by x_{IP} as a function of Q^2 in bins of fixed β and x_{IP} for $x_{IP} = 0.03$ as measured in this analysis (green points) and H1 analyses at medium Q^2 (red points) and low Q^2 (blue points). Also shown is a NLO QCD fit to H1 data (solid black curve), Fit 1 in the text, which includes the medium Q^2 data. Inner error bars are statistical errors alone, the outer error bars are the total statistical and systematic errors added in quadrature.*

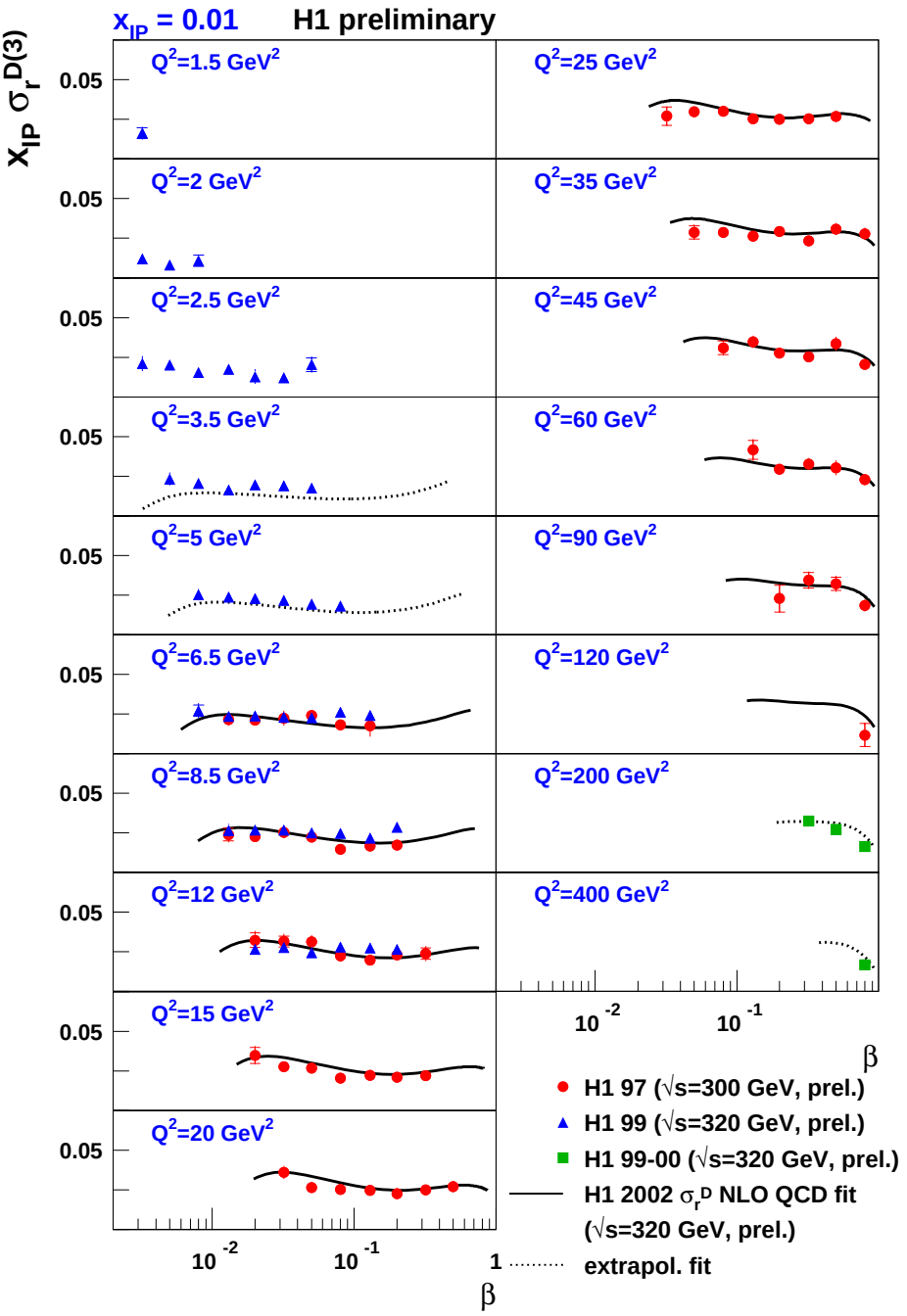

Figure 5.11: *The diffractive reduced cross-section $\sigma_r^{D(3)}$ multiplied by x_{IP} as a function of β in bins of fixed Q^2 and x_{IP} for $x_{IP} = 0.01$ as measured in this analysis (green points) and H1 analyses at medium Q^2 (red points) and low Q^2 (blue points). Also shown is a NLO QCD fit to H1 data (solid black curve), Fit 1 in the text, which includes the medium Q^2 data. Inner error bars are statistical errors alone, the outer error bars are the total statistical and systematic errors added in quadrature.*

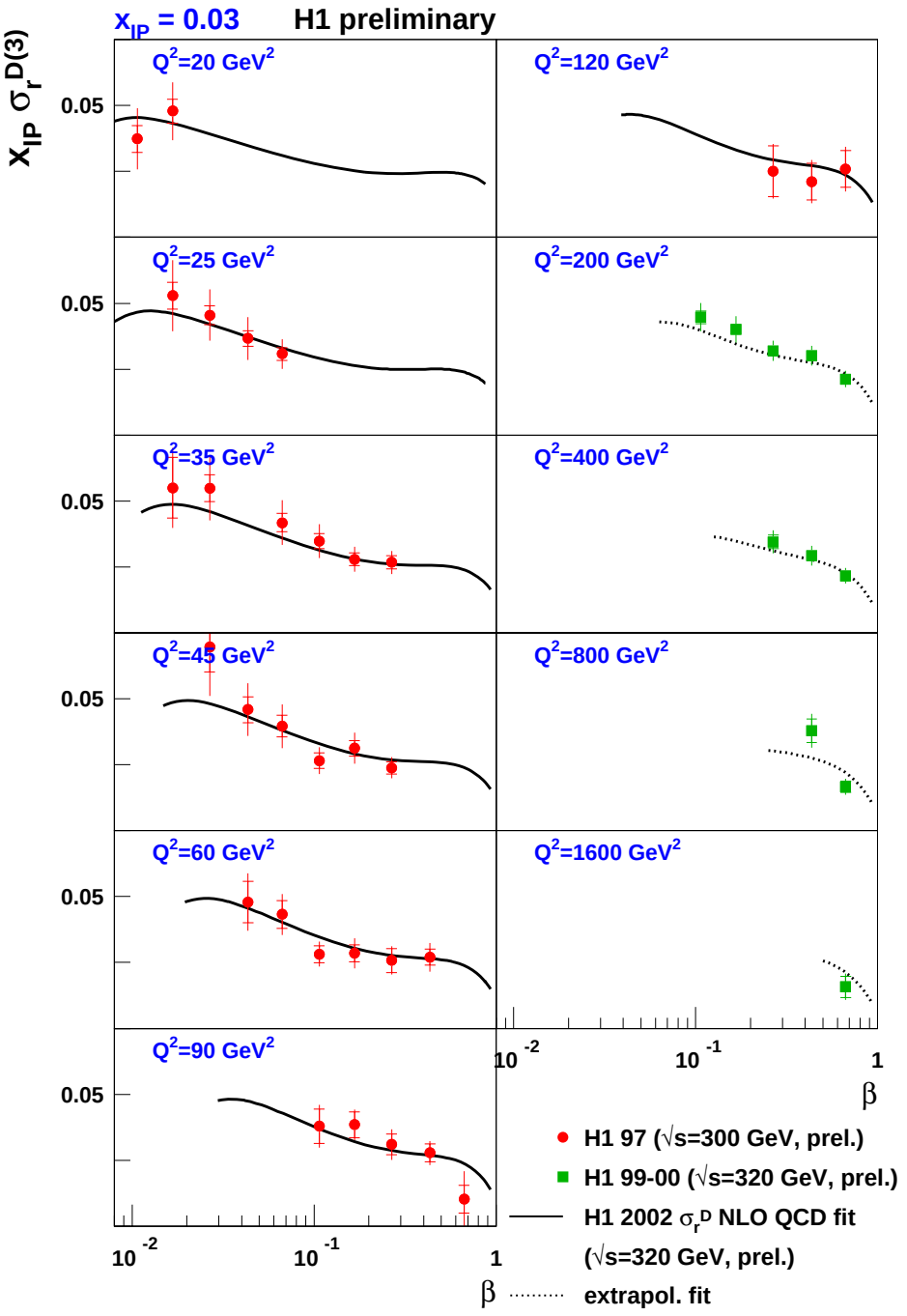

Figure 5.12: *The diffractive reduced cross-section $\sigma_r^{D(3)}$ multiplied by x_{IP} as a function of β in bins of fixed Q^2 and x_{IP} for $x_{IP} = 0.03$ as measured in this analysis (green points) and H1 analyses at medium Q^2 (red points) and low Q^2 (blue points). Also shown is a NLO QCD fit to H1 data (solid black curve), Fit 1 in the text, which includes the medium Q^2 data. Inner error bars are statistical errors alone, the outer error bars are the total statistical and systematic errors added in quadrature.*

5.3.7 Diffractive Parton Densities

Following the NLO QCD fit to the data it is possible to extract PDFs interpretable within the resolved Pomeron model as being the parton density functions of an object with the quantum numbers of the vacuum, i.e. the Pomeron. Furthermore, using the strategy given in [28, 29] it is possible to extract the uncertainties on these PDFs. Both a singlet distribution $\Sigma(z, Q_0^2)$ and a gluon distribution $g(z, Q_0^2)$ are included in the fits, where the singlet distribution assumes $u = d = s = \bar{u} = \bar{d} = \bar{s}$ and the starting scale used is $Q_0^2 = 3$ GeV^2. Figures 5.13 and 5.14 show the PDFs at NLO from Fit 1 and Fit 2 as a function of z on a linear and log scale respectively, where z is the fractional momentum of the parton within the diffractive exchange with respect to the diffractive exchange.

The gluon density is seen to dominate the structure of the diffractive exchange in both fits at all Q^2. Fit 2 produces a substantially more gluon dominated structure than Fit 1.

5.4 Summary and Outlook

A new measurement of inclusive diffractive DIS at high Q^2 has been presented which extends the previous kinematic phase-space significantly and increases the statistical significance of the data. The data have been shown to be well understood with both the inclusive DIS sample and the diffractive DIS sample being well described by Monte Carlo simulations. All systematic effects have been accounted for and the Monte Carlo simulations corrected to describe the data where appropriate.

The diffractive reduced cross-section $\sigma_r^{D(3)}(x, Q^2, x_{IP})$ was extracted from the data in the kinematic range ($Q^2 > 130$ GeV^2, $0.07 < \beta < 1.0$ and $0.005 < x_{IP} \leq 0.05$) and found to be consistent with previous measurements using the H1 detector. The x_{IP} dependence of the data was studied and a value of $\alpha_{IP}(0)$ was extracted using a Regge parameterisation of the data. The value of $\alpha_{IP}(0)$

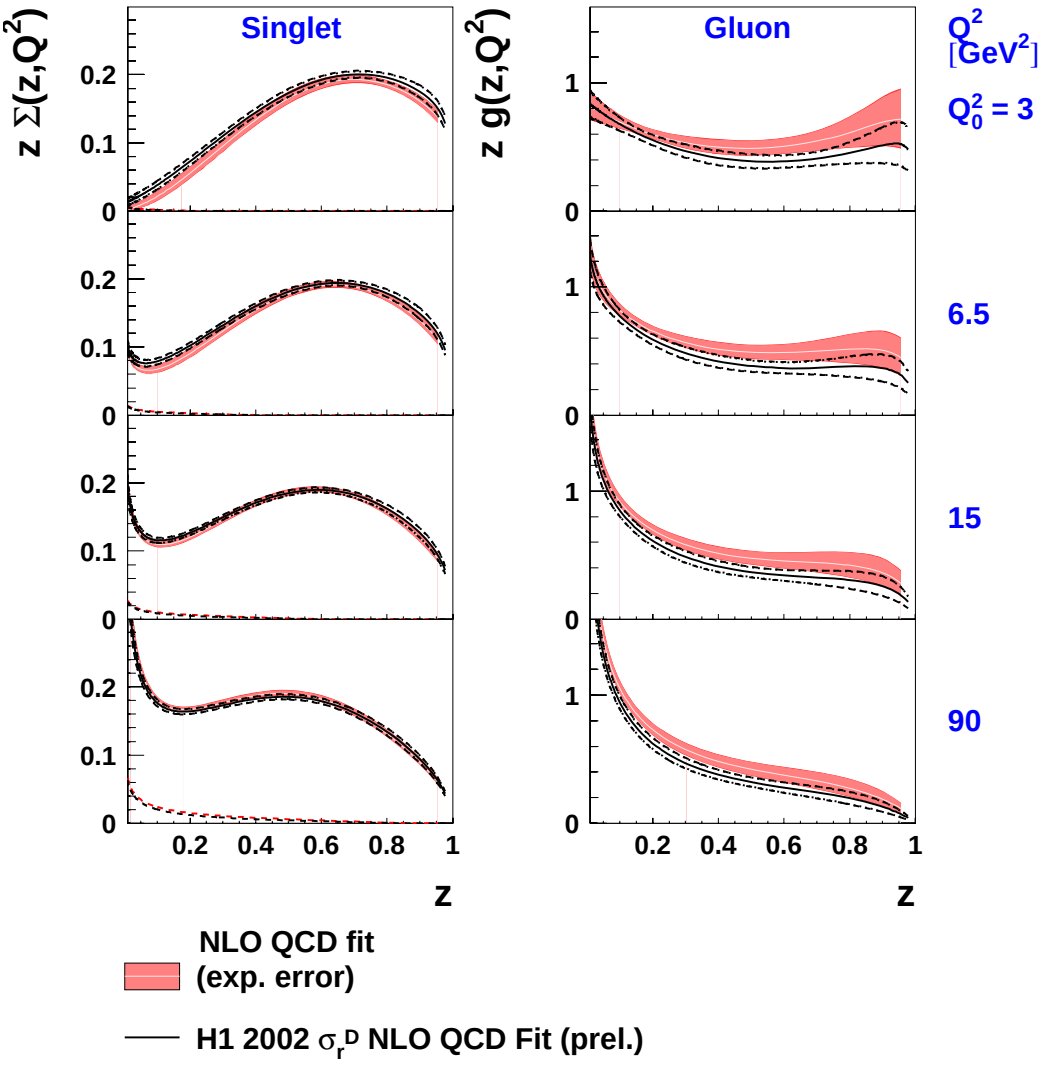

Figure 5.13: *The diffractive quark singlet and gluon density functions as a function of z as extracted from two NLO QCD fits; Fit 1 (black curves) and Fit 2 (pink curves). The bands show the experimental error.*

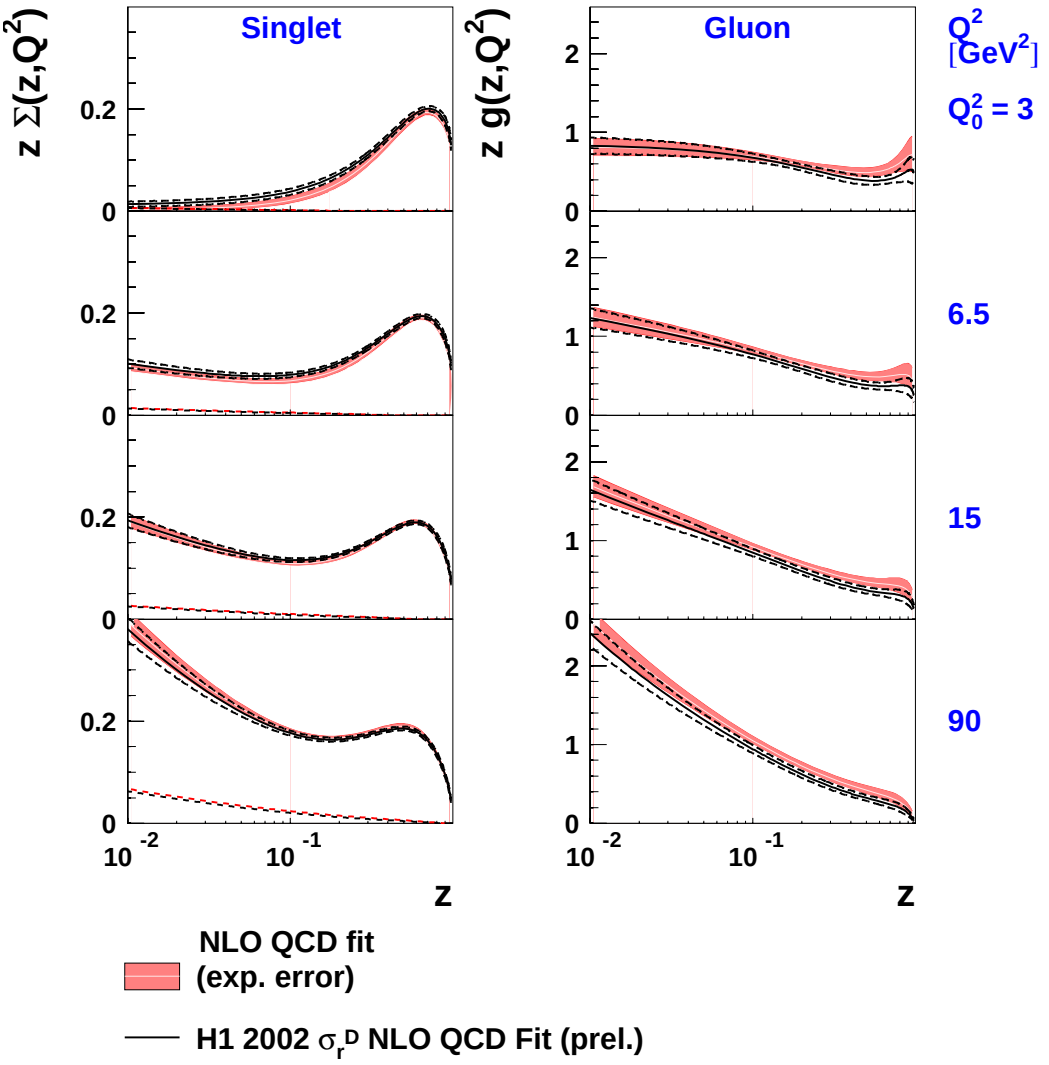

Figure 5.14: *The diffractive quark singlet and gluon density functions as a function of* $\log z$ *as extracted from two NLO QCD fit; Fit 1 (black curves) and Fit 2 (pink curves). The bands show the experimental error.*

extracted is consistent with previous measurements and is significantly larger than that of the soft Pomeron of hadronic physics. The data are consistent with a Pomeron dominated exchange at low values of $x_{I\!P}$ with a non-negligible meson contribution at higher values of $x_{I\!P}$.

Several models of diffraction were confronted with the data. The Semi-Classical model is found to produce a reasonable description of the data at low β but undershoots the data at higher β. The original SCI model is found to be able to describe the data in the highest β bin at high $x_{I\!P}$. The SCI model which incorporates a generalised area law is found to produce a good description of the data except at the lowest β.

Following the proof of QCD hard scattering factorisation for diffraction [8] the data were also studied within the framework of QCD by using a binning scheme which fixes $x_{I\!P}$. This allows the Regge factorisation hypothesis to be tested, the Q^2 and β dependencies to be studied and a NLO QCD fit to be performed. The Q^2 dependence of the data show large positive scaling violations persisting out to large values of $\beta \sim \frac{2}{3}$, consistent with the gluon dominated structure seen in previous analyses. The large gluon density is seen to persist out to the largest fractional momenta. NLO QCD fits to the data are able to describe the data well and the extracted PDFs are dominated by a large gluon contribution across the full measured phase-space. The NLO QCD fit which includes the data presented in this analysis produces a more gluon-dominated structure than the previous fit, although the fits are consistent with each other.

The Regge factorisation hypothesis implies the concept of a resolvable Pomeron in diffractive processes at HERA. The NLO QCD fits to the data demonstrate that this is a good approximation, at least at HERA, of whatever the underlying process is. More data will be needed to test the extent of the validity of the Regge factorisation approximation, to extract more accurate diffractive PDFs and to uncover the true nature of this intriguing phenomenon.

5.4.1 Improvements and Future Work

There are several areas in which improvements could be made to the current analysis.

- Combining the 1994-1997 data period would increase the integrated luminosity by ≈ 50 %, yielding an increase in the statistical significance of the data.
- Incorporating proton dissociation into the RAPGAP Monte Carlo would decrease the corresponding systematic uncertainties.
- The simulated description of the Forward Detectors of H1 is quite poor and an improved understanding of these detectors would reduce the associated systematic uncertainties.
- The uncertainty on the amount of energy due to noise in the LAC is 25% and leads to a large systematic uncertainty which could be reduced.

Improvements of the generic OO analysis framework used to perform this analysis are discussed in section 6.3.9.

Chapter 6

Object Oriented Techniques Used in Offline Physics Analysis

In this chapter the generic Object-Oriented (OO) analysis framework used to perform the analysis presented in this thesis is described. Firstly the principles of OO programming are introduced along with the applicability of these principles to physics analysis. The OO data-storage and analysis framework of H1 is briefly introduced with emphasis on those elements of the framework relevant to analysis. Next, physics analysis is abstracted into a series of generic tasks which are identified with analysis-level objects; these objects can be organised into the generic analysis framework presented here. Finally, a discussion of future work to improve the generic analysis framework is presented.

6.1 Introduction

One of the founding principles behind OO programming philosophy is the finding that humans have a surprisingly small short-term memory and are only capable of processing 7 ± 2 pieces of information at once [81]. This is a crucial limitation in man's ability to deal with complex systems, an example of which is a software framework used to perform physics analysis. If there is no structure to the system then a step by step or binomial search approach is

likely to be the best means of solving problems within the system.

6.1.1 Chunking and Modularisation

Although humans are only capable of processing 7 ± 2 pieces of information at once this limitation does not seem to depend on the complexity of the piece of information. For example, an average human can process as many words as he/she can letters. Chunking information, like forming words from letters, increases the total amount of information that can be processed.

If the individual information within a software system can be organised into chunks of information, henceforth referred to as modules, then each piece of information in the system can be bigger. 7 ± 2 pieces of information will then represent a larger fraction of the system as a whole. Modules can also be arranged into larger, composite modules and so the modularisation process can be re-iterated until the system is composed of < 7 modules. However, if the modules cannot be treated independently of one another then the modularisation procedure does not significantly reduce the complexity of the system.

6.1.2 Object-Orientation

Object-Orientation takes the modularisation process one step further. In an OO system each module is also entirely responsible for its data. These empowered modules, or objects, must themselves be able to supply any and all information about the data they contain. All access to the object's data is through the object's interface allowing the object itself to maintain its integrity. The contents of the object are thus decoupled from the system; the system now comprises of < 7 independent, possibly composite, objects which can only deal with each other through well-defined interfaces and as a result the complexity of the system is significantly reduced.

Abstraction

An abstraction is the list of methods, or *member functions* in C++, which defines what an object can and must do. For example, a "Mode of Transport" `ModeOfTransport`[1] may be defined as something which transports a "Paying Customer" `PayingCustomer` from one specified "Place" `Place` to another. It must therefore provide a `Transport` member function which allows a `PayingCustomer` to be transported from one `Place` to another.

```
ModeOfTransport vehicle;
PayingCustomer customer;
Place fromA, toB;

vehicle.Transport(customer, fromA, toB);
```

Specialisation and Inheritance

Different sorts of the same abstraction can behave in different ways. `Train`, `Bus` and `Taxi` are all a `ModeOfTransport`. They are specialisations of the original abstraction and in the C++ programming language this relationship is expressed through inheritance; `Train`, `Bus` and `Taxi` all inherit the `ModeOfTransport` interface. They will each perform the `Transport` request for a `PayingCustomer`, each one performing the request slightly differently, but how they do it is not important. Of course, the `PayingCustomer` may find that the amount that he is requested to pay via his `Pay` member function varies greatly, but the `ModeOfTransport` has transported the `PayingCustomer` as he said he would according to his interface and now the `PayingCustomer` must respect his interface and pay. The interface defines what an object must do and both `ModeOfTransport` and `PayingCustomer` objects must strictly adhere to their respective interfaces.

[1]Here the notation used is that a concept is given in quotation marks followed by the name of the abstraction in `this font-type`.

Encapsulation

The member functions that an object provides to other objects are called *public* member functions and define the interface to the object, i.e. *what* the object will do, but *how* an object performs a particular task and *how* it maintains its own state, i.e. via its *data members*, are *private* information. Encapsulation is this separation of an object's interface from its implementation. The `Train`, `Bus` and `Taxi` are all a `ModeOfTransport` each differing in how they transport a `PayingCustomer`. They could also differ in their physical states, although there may be some similarities. The important thing is that the `PayingCustomer` shouldn't have to and indeed doesn't have to care about these details. If `Bus`es and `Train`s find a way of running to schedule the `PayingCustomer` still requests to be transported in exactly the same way as before (although he may find that the amount he pays varies again). Changes made to an objects algorithms and state are *internal* and because of encapsulation these changes cannot affect other objects.

6.1.3 Classes and Objects

Classes are generally the means by which OO computing languages define an object's state and interface. In the trivial example below a class `Circle` is defined in C++, with a rather restricted (and not very useful) interface.

```
class Circle{
public:
  Circle()                {fRadius = 1.0;}
  Circle(double radius)   {fRadius = radius;}
  ~Circle()               {}
  double GetRadius()      {return fRadius;}
private:
  double fRadius;
};
```

`Circle` is little more than a data-storage object as it stands and it would be far more efficient to simply use the `double` already provided. To be a complete `Circle` object it must at least have member functions like

```
double GetDiameter();
double GetArea();
double GetCircumference();
```

as well as some functionality which allows a client to manipulate the `Circle` object, e.g.

```
void SetRadius();
void SetDiameter();
void SetArea();
void SetCircumference();
```

6.1.4 A Code Comparison - The 4-vector

A 4-vector is a familiar concept in physics and the components of a 4-vector, for example p_x, p_y, p_z and E, appear frequently in physics analysis software. In an OO programming scheme the components of the 4-vector are collected together into one object which will be referred to here as the `4Vector` object[2]. The `4Vector` object is responsible for its own information and can therefore ensure its own self-consistency. If the 4-vector needs to be changed in some way then the `4Vector` object is responsible for ensuring that it is changed consistently and correctly. In the example below the task set is that a 4-vector is first made, then scaled by a factor of 2.0 (for example in the case of a calibration) and finally the polar angle of the 4-vector is shifted by 2 mrad (for example in the case of studying the effect of a systematic uncertainty on the angular position of a detected particle). On the left is a possible solution in C, on the right is a solution using a `4Vector` object.

[2]The concept of the 4-vector is so familiar in fact that several `4Vector` classes exist, albeit with different names. The ROOT [82] `4Vector` class is called `TLorentzVector`.

C

```
// Initialisation

double px = 1.0;
double py = 1.0;
double pz = 1.0;
double e = 1.0;

// Scale the 4-vector

px *= 2.0;
py *= 2.0;
pz *= 2.0;
e *= 2.0;

// Add 2 mrad to theta preserving the magnitude of the vector

double p = sqrt((px*px)+(py*py)+(pz*pz));
double pt = sqrt((px*px) + (py*py));
double theta = atan2(pt, pz);
theta += 0.002;
double phi = atan2(py, px);

px = p*sin(theta)*cos(phi);
py = p*sin(theta)*sin(phi);
pz = p*cos(theta);
```

C++

```
double px = 1.0;
double py = 1.0;
double pz = 1.0;
double e = 1.0;
4Vector victor(px, py, pz, e);

victor *= 2.0;

double theta = victor.GetTheta();
theta += 0.002;
victor.SetTheta(theta);
```

Of course the calculations are fairly trivial[3] and if this were a standalone, once-and-once-only task that needed to be done then it would be far more efficient to write the code on the left rather than write the `4Vector` class. However, this calculation and very many others like it are required time and time again when dealing with and manipulating 4-vectors. In the OO scheme all useful manipulations are defined *once* in a `4Vector` class and all `4Vector` objects manipulate themselves using that singular definition[4].

The important thing to note is that `victor` is not only a means of data-storage, he also controls *all* access to his data, thus he is able to ensure that his data is always self-consistent; a client of `victor` is not allowed to be in a position to get something wrong. Note too that `victor` is created as a Cartesian 4-vector but has no problem in dealing with spherical polar representations of himself. The author of the `4Vector` class is perfectly at liberty to change the way in which a `4Vector` stores its state or the way in which it performs calculations, for example to optimise performance, without fear of affecting any `4Vector` clients.

6.2 OO Techniques Applied to Physics Analysis Software

Despite the diversity of techniques that must be employed to perform physics analysis there remain many similarities between the tasks which need to be done. OO programming provides a natural way to exploit these similarities.

[3]Although there are several common bugs possible, for example, in which order should the arguments be given to atan2?

[4]Thus, if the arguments to atan2 are given in the incorrect order the programmer need only look in one place to correct the bug. Once the definition is corrected then every `4Vector` object benefits.

6.2.1 The H1 OO Project

The H1OO Project [83] is the new combined data storage and physics analysis framework for H1. The aims of this project can be summarised as

- Use OO paradigms to organise and centralise the physics analysis software.
- Use the best understanding of the H1 detector and physics analysis algorithms in all physics analyses and build on this expert knowledge.
- Use one tool for data storage and physics analysis.

The H1OO framework is based on ROOT [82] which provides a means of storing objects persistently as well as a series of packages aimed specifically for physics analysis. The old and new data storage schemes are shown in 6.1. Both schemes share the same input level which is the Production Output Tape (POT). In the old scheme this POT information is used to create the Data Summary Tape (DST) which is then used in turn to create, generally using private FORTRAN code, a reduced set of information for each event (an ntuple); this is then analysed using PAW [84].

In the new scheme the POT information is used to create the Object Data Storage (ODS) layer which is equivalent to the DST information. The ODS consists of reconstructed tracks, clusters and detector-level information, but this information is stored in the form of objects, for example `H1Track` and `H1Cluster` objects. The next layer of information is the *micro* ODS (μODS) and contains identified particle objects reconstructed from the ODS information, for example `H1PartMuon` objects are the reconstructed muons from the event. The final layer of information is the H1 Analysis Tag (HAT) layer which is a concise event summary, for example it contains the number of muons found in the event. Any combination of the ODS, μODS and HAT layers can be analysed using ROOT combined with the H1OO framework.

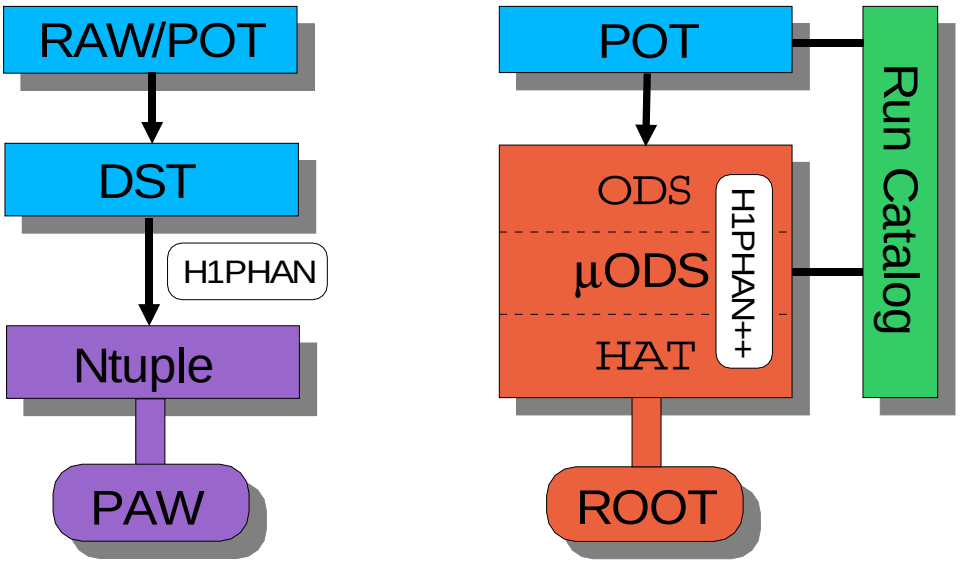

Figure 6.1: *A schematic view of the old (left) and new (right) data storage and analysis schemes of H1.*

The H1OO framework also provides a means of *steering* objects via the H1Steering package [85]. Steering here is used to mean dynamically changing the state of an object without having to recompile code. The initial state attributes of an object can be specified in a simple ACSCII text file, the H1Steering mechanism then uses ROOT's run-time type information mechanism to set the object's attributes to the specified values.

The Hybrid Mechanism

The analysis presented in this thesis uses a hybrid mechanism to produce μODS and HAT files from existing FORTRAN code which are then analysed using a combination of ROOT and the H1OO framework. This mechanism allows the structure of the code to be checked independently of new physics algorithms and the results obtained are directly comparable with existing results made using the old scheme. The H1OO framework is continuously developing and the version used for this thesis is 2.2.13.

6.3 A Generic OO Analysis Framework

The aim of the following is firstly to identify the generic tasks which need to be performed in an analysis and then to relate these tasks to objects.

6.3.1 Generic Analysis Tasks

Figure 6.2 shows a flow diagram of a typical analysis scenario.

1. Initialisation, steering and control of the analysis is done.
2. A set of files is loaded, data or simulation.
3. For each event in the file:
    - Variables are read in from the files;
    - More variables are calculated from that information;
    - An event selection is performed;
    - If the event passes the selection some histograms are filled;
    - The event is binned.
4. If there is another set of files goto 2.
5. Calculations of *Acceptance*, *Purity* and *Stability*, etc. are done.
6. The final measurement is made.

Binning an event here refers to the process of finding the reconstructed (REC) level and generator (GEN) level bins for an event and studying them according to the method detailed in section 4.3.1, where the definitions of *Acceptance*, *Purity* and *Stability* can also be found.

One abstraction which presents itself immediately on inspection of this list is the `Event` object. This object is necessary in order to ensure that there is one coherent and consistent representation of the event. This object will be the

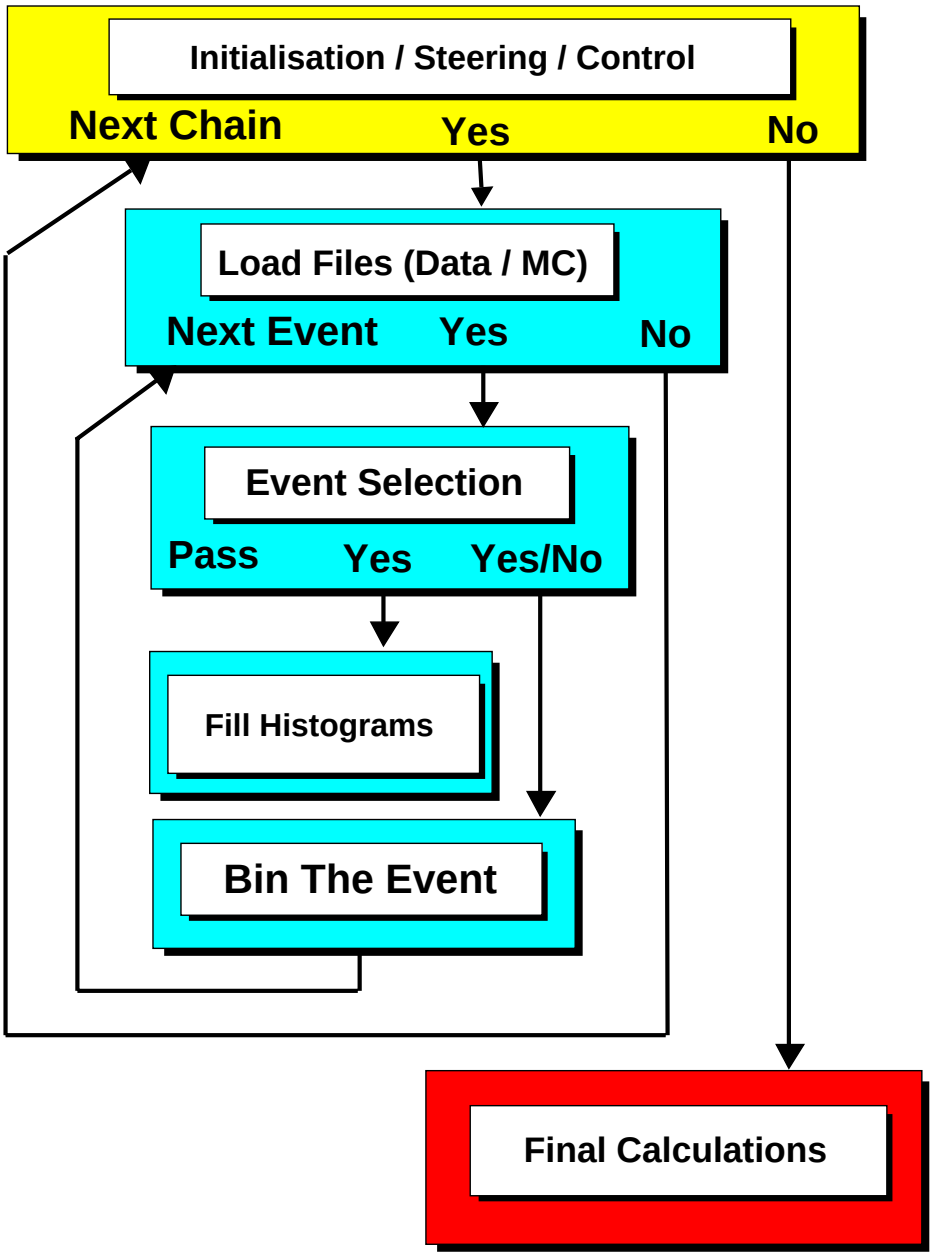

Figure 6.2: *A flow diagram of an analysis.*

source of all of the information that is needed by the other objects involved in the `Analysis`, which is itself an abstraction. The following paragraph describes in words the list given above; object candidates are highlighted.

> An `Analysis` is composed of several `AnalysisChains` each of which consist of the `Files` of data or simulated events that are to be analysed. For each `Event` in the file an `EventSelection` is made, some `Histograms` are filled and the `Event` is `Binned`. When all `AnalysisChains` have been analysed some `FinalCalculations` are done and the final `Measurement` is made.

6.3.2 The H1Calculator

The `Event` object was the first object identified in section 6.3.1. Such an object already exists in the H1OO framework under the name of `H1Calculator`. An `Event` is clearly a complex object, dealing with information ranging from tracks and clusters to identified particles such as electrons and muons and finally whether or not the `Event` is (for example) a diffractive, high Q^2 `Event`. Object composition allows the different aspects of the `Event` object to be segmented into smaller objects which are referred to as `Calculators`. Individual `Calculator` classes control the access to different aspects of the `Event` information and the `Event` object, being composed of them, controls the `Calculators` allowing the `Event` object to ensure that it is always consistent.

A simple example can be used to highlight the benefit of the `Event` object. The `Event` kinematics, calculated using several possible techniques by a kinematics `Calculator`, requires information from the scattered electron and the hadronic final state (HFS) `Calculators`. The diffractive kinematics of an `Event` require information from the kinematic `Calculator` as well as information from the diffractive final state `Calculator`. The full set of dependencies for calculating the diffractive kinematics of an `Event` can be seen in figure 6.3[1].

[1]The dependence on the `Event`'s vertex `Calculator` arises from the dependence of the scattered electron and HFS systematic uncertainties on their z position in the LAC.

The colour-coding scheme used in figure 6.3 is such that yellow `Calculator` objects have a systematic uncertainty associated with some of their information, blue and red objects do not and the red diffractive kinematics `Calculator` is the object of interest.

If a client wishes to know the effect of a systematic uncertainty on the polar angle of the scattered electron on a measurement then the client requests the `Event` object to shift the polar angle of the scattered electron by the uncertainty. This will have the result that every subsequent time the client asks the `Event` object for information about the scattered electron the polar angle of the scattered electron will be shifted by the uncertainty. Crucially, if the client also requests information about the diffractive kinematics[2] then the diffractive kinematical quantities will also be changed accordingly.

6.3.3 An Event Selection

An `Event` selection is performed by an `EventSelector` object. The basic constituent of an `EventSelector` is the `Cut` object which will return a boolean decision on the `Event`. Logical combinations of `Cut`s are also necessary and the `OrCut`, `NotCut` and `AndCut` `Cut` objects specialise in forming logical combinations of more simple `Cut` objects. The basic criteria needed to make a simple `Cut` object are the name of the variable and the range that variable is required to be in.

`Cut` objects are placed into a list of cuts (`CutList`) which provides an interface for applying all `Cut`s; this `CutList` object uses the ROOT `TObjArray` class which is an array class for `TObject`s (and `Cut` objects are also `TObject`s).

The `EventSelector` consists of three `CutList`s, one for the list of criteria for the reconstructed level properties of an `Event` for both data and simulation, one for the generator level properties of a simulated event and one for the purpose of selecting the generator level phase-space for a given simulation.

[2]The diffractive kinematics may depend on the polar angle of the scattered electron depending on the kinematic reconstruction technique used.

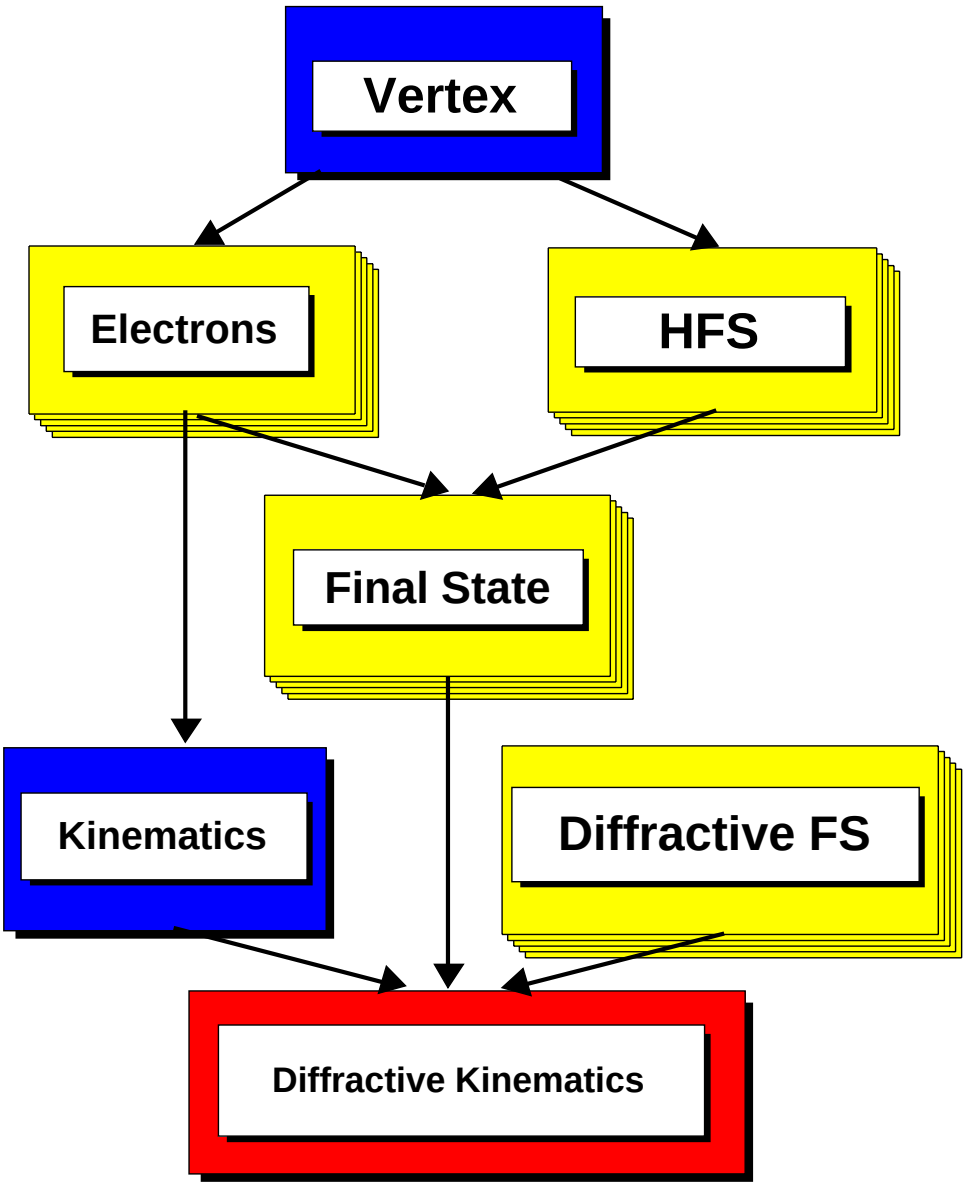

Figure 6.3: *The set of* `Calculator` *objects necessary for calculating the diffractive kinematics (red) of an* `Event`*. Yellow* `Calculator` *objects have a systematic uncertainty associated with some of their information, blue and red objects do not.*

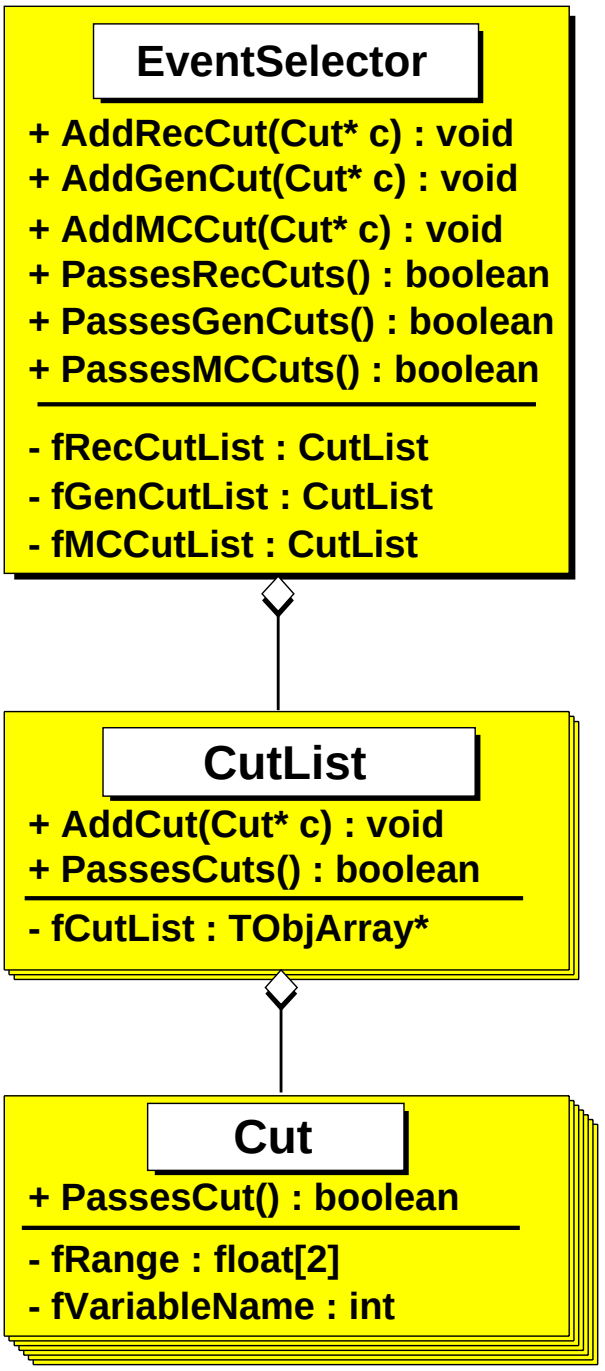

Figure 6.4: *The* `EventSelector`, `CutList` *and* `Cut` *objects.*

The `EventSelector`, `CutList` and `Cut` objects are shown in figure 6.4. In this and the other class diagrams in this section the conventions used are those of the Unified Modelling Language (UML) [86].

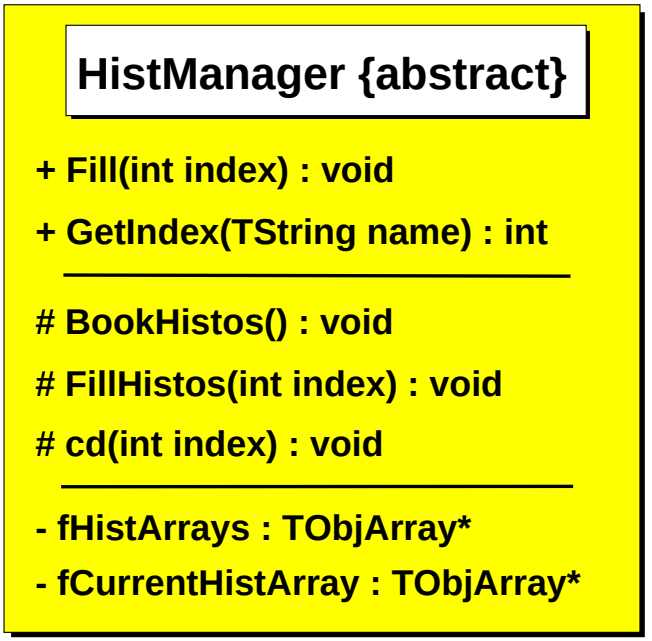

Figure 6.5: *The* `HistManager` *object.*

6.3.4 Histogramming an Event

ROOT already provides several histogram objects. However, in the course of producing an analysis many histograms are needed in order to ensure that the selected event samples are well understood. A `HistManager` object acts as an interface for several individual histogram objects. Again the ROOT `TObjArray` class is used to store the histogram objects, which are also `TObject`s. In fact a `HistManager` object can deal with the subdivision of histograms into different categories, for example reconstructed level and generator level histograms. A client books some histograms under a name of his choice and can then tell the `HistManager` to fill these histograms using that name. The `HistManager` object is shown in figure 6.5

Plotting several histograms at once for the purpose of presenting control distributions of event samples is an art unto itself, an art at which a `Plotter` object excels at.

6.3.5 Binning an Event

The process of binning an `Event` is a fairly complicated one. A `BinGrid` object defines one binning scheme, for example in this analysis two three-dimensional binning schemes are used for the binning of the cross-section measurement and thus two `BinGrid` objects are used in the `Analysis`. The results of binning an `Event` are the sets of numbers defined in section 4.3.1, i.e. $N_{REC}, N_{GEN}, N_{STAY}, N_{SMEARIN}, N_{SMEAROUT}$ and N_{LOST}. Each number has a corresponding error on that number and the two are intrinsically linked. The `Measurement` object is an abstraction of these "numbers with errors". Finally, the `Binner` object oversees the whole process of creating `Measurement`s with `BinGrid`s with the help of an object which encapsulates all of the information that it needs to perform this task, this is the `SelectionResults` object.

The `BinGrid` Object

A `BinGrid` is an N-dimensional array of bin edges. Given an N-dimensional array of numbers a `BinGrid` will return the unique bin number for that sample. For example, a `BinGrid` created with bin edges in x and Q^2 will return the bin number given a two dimensional array containing the `Event`'s value of x and Q^2. The `BinGrid` object is shown in figure 6.6.

The `Measurement` Objects

`Measurement`s are a series of related numbers. In the case of a `SimpleMeasurement` this is most easily expressed as the two values N and ΔN. In general these two values will be an array of values, the elements of which are defined by a `BinGrid` object. `CompositeMeasurement`s are collections of related `SimpleMeasurement`s, for example $N_{REC}, N_{GEN}, N_{STAY}, N_{SMEARIN}, N_{SMEAROUT}$ and N_{LOST}. The `Measurement` interface and the `SimpleMeasurement` and `CompositeMeasurement` objects are shown in figure 6.7. The `ArrayD` object also shown in this figure is an array of `double`s, an array which is also a `TObject`.

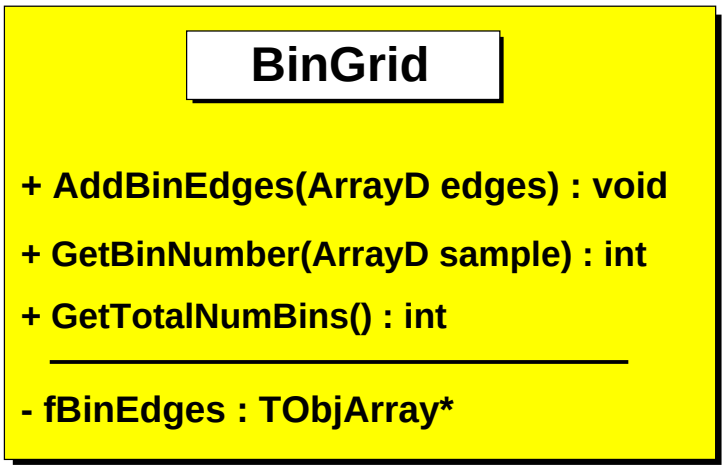

Figure 6.6: *The* `BinGrid` *object.*

The `SelectionResults` Object

The `SelectionResults` object encapsulates all of the information that is needed in order to bin an event and one `SelectionResults` object is needed per binning scheme. Figure 6.8 shows this simple object together with the `CalcReader` object. The `CalcReader` object is given an array of variable names and it retrieves the corresponding variables from the `Event` object when asked to.

The `Binner` Objects

A `Binner` object oversees the whole binning process, using a `BinGrid` to bin one or more `Measurements`. As such it houses the binning algorithm and the algorithms for the calculations of *Acceptance*, *Purity* and *Stability*. `DataBinner` and `ModelBinner` objects each specialise in binning data and simulations respectively, they are shown in figure 6.9 together with the `Binner` interface.

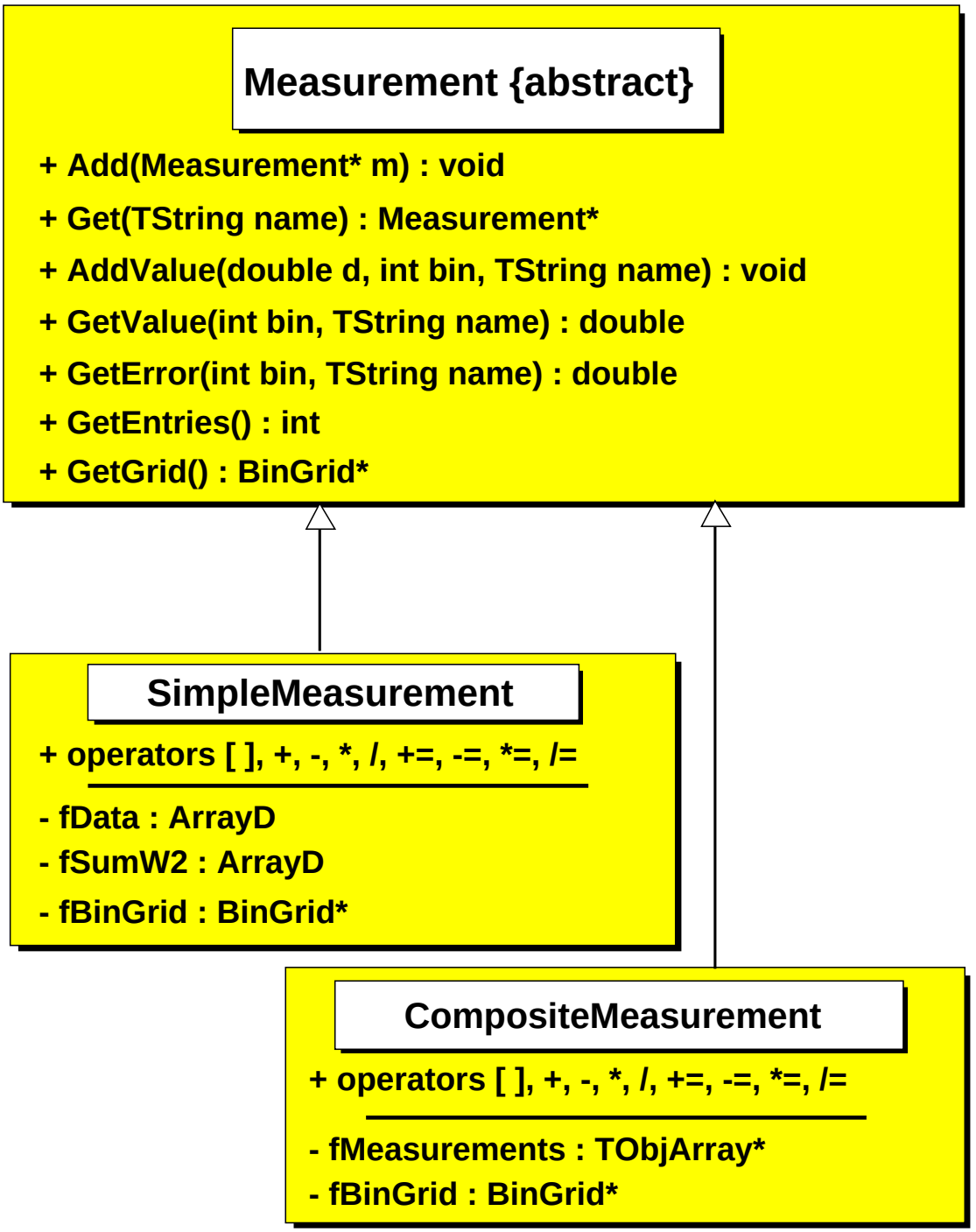

Figure 6.7: *The* `Measurement` *interface and the* `SimpleMeasurement` *and* `CompositeMeasurement` *objects.*

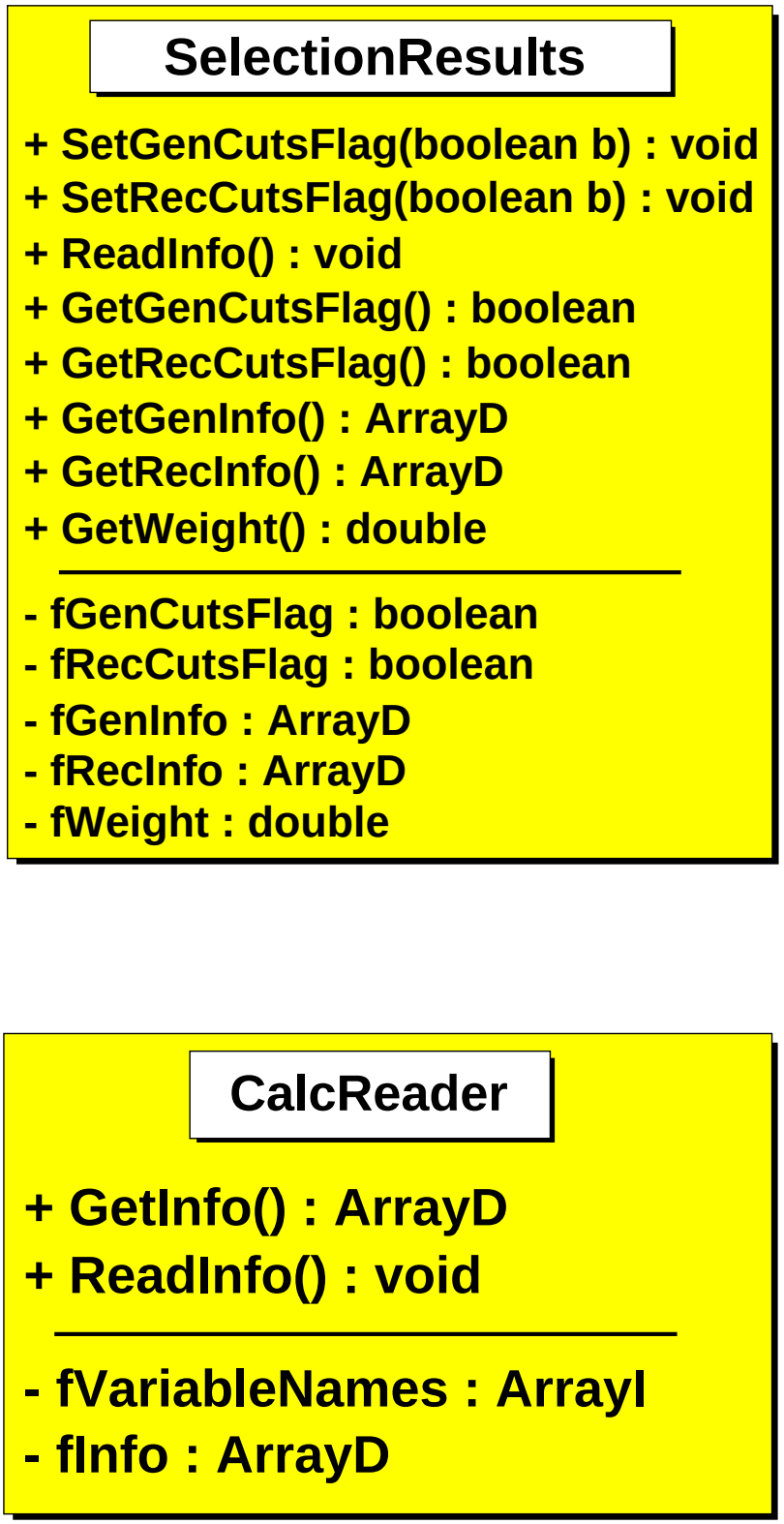

Figure 6.8: *The* `SelectionResults` *and* `CalcReader` *objects.*

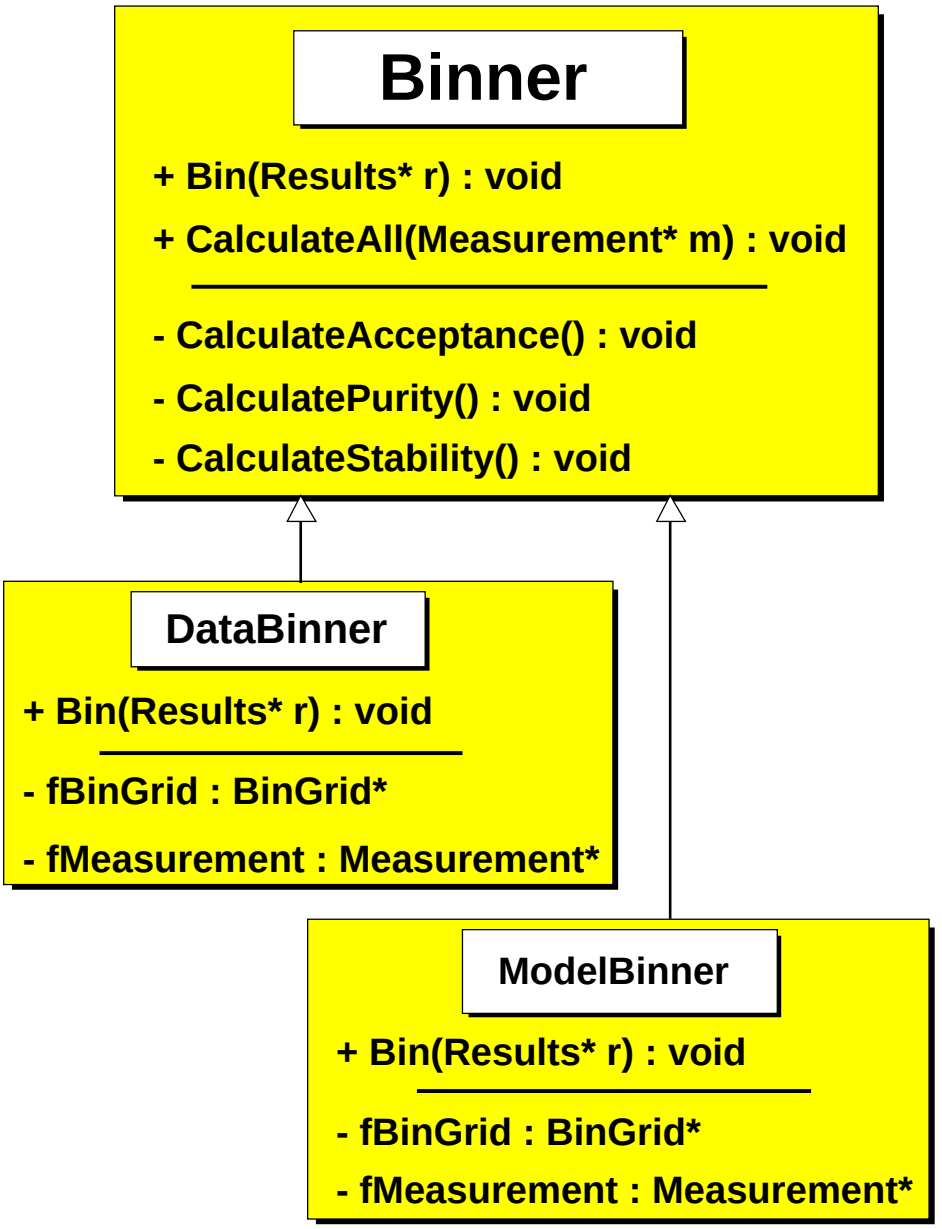

Figure 6.9: *The* `Binner` *interface and the* `DataBinner` *and* `ModelBinner` *objects.*

6.3.6 An Analysis Chain

An `AnalysisChain` stores the `HistManager`s and `Measurement`s for one chain[3] of analysis. The actual behaviour of an `AnalysisChain` is defined by its `EventLoop` member function, which defines what the `AnalysisChain` does on an event by event basis. Default implementations for data, background and model `AnalysisChain`s are also part of the analysis framework.

File Management

The `AnalysisChain` uses a `FileManager` object to manage the finding and loading of the files that it will analyse. The `FileManager` object in turn deals with the `H1Tree` of the H1OO framework, which is the interface to both the μODS and HAT layers. Both the `AnalysisChain` and `FileManager` objects are shown in figure 6.10.

6.3.7 The `Analysis` Object

An `Analysis` object is composed of one or more `BinGrid`s, one or more `EventSelector`s, one or more `SelectionResults`s and one or more `AnalysisChain`s. Its behaviour is dictated by the `DoAnalysis` member function, a default implementation of which exists in the framework[4]. At the end of the analysis job the `Analysis` object is written as one coherent object to a ROOT file. Crucially, when the analysis object is subsequently read back from its file it is still an object; the analysis itself is consistent. The `Analysis` object is shown in figure 6.11.

[3]The name is taken from the PAW definition where a chain represents a set of files.

[4]The default implementation simply loops over all exisiting `AnalysisChain`s asking them to perform their `DoAnalysis` tasks.

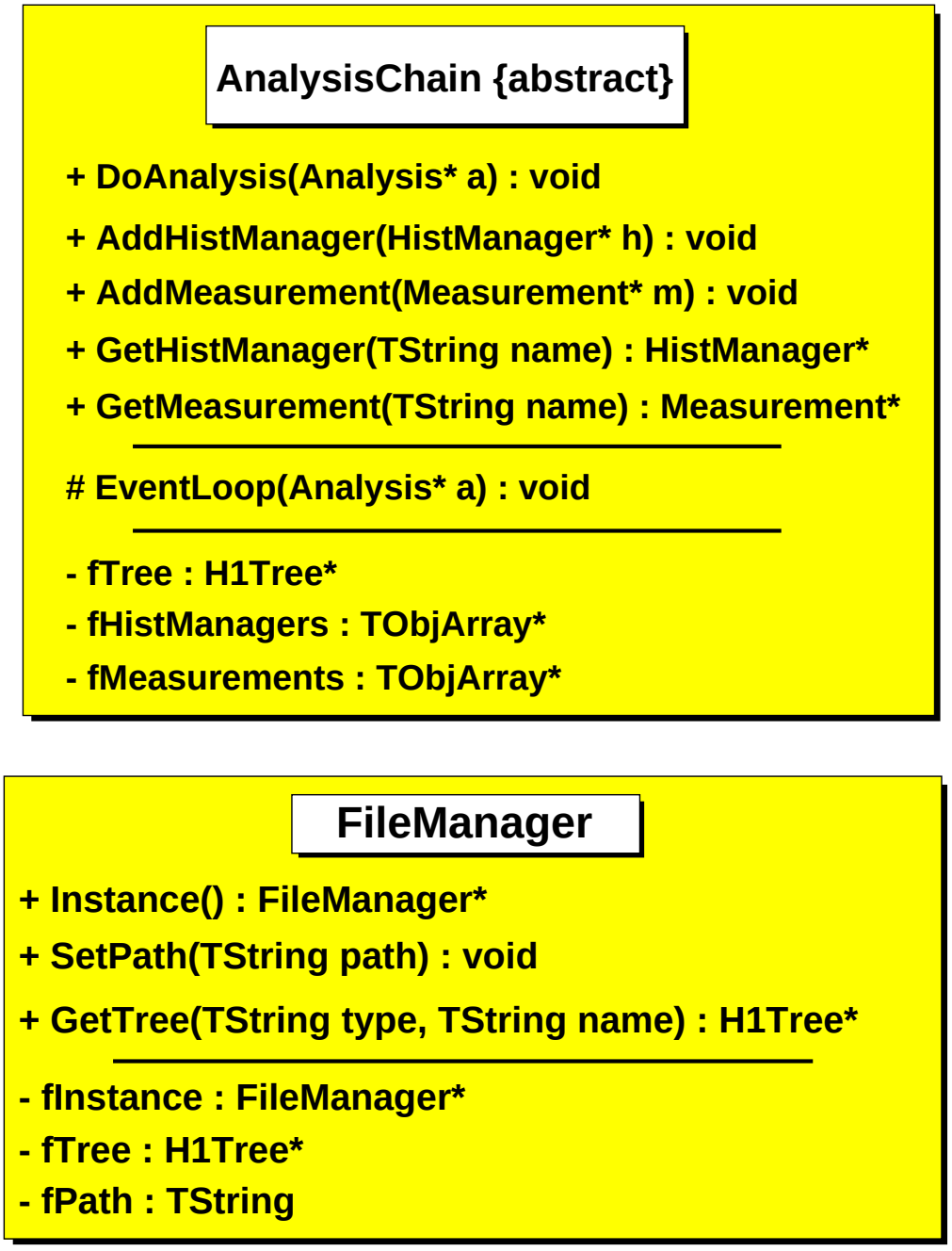

Figure 6.10: *The* `AnalysisChain` *and* `FileManager` *objects.*

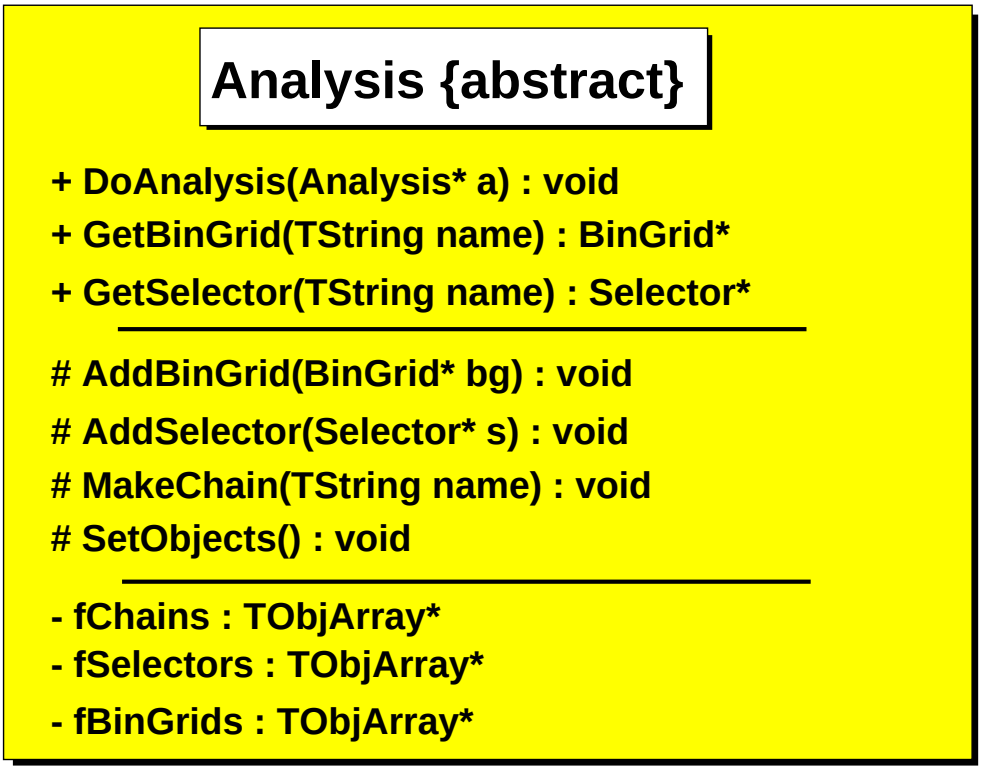

Figure 6.11: *The* `Analysis` *object.*

6.3.8 The Complete Design

The complete design for the generic analysis framework is shown in figure 6.12. Structurally the framework is centred around the `Analysis` object which houses the `BinGrid`s, `EventSelector`s, `SelectionResults`s and `AnalysisChain`s and these objects are initialised according to some steering parameters at the start of the analysis job. In the default implementation of the `DoAnalysis` function of the `Analysis` object the `AnalysisChain` objects are simply looped over and asked to do their `DoAnalysis` task. This will consist of loading in a new set of files via the `FileManager` object which will then be analysed in the `EventLoop`.

In a typical implementation of the `EventLoop` function the `EventSelector` will be required to perform its `Event` selections at the reconstructed and generator levels for each event. Depending on the results of these selections the `HistManager` will be required to fill some histograms. At the end of the `EventLoop` the `Binner` object will `Bin` the `SelectionResults` object, which has gathered all of the necessary information, and updates one or more `Measurement`s according to the definition provided by the `BinGrid`. When there are no more events left to analyse the `Binner` performs the calculations of *Acceptance*, *Purity* and *Stability* and creates `Measurement` objects to store these numbers. All of the `Measurement`s created by the `Binner` are then given to the `AnalysisChain` to store. The `HistManager` is added to the `AnalysisChain` during initialisation.

When all of the `AnalysisChain` objects have finished doing their work the `Analysis` object simply writes itself to a ROOT file. This default behaviour can be changed by overriding the `DoAnalysis` function of the `Analysis` object. All `AnalysisChain`s, `BinGrid`s, `EventSelector`s and `SelectionResults` objects are therefore written together as part of one coherent `Analysis` object, which also stores any steering parameters used. If a physicist want to know the selection used to produce the cross-section measurement made with a particular `Analysis` object then he/she just needs to ask the `Analysis` object.

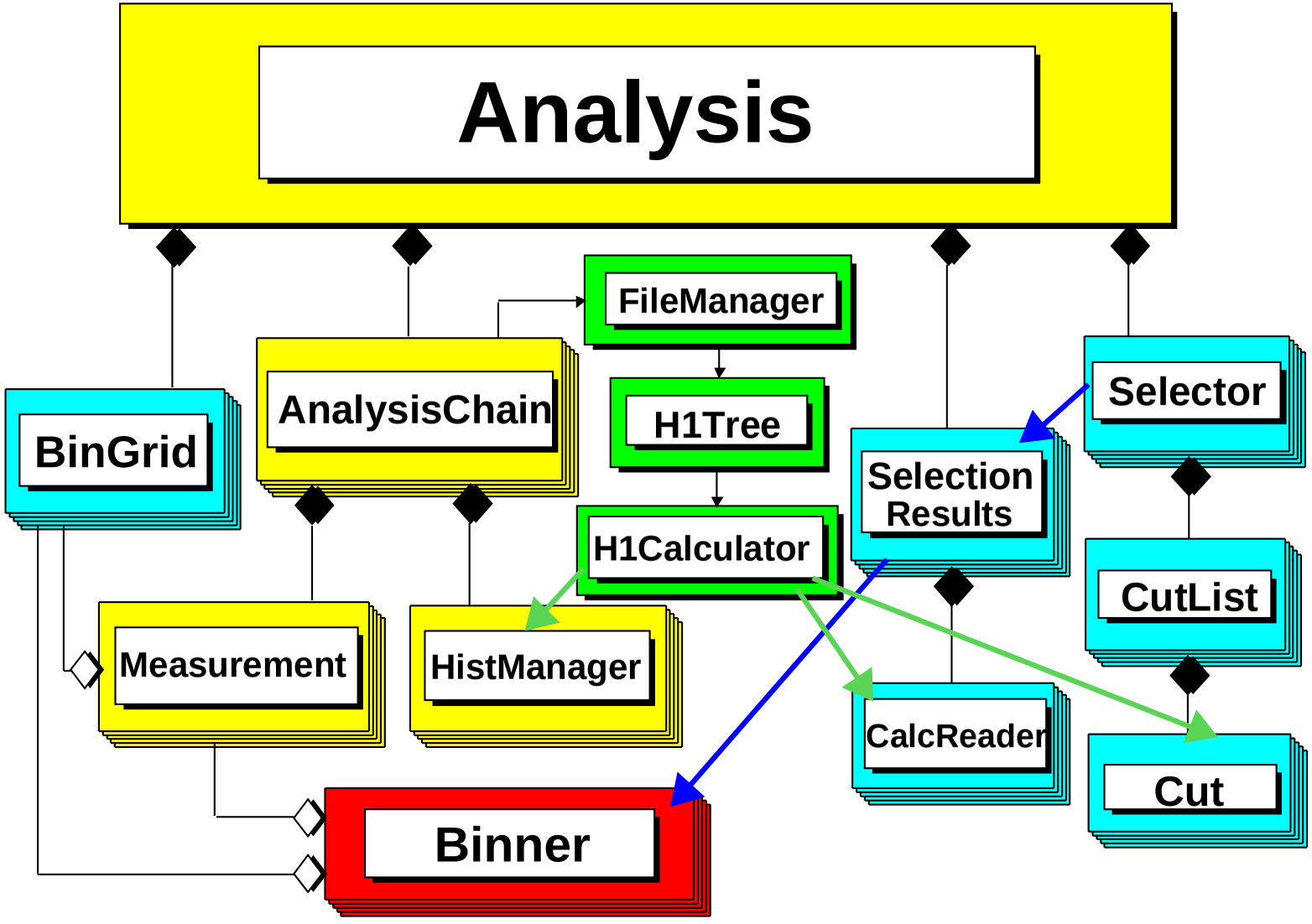

Figure 6.12: *The generic analysis framework design.*

6.3.9 Improvements and Future Work

The physics analysis uses of the generic analysis framework presented here currently range from "Searches for Leptoquarks" and "Studies of isolated electrons and muons in events with missing transverse momentum" to "Measurements of the inclusive NC and CC cross-sections" and of course the measurement of the diffractive reduced cross-section at high Q^2 presented here. The framework continues to develop as it acquires more users who demand more flexibility and functionality of it. The following is a discussion of general improvements that could be made to enhance the framework.

Cross-Section Extractions and Systematic Uncertainties

The cross-section extraction procedure involves many sets of numbers and, despite the `CompositeMeasurement` object, still requires many objects (greater than the 7 ± 2 goal). At least one potential object would make this procedure simpler, an object which deals with calculating the error arising from a systematic uncertainty on the measurement. In general this error is calculated from the change in the *Acceptance* correction found for each particular uncertainty and a `SystematicMeasurement` could generalise and thereby simplify this procedure.

Steering

The `Analysis`, `AnalysisChain` and `SelectionResults` are all entirely steerable and the `EventSelector` object can be partially steered to enable or disable `Cuts` through the `AnalysisChain` steering. The H1OO Steering mechanism allows any object to be steered and so this list could be extended to include all of the objects in the framework. The decision on whether or not to steer an object must be a compromise between compile-time errors, which are preferred, and run-time errors.

A Graphical User Interface

The ROOT framework already supports graphical objects and a graphical user interface to the analysis framework would make it yet more user-friendly. A full "Point and Click" physics analysis would have many obvious benefits, for example an `Analysis` object stored in a ROOT file could be sent to a colleague who may then be several mouse-clicks away from not only seeing the results but any other related information.

Appendix A

Tables of Cross-Section Results

Q^2 (GeV^2)	β	x_{IP}	$x_{IP}\sigma_r^{D(3)}$	δ_{stat}	δ_{sys}
200.0	0.106667	0.03	0.044639	0.053	0.107
200.0	0.166667	0.03	0.040093	0.046	0.114
200.0	0.266667	0.03	0.031921	0.051	0.107
200.0	0.320000	0.01	0.032590	0.050	0.093
200.0	0.433333	0.03	0.030096	0.052	0.111
200.0	0.500000	0.01	0.027015	0.048	0.106
200.0	0.666667	0.03	0.021232	0.067	0.127
200.0	0.800000	0.01	0.016398	0.069	0.119
400.0	0.266667	0.03	0.034476	0.073	0.103
400.0	0.433333	0.03	0.029282	0.065	0.111
400.0	0.666667	0.03	0.021633	0.072	0.115
400.0	0.800000	0.01	0.016850	0.110	0.133
800.0	0.433333	0.03	0.037834	0.116	0.123
800.0	0.666667	0.03	0.016580	0.132	0.126
1600.0	0.666667	0.03	0.015760	0.254	0.190

Table A.1: *The diffractive reduced cross-section $\sigma_r^{D(3)}(Q^2, \beta, x_{IP})$ multiplied by x_{IP} as measured in bins of fixed Q^2, x and x_{IP}. The quantities δ_{stat} and δ_{sys} represent the fractional statistical and systematic errors, respectively.*

Q^2 (GeV^2)	β	x_{IP}	$x_{IP}\sigma_r^{D(3)}$	δ_{stat}	δ_{sys}
200.0	0.10	0.032000	0.049455	0.070	0.132
200.0	0.20	0.016000	0.033355	0.058	0.108
200.0	0.20	0.025000	0.034738	0.053	0.123
200.0	0.20	0.040000	0.037552	0.075	0.137
200.0	0.40	0.008000	0.030565	0.076	0.110
200.0	0.40	0.012500	0.027801	0.062	0.115
200.0	0.40	0.020000	0.026605	0.067	0.106
200.0	0.40	0.032500	0.030994	0.078	0.134
200.0	0.65	0.004923	0.030915	0.089	0.121
200.0	0.65	0.007692	0.025607	0.073	0.120
200.0	0.65	0.012308	0.023395	0.073	0.113
200.0	0.65	0.020000	0.021863	0.077	0.122
200.0	0.65	0.030769	0.024284	0.078	0.132
200.0	0.65	0.049231	0.020425	0.109	0.173
200.0	0.90	0.003556	0.022024	0.203	0.211
200.0	0.90	0.005556	0.012713	0.182	0.231
200.0	0.90	0.008889	0.014579	0.174	0.211
200.0	0.90	0.014444	0.006831	0.233	0.212
200.0	0.90	0.022222	0.006459	0.252	0.236
200.0	0.90	0.035556	0.004461	0.374	0.489

Table A.2: *The diffractive reduced cross-section* $\sigma_r^{D(3)}(Q^2, \beta, x_{IP})$ *multiplied by* x_{IP} *as measured in bins of fixed* Q^2, x *and* β *for* $Q^2 = 200$ GeV^2. *The quantities* δ_{stat} *and* δ_{sys} *represent the fractional statistical and systematic errors, respectively.*

Q^2 (GeV^2)	β	x_{IP}	$x_{IP}\sigma_r^{D(3)}$	δ_{stat}	δ_{sys}
400.0	0.20	0.040000	0.042185	0.107	0.150
400.0	0.40	0.020000	0.029400	0.097	0.115
400.0	0.40	0.032500	0.028070	0.104	0.139
400.0	0.40	0.050000	0.029144	0.150	0.225
400.0	0.65	0.012308	0.023841	0.115	0.135
400.0	0.65	0.020000	0.020908	0.089	0.118
400.0	0.65	0.030769	0.025187	0.083	0.119
400.0	0.65	0.049231	0.019766	0.112	0.168
400.0	0.90	0.008889	0.010775	0.293	0.197
400.0	0.90	0.014444	0.010946	0.241	0.221
400.0	0.90	0.022222	0.005240	0.300	0.283
400.0	0.90	0.035556	0.005505	0.297	0.334
800.0	0.40	0.032500	0.031758	0.185	0.171
800.0	0.65	0.020000	0.029304	0.169	0.157
800.0	0.65	0.030769	0.017839	0.161	0.135
800.0	0.65	0.049231	0.023023	0.164	0.161
800.0	0.90	0.014444	0.010672	0.527	0.251
800.0	0.90	0.022222	0.004165	0.513	0.312
800.0	0.90	0.035556	0.008997	0.335	0.232
1600.0	0.65	0.030769	0.013968	0.354	0.289
1600.0	0.65	0.049231	0.017106	0.282	0.148
1600.0	0.90	0.022222	0.005472	0.768	0.289
1600.0	0.90	0.035556	0.001585	1.155	0.252

Table A.3: *The diffractive reduced cross-section $\sigma_r^{D(3)}(Q^2, \beta, x_{IP})$ multiplied by x_{IP} as measured in bins of fixed Q^2, x and β for $Q^2 = 400, 800$ and 1600 GeV^2. The quantities δ_{stat} and δ_{sys} represent the fractional statistical and systematic errors, respectively.*

References

[1] I. Ia. Pomeranchuk. The Conservation of Isotopic Spin and the Scattering of Antinucleons by Nucleons. *Soviet Physics JETP*, 3:306–307, 1956.

[2] I. Ia. Pomeranchuk and L.B. Okun. The Conservation of Isotopic Spin and the Cross Section of the Interaction of High-Energy π-Mesons and Nucleons with Nucleons. *Soviet Physics JETP*, 3:307–308, 1956.

[3] L. L. Foldy and R. F. Peierls. Isotopic Spin of Exchanged Sytems. *Physical Review*, 130:1585–1589, 1963.

[4] T. Regge. Introduction to Complex Orbital Momenta. *Nuovo Cim.*, 14:951, 1959.

[5] T. Regge. Bound States, Shadow States and Mandelstam Representation. *Nuovo Cim.*, 18:947–956, 1960.

[6] A. Donnachie and P. V. Landshoff. Total Cross-Sections. *Phys. Lett.*, B296:227–232, 1992.

[7] S. Abatzis et al. Observation of a Narrow Scalar Meson at 1450-MeV in the Reaction $pp \to p_f(\pi^+\pi^-\pi^+\pi^-)p_s$ at 450-GeV/c Using the CERN Omega Spectrometer. *Phys. Lett.*, B324:509–514, 1994.

[8] John C. Collins. Proof of Factorization for Diffractive Hard Scattering. *Phys. Rev.*, D57:3051–3056, 1998.

[9] G. Ingelman and P. E. Schlein. Jet Structure in High Mass Diffractive Scattering. *Phys. Lett.*, B152:256, 1985.

[10] R. Keith Ellis, Howard Georgi, Marie Machacek, H. David Politzer, and Graham G. Ross. Factorization and the Parton Model in QCD. *Phys. Lett.*, B78:281, 1978.

[11] I. J. R. Aitchison and A. J. G. Hey. Gauge Theories in Particle Physics: A Practical Introduction. Bristol, UK: Hilger (1989) 571p.

[12] F. Halzen and Alan D. Martin. Quarks and Leptons: An Introductory Course in Modern Particle Physics. New York, Usa: Wiley (1984) 396p.

[13] C. Adloff et al. Measurement and QCD Analysis of Neutral and Charged Current Cross Sections at HERA. 2003. Submitted to Eur. Phys. J, 04/03.

[14] C. Adloff et al. Measurement of Neutral and Charged Current Cross Sections in Electron Proton Collisions at High Q^2. *Eur. Phys. J.*, C19:269–288, 2001.

[15] Martin Breidenbach et al. Observed Behavior of Highly Inelastic Electron - Proton Scattering. *Phys. Rev. Lett.*, 23:935–939, 1969.

[16] Jerome I. Friedman and Henry W. Kendall. Deep Inelastic Electron Scattering. *Ann. Rev. Nucl. Part. Sci.*, 22:203–254, 1972.

[17] Murray Gell-Mann. A Schematic Model of Baryons and Mesons. *Phys. Lett.*, 8:214–215, 1964.

[18] Yuri L. Dokshitzer. Calculation of the Structure Functions for Deep Inelastic Scattering and e+ e- Annihilation by Perturbation Theory in Quantum Chromodynamics. (in Russian). *Sov. Phys. JETP*, 46:641–653, 1977.

[19] V. N. Gribov and L. N. Lipatov. e+ e- Pair Annihilation and Deep Inelastic e p Scattering in Perturbation Theory. *Yad. Fiz.*, 15:1218–1237, 1972.

[20] V. N. Gribov and L. N. Lipatov. Deep Inelastic e p Scattering in Perturbation Theory. *Yad. Fiz.*, 15:781–807, 1972.

[21] Guido Altarelli and G. Parisi. Asymptotic Freedom in Parton Language. *Nucl. Phys.*, B126:298, 1977.

[22] E. A. Kuraev, L. N. Lipatov, and Victor S. Fadin. Multi - Reggeon Processes in the Yang-Mills Theory. *Sov. Phys. JETP*, 44:443–450, 1976.

[23] I. I. Balitsky and L. N. Lipatov. The Pomeranchuk Singularity in Quantum Chromodynamics. *Sov. J. Nucl. Phys.*, 28:822–829, 1978.

[24] Marcello Ciafaloni. Coherence Effects in Initial Jets at Small Q^2 / s. *Nucl. Phys.*, B296:49, 1988.

[25] S. Catani, F. Fiorani, and G. Marchesini. QCD Coherence in Initial State Radiation. *Phys. Lett.*, B234:339, 1990.

[26] S. Catani, F. Fiorani, and G. Marchesini. Small x Behavior of Initial State Radiation in Perturbative QCD. *Nucl. Phys.*, B336:18, 1990.

[27] C. Adloff et al. Multi-Jet Event Rates in Deep Inelastic Scattering and Determination of the Strong Coupling Constant. *Eur. Phys. J.*, C6:575–585, 1999.

[28] Frank-Peter Schilling. NLO QCD Fit to H1 Diffractive DIS Data. *Acta Phys. Polon.*, B33:3419–3424, 2002.

[29] F. P. Schilling. Inclusive Diffraction at HERA. 2002. To appear in the proceedings of the 31st Intl. Conference on High Energy Physics, Amsterdam (ICHEP 2002).

[30] J. R. Forshaw and D. A. Ross. Quantum Chromodynamics and the Pomeron. Cambridge, UK: Univ. Pr. (1997) 248 p. (Cambridge lecture notes in physics. 9).

[31] G. F. Chew and S. C. Frautschi. Principle of Equivalence for all Strongly Interacting Particles Within the S Matrix Framework. *Phys. Rev. Lett.*, 7:394–397, 1961.

[32] G. F. Chew and S. C. Frautschi. Regge Trajectories and the Principle of Maximum Strength for Strong Interactions. *Phys. Rev. Lett.*, 8:41–44, 1962.

[33] P. Laycock. New Results on Inclusive Diffraction. *Acta Phys. Polon.*, B33:3413–3417, 2002.

[34] A. Edin, G. Ingelman, and J. Rathsman. Soft Color Interactions as the Origin of Rapidity Gaps in DIS. *Phys. Lett.*, B366:371–378, 1996.

[35] A. Edin, G. Ingelman, and J. Rathsman. Unified Description of Rapidity Gaps and Energy Flows in DIS Final States. *Z. Phys.*, C75:57–70, 1997.

[36] Johan Rathsman. A Generalised Area Law for Hadronic String Reinteractions. *Phys. Lett.*, B452:364–371, 1999.

[37] W. Buchmuller, T. Gehrmann, and A. Hebecker. Inclusive and Diffractive Structure Functions at Small x. *Nucl. Phys.*, B537:477–500, 1999.

[38] Torbjorn Sjostrand. The Lund Monte Carlo for Jet Fragmentation and e+ e- Physics: JETSET Version 6.2. *Comput. Phys. Commun.*, 39:347–407, 1986.

[39] Bo Andersson, G. Gustafson, G. Ingelman, and T. Sjostrand. Parton Fragmentation and String Dynamics. *Phys. Rept.*, 97:31, 1983.

[40] G. A. Schuler and H. Spiesberger. DJANGO: The Interface for the Event Generators HERACLES and LEPTO. In *Hamburg 1991, Proceedings, Physics at HERA, vol. 3* 1419-1432. (see High Energy Physics Index 30 (1992) No. 12988).

[41] A. Kwiatkowski, H. Spiesberger, and H. J. Mohring. HERACLES: An Event Generator for e p Interactions at HERA Energies Including Radiative Processes: Version 1.0. *Comp. Phys. Commun.*, 69:155–172, 1992.

[42] Leif Lonnblad. ARIADNE Version 4: A Program for Simulation of QCD Cascades Implementing the Color Dipole Model. *Comput. Phys. Commun.*, 71:15–31, 1992.

[43] Gosta Gustafson and Ulf Pettersson. Dipole Formulation of QCD Cascades. *Nucl. Phys.*, B306:746, 1988.

[44] Bo Andersson, Gosta Gustafson, Leif Lonnblad, and Ulf Pettersson. Coherence Effects in Deep Inelastic Scattering. *Z. Phys.*, C43:625, 1989.

[45] Bo Andersson, Gosta Gustafson, and Leif Lonnblad. Gluon Splitting in the Color Dipole Cascades. *Nucl. Phys.*, B339:393–406, 1990.

[46] C. Adloff et al. Measurement of Neutral and Charged Current Cross-Sections in Positron Proton Collisions at Large Momentum Transfer. *Eur. Phys. J.*, C13:609–639, 2000.

[47] Hannes Jung. Hard Diffractive Scattering in High-Energy e p Collisions and the Monte Carlo Generation RAPGAP. *Comp. Phys. Commun.*, 86:147–161, 1995.

[48] C. Adloff et al. Inclusive Measurement of Diffractive Deep-Inelastic *ep* Scattering. *Z. Phys.*, C76:613–629, 1997.

[49] H. Plothow-Besch. PDFLIB: A Library of all Available Parton Density Functions of the Nucleon, the Pion and the Photon and the Corresponding alpha-s Calculations. *Comput. Phys. Commun.*, 75:396–416, 1993.

[50] H. Plothow-Besch. The Parton Distribution Function Library. *Int. J. Mod. Phys.*, A10:2901–2920, 1995.

[51] B. List and A. Mastroberardino. DIFFVM: A Monte Carlo Generator for Diffractive Processes in e p Scattering. Prepared for Workshop on Monte Carlo Generators for HERA Physics (Plenary Starting Meeting), Hamburg, Germany, 27-30 Apr 1998.

[52] A. Courau and P. Kessler. QED Compton Scattering in High-Energy Electron - Proton Collisions. *Phys. Rev.*, D46:117–124, 1992.

[53] S. P. Baranov, O. Duenger, H. Shooshtari, and J. A. M. Vermaseren. LPAIR: A Generator for Lepton Pair Production. In *Hamburg 1991, Proceedings, Physics at HERA, vol. 3* 1478-1482. (see High Energy Physics Index 30 (1992) No. 12988).

[54] I. Abt et al. The Tracking, Calorimeter and Muon Detectors of the H1 Experiment at HERA. *Nucl. Instrum. Meth.*, A386:348–396, 1997.

[55] I. Abt et al. The H1 Detector at HERA. *Nucl. Instrum. Meth.*, A386:310–347, 1997.

[56] K. Muller et al. Construction and Performance of a Thin Cylindrical Multiwire Proportional Chamber with Cathode Pad Readout for the H1 Experiment. *Nucl. Instrum. Meth.*, A312:457–466, 1992.

[57] S. Egli et al. The Central Inner z Drift Chamber of the H1 Experiment. *Nucl. Instrum. Meth.*, A283:487–491, 1989.

[58] Jan Haack. Calibration of the Outer z Drift Chamber of the HERA H1 Experiment. DESY-ZEUTHEN-94-03.

[59] J. Burger et al. The Central Jet Chamber of the H1 Experiment. *Nucl. Instrum. Meth.*, A279:217–222, 1989.

[60] S. Burke et al. Track Finding and Fitting in the H1 Forward Track Detector. *Nucl. Instrum. Meth.*, A373:227–260, 1996.

[61] B. Andrieu et al. The H1 Liquid Argon Calorimeter System. *Nucl. Instrum. Meth.*, A336:460–498, 1993.

[62] B. Andrieu et al. Electron / Pion Separation with the H1 LAr Calorimeters. *Nucl. Instrum. Meth.*, A344:492–506, 1994.

[63] Mattias Ruffer. Implementing the Silicon Instrumented PLUG Calorimeter in the H1 Detector. DESY-FH1K-93-01.

[64] J. Heatherington et al. Studies on ToF FTDC Data. H1 Internal Note H1-IN-307(08/1993).

[65] H. Bethe and W. Heitler. On the Stopping of Fast Particles and on the Creation of Positive Electrons. *Proc. Roy. Soc. Lond.*, A146:83–112, 1934.

[66] P. Biddulph et al. The H1 Forward Muon Spectrometer. *Nucl. Instrum. Meth.*, A340:304–308, 1994.

[67] P. Bruel. Recherche d'Interactions au-delà du Modèle Standard à HERA. Thesis 05/98.

[68] Beate Heinemann. Measurement of Charged Current and Neutral Current Cross Sections in Positron Proton Collisions at $\sqrt{s} \approx 300\ GeV^2$. DESY-THESIS-1999-046.

[69] C. Adloff et al. Diffraction Dissociation in Photoproduction at HERA. *Z. Phys.*, C74:221–236, 1997.

[70] E. Chabert et al. Marseille. QBGFMAR: An Updated Phan Package for Cosmic and Halo Muon Topological Rejection in High P_T Physics Analysis. H1 Internal Note h1-1198-556.

[71] Eram Rizvi. Private Communication.

[72] Andy Mehta. Private Communication.

[73] Frank-Peter Schilling. Private Communication.

[74] Paul Newman and Carrie Johnson. Private Communication.

[75] H1 Collaboration. Measurement and Interpretation of the Diffractive Structure Function $F_2^{D(3)}$ at HERA. Contributed paper no. 571 submitted to ICHEP 1998 (Vancouver).

[76] C. Adloff et al. Diffraction Dissociation in Photoproduction at HERA. *Z. Phys.*, C74:221–236, 1997.

[77] C. Adloff et al. Proton Dissociative Rho and Elastic Phi Electroproduction at HERA. *Z. Phys.*, C75:607–618, 1997.

[78] T. Ahmed et al. Photoproduction of J/Psi Mesons at HERA. *Phys. Lett.*, B338:507–518, 1994.

[79] C. Adloff et al. A Measurement of the Proton Structure Function F2(x,Q^2) at Low x and Low Q^2 at HERA. *Nucl. Phys.*, B497:3–30, 1997.

[80] C. Adloff et al. Measurement and NLO DGLAP QCD Interpretation of Diffractive Deep-Inelastic Scattering at HERA. 2002. Submitted to 31st Intl. Conference on High Energy Physics, Amsterdam (ICHEP 2002), Abstract 980.

[81] G. A. Miller. The Magical Number Seven, Plus or Minus Two: Some Limits on Our Capacity for Processing Information. *The Psychological Review*, 63:81–97, 1956.

[82] R. Brun and F. Rademakers. ROOT: An Object Oriented Data Analysis Framework. *Nucl. Instrum. Meth.*, A389:81–86, 1997.

[83] A. B. Meyer. A New Object-Oriented Physics Analysis Framework for the H1 Experiment. Published in Budapest 2001, High Energy Physics hep2001/276.

[84] Rene Brun, Olivier Couet, Carlo E. Vandoni, and Pietro Zanarini. PAW: A General Purpose Portable Software Tool for Data Analysis and Presentation. *Comput. Phys. Commun.*, 57:432–437, 1989.

[85] The OO Project Team. A Steering Mechanism for the H1 OO Analysis Environment.

[86] Object Management Group. OMG Unified Modeling Language Specification. March 2003. Version 1.5.